Interstitial diffusion in Li-ion battery electrodes and structural phase transitions in crystalline solids from first principles

by

Jishnu Bhattacharya

A dissertation submitted in partial fulfillment
of the requirements for the degree of
Doctor of Philosophy
(Mechanical Engineering)
in the University of Michigan
2010

Doctoral Committee:

Assistant Professor Anton Van der Ven, Co-Chair
Assistant Professor Vikram Gavini, Co-Chair
Associate Professor Krishnakumar Garikipati
Associate Professor Katsuyo Thornton

To my parents

Acknowledgements

First of all, I would take the opportunity of expressing my deepest feeling of obligation to my thesis advisor Anton Van der Ven. Whenever I approached him with some concern, his calm, smiley patience and the precious ideas showed me the way. His continuous guidance, encouragement and support were crucial in making this thesis possible.

I sincerely appreciate the ideas and constructive criticisms I received from my doctoral thesis committee members, Vikram Gavini, Krishna Garikipati and Katsuyo Thornton. Without their suggestions my research work would have been incomplete.

During the coursework at University of Michigan, I learnt a lot from Prof. Dowling, Prof. Borgnakke, Prof. Chen, Prof. Smadar, Prof. Van der Ven, Prof. Pipe, Prof. Gavini and got very helpful company of friends: Gaurav, Jaskirat, Sai, Jingli, Vinod, Christian.

I express my sincere gratitude to Prof. Pradip Dutta (IISc, India), my master degree thesis advisor and Prof. Suman Chakraborty (IIT Kharagpur, India), for their constant advice and the initial push I needed for venturing my PhD.

I want to thank my friends, Bibhas, Kaushik, Sriparna, Saikat, Umesh, Bodhi, Soma, Harsh, Sam, Ayan and Alok for making my stay in Ann Arbor as enjoyable as possible. I appreciate their cooperation in every other aspects of life which kept me focused on my research work.

The department of Mechanical Engineering, especially Cynthia Quann-White and Material Science and Engineering, especially Renee Hilgendorf and Lisa Moran have helped me a lot during any official need in my graduate years. I acknowledge Dean's scholarship from Mechanical Engineering for my first-year funding.

I am thankful to my fellow lab mates: Qingchuan Xu, Jessica Bickel, John C. Thomas, Andrew Dalton and Ling Chen for a nice and productive research environment. Qingchuan helped me although my initial period of struggle and I fondly remember the long discussions I have with John during our joint coding endeavors.

I would like to thank my parents-in-law for sincere enthusiasm they showed in my research and for making me at-home and calm in any situation of confusion.

My family has always stood beside me throughout my life especially during my stay in the graduate school. The faith of my parents on me and their encouragement in every tough situation made me what I am today. The members of my extended family, especially *barojhethu*, *barda*, *bardi* and *chhoto-mama-mami* took pride in my achievements and shared the moments of joy and sorrow. My elder brother has always been my friend, philosopher and guide without whose guidance it would have impossible for me to finish this thesis work. I thank my sister-in-law for being a well-wisher of mine. My little niece *Rani* brought fresh and pure air every now and then and helped me keep smiling even in hard days.

It is needless to express my sincere appreciation for my wife, Ananya's role in the most crucial stage of my stay in the graduate school. Her love, sacrifice and bold company made me surpass the roughest terrains of my thesis work.

Table of Contents

List of Figures

Abstract

We perform first-principles investigations of thermally activated phase transitions and diffusion in solids. The atomic scale energy landscapes are evaluated with first-principles total energy calculations for different structural and configurational microstates. Effective Hamiltonians constructed from the total energies are subjected to Monte Carlo simulations to study thermodynamic and kinetic properties of the solids at finite temperatures.

Cubic to tetragonal martensitic phase transitions are investigated beyond the harmonic approximation. As an example, stoichiometric TiH_2 is studied where a cubic phase becomes stable at high temperature while ab-initio energy calculations predict the cubic phase to be mechanically unstable with respect to tetragonal distortions at zero Kelvin. An anharmonic Hamiltonian is used to explain the stability of the cubic phase at higher temperature. The importance of anharmonic terms is emphasized and the true nature of the high temperature phase is elucidated beyond the traditional Landau-like explanation.

In Li-ion battery electrodes, phase transitions due to atomic redistribution with changes in Li concentration occur with insertion (removal) of Li-ions during discharge (charge). A comprehensive study of the thermodynamics and the non-dilute Li-diffusion mechanisms

in spinel-$Li_{1+x}Ti_2O_4$ is performed. Two distinct phases are predicted at different lithium compositions. The predicted voltage curve qualitatively matches with experimental observation. The predicted fast diffusion arises from crystallographic features unique to the spinel crystal structure elucidating the crucial role of crystal structure on Li diffusion in intercalation compounds.

Effects of anion and guest species on diffusion are elucidated with Li- and Cu-diffusion in spinel-Li_xTiS_2. We predict strong composition dependence of the diffusion coefficients. A unique feature about spinel-Li_xTiS_2 is that the intermediate site of a Li-hop is coordinated by four Li-sites. This results in di- and triple-vacancy mechanisms at non-dilute concentrations with very different migration barriers. The strong dependence of hop mechanisms on local Li-arrangement is at the origin of large concentration dependence of the diffusion coefficients. This contrasts with spinel-Li_xTiO_2 where the transition states are coordinated only by the end states of the hop, thereby restricting hops to a single vacancy mechanism. Cu ions are predicted to have much slower diffusion rate in TiS_2 host compared to Li ions.

Chapter 1

Introduction

The advancement of computational capacities of modern day computers and developments of efficient theoretical tools have rendered the field of computational material science effective and practical in understanding and predicting key material properties. Density functional theory can accurately calculate the electronic structure and energy associated with an arrangement of atoms.[1-5] Statistical mechanics acts as the theoretical bridge between finite temperature thermodynamic and kinetic properties and the energy landscape of atomic arrangements and the excitations of atoms and electrons.[6-10] In the present thesis, the link between ab-initio energy calculation and the macro-scale properties will be demonstrated, particularly in chapter 2. New contributions in developing models for structural phase transitions and the use of statistical mechanics for understanding non-dilute interstitial diffusion will be emphasized in this chapter. In chapter 3, this methodology will be applied to elucidate structural phase transformations with a particular focus on the cubic to tetragonal phase transformation in stoichiometric TiH_2. In chapters 4 and 5, the thermodynamics and kinetics of intercalation processes in Li-ion battery electrodes will be presented. Some fundamental insights about diffusion processes, the role of crystal structure and features of the network of interstitial sites will be explained in these chapters. In chapter 6, diffusion of copper ions will be presented in comparison to the Li ions in the same crystallographic host structure. The role of guest species in the diffusion process and some practical consequences of it will be emphasized. We will conclude the thesis in chapter 7 revisiting the original ideas and insights it would provide.

Phase transformations in materials can occur due to the variation of numerous external factors such as temperature, chemical composition, electromagnetic fields, stress fields.[11, 12] Various properties are associated with different kinds of phase transitions and technological applications of materials exploit these property variations. Solidification is an example of a liquid to solid phase transformation where physical properties of the material change with a change in temperature. A ferromagnetic to paramagnetic transition is associated with the change in magnetic properties.[13] Certain metals transform to a superconducting phase at extremely low temperature.[13, 14] To exploit these changes in properties, it is crucial to understand the nature of the phase transitions and the factors controlling them at a fundamental level.

The various types of phase transitions can be classified on several levels. A first-order phase transition causes a discontinuity of the slope of the free energy of the material. A second-order phase transition is usually accompanied by a divergence of the second derivative of the characteristic free energy.[7, 11, 12] Solid to liquid phase transformations are classic examples of a first-order transformation as the discontinuity is observed in density which is related to a first order derivative of free energy with respect to pressure. On the basis of the long-range movement of the atoms, one can define diffusive and displacive phase transformations.[13] In displacive transformations, the transition between two phases occurs without long-range diffusion of atoms while atoms travel from one region to the other during diffusive transitions.

In the present thesis, we focus on two very important classes of phase transitions: structural transformations and transformations due to atomic redistribution. In a broad sense, structural phase transitions cover all kinds of transformations involving a change in crystal structure without a change in composition. The diffusional tranformations or transformations due to atomic redistribution through diffusion involve changes in material properties due to different arrangements of atoms (order/disorder) or compositions of atoms, without altering the crystal structure. Both of these are observed in many technologically important materials. Often both the structural and diffusional transitions are commonly observed simultaneously during heat treatment of steel.[15, 16]

Structural phase transformations are exploited in shape memory alloys for smart materials.[17-19] On the other hand, in any open system where chemical composition of one or more components can change, different atomic distributions can be energetically favorable at different compositions. The redistributional phase changes occur, for example, during each charge-discharge cycle of modern-day rechargeable batteries.[20, 21] In many of these material systems, structural phase transformations accompany the redistributional phase transformations.

The first major focus of the present thesis is explaining thermally activated phase transitions where the high temperature phase is predicted to be mechanically unstable at 0 K. It is difficult to explain this behavior with the traditional assumptions in modeling structural phase transformations. Our study will introduce key ideas to explain the high temperature and high symmetry phases and bring insights for the structural phase transitions in general. The other area of focus is the thermally activated diffusion process especially within Li-ion battery electrodes. While diffusion behavior at non-dilute concentrations is a key factor in determining the efficiency of an electrode, very little is understood at a fundamental level. The effect of crystal structure and chemical composition on Li diffusion will be elucidated with several examples discussing critical insights for future material design.

Structural phase transformations occur through a diffusionless mechanism, where both strain energy and interfacial energy play a major role.[22] In one kind of structural phase transformation, the relative positions of atoms change with/without minor shape change.[23, 24] It involves small movements of atoms and it affects only the symmetry of the structure. When homogeneous distortive lattice strains are involved in the transformation, the underlying Bravais lattice changes to a different one. The cubic to tetragonal transformation is an example of a homogeneous distortion and is very common in materials of technological importance.[25-37] The austenite to martensite transition in steel is of this type and hence the common terminology for structural phase transitions due to the distortive lattice strain is a *martensitic transition*. Landau theory [12, 13, 38] rationalizes these transformations by introducing a coarse-grained free energy, expressed

as a function of an internal order parameter that characterizes the extent of the phase transformation. The conventional explanation of a structural phase transformation with changes in temperature assumes the mechanical stability of both phases. For a first order cubic to tetragonal transition, a Landau description assumes two local minima in the free energy as a function of tetragonality (c/a ratio, where c is the tetragonally distorted lattice parameter and a is the length of either of the other two lattice vectors of equal magnitude). As temperature changes, the shape of the free energy curve changes in a way that preserves the double-well nature while shifting the relative depths of the wells. This is schematically shown in fig 1.1 for a first-order cubic to tetragonal transition. The change in free energy curve with temperature is due to electronic and vibrational excitations at the atomic scale. The dependence of free energy on atomic scale vibrations are often assumed to be harmonic (the equilibrium position of atoms are at a steep energy well and the displacements from the equilibrium positions are small).[39] However, these assumptions can be far from the reality in many cases due to the predicted mechanical instability of observed high symmetry phase.[40-42] One such example will be discussed in chapter 3 and the idea can be extended to studies of many similar transitions.
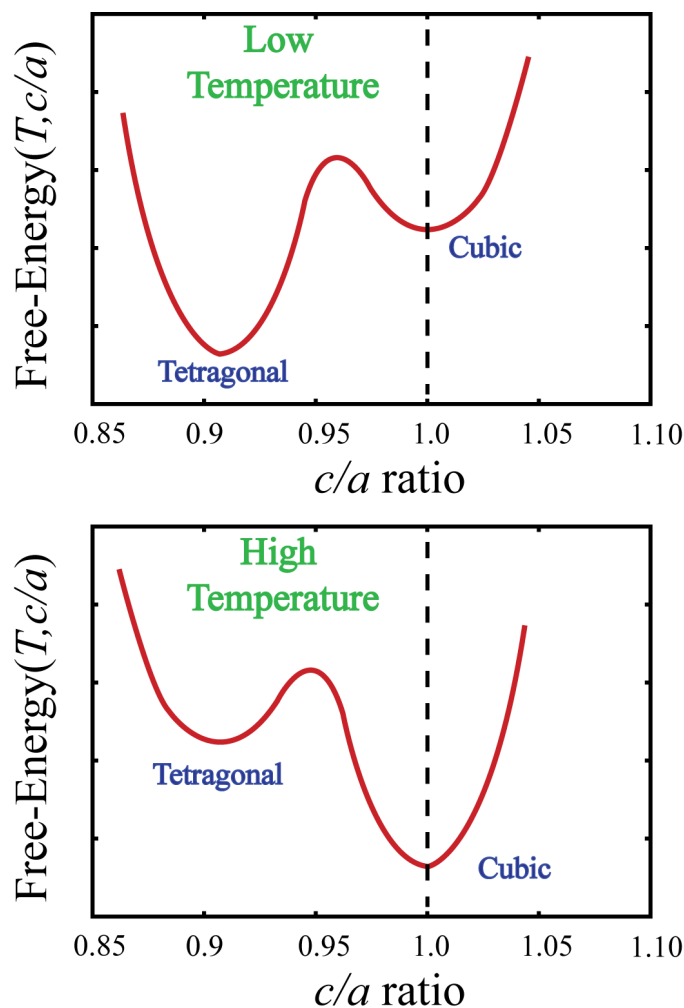
FIG 1.1: Conventional explanation of tetragonal to cubic phase transformation with increase in temperature. (a) At low temperature, free energy curve has a deeper local minimum at tetragonal state compared to the cubic state. (b) At high temperature, the shape of the free energy curve changes so that the cubic state becomes more stable compared to the tetragonal state.

Redistributional phase changes occur in many electrode materials during the charge and discharge of Li-ion batteries. In a Li-ion battery, Li^+ ions get transported between cathode and anode through an electrolyte with high ionic conductivity but zero electronic conductivity. The electrodes are typically made of intercalation compounds with relatively open but rigid host structures where Li-ions can fill the interstitial sites without major irreversible structural modifications.[21, 43-48] The open circuit voltage of a cell

is determined by the difference in Li chemical potentials between cathode and anode. To maximize the average voltage of a Li battery, it is desirable to combine a high-potential cathode with a low potential anode. The most common anode material is carbon in graphitic form.[21, 47, 49-52] Li-ions can intercalate between the graphitic sheets and the flexible crystal structure of graphite allows for easy insertion and extraction of Li-ions. It provides very low voltage (0.1-0.2 V) which makes it attractive as an anode.

Cathodes, on the other hand, are typically made of transition metal dichalcogenides.[21, 43] Transition metals such as Co, Ti, Mn, Ni, V form sulfides and oxides which have stable host structures that can intercalate Li ions. Removal (charging) and re-insertion (discharging) of Li-ions often do not significantly or irreversibly alter the structure. The structures of the transition metal dichalcogenides are reasonably open so that Li-ions can intercalate at ease. In early years, transition metal sulfides were used as the cathode.[53-55] The sulfides (such as Li_xTiS_2) were kinetically very favorable for the intercalation process.[53, 56-58] Oxides were chosen over sulfides in later years because of higher voltage. The most common cathode material in modern day Li-ion battery is Li_xCoO_2.[43-45, 59] Other commonly used single transition metal oxides are $Li_xMn_2O_4$, Li_xTiO_2, Li_xVO_2, Li_xFeO_2, Li_xNiO_2 etc.[60-65] Intercalation compounds having more than one transition metals such as $Li_xNi_{1-y}Co_yO_2$, $Li_x(Mn_{0.5}Ni_{0.5})O_2$ are also actively pursued to combine the advantages of different single metal oxides.[66-68] Other than the transition metal dichalcogenides, olivines (Li_xMPO_4 where M = Fe, Mn, Co, Ni) form another class of cathode materials.[46, 69] They are the latest electrode materials and proved to be very attractive because they are much less expensive than the transition metal oxides. These intercalation compounds show a variety of crystal structures. Many of the transition metal dichalcogenides such as Li_xCoO_2, Li_xTiS_2, $Li_x(Ni_{1/2}Mn_{1/2})O_2$ have a layered crystal structure where Li ions reside on two-dimensional sheets between the transition metal oxide/sulfide slabs. Compounds such as $Li_xMn_2O_4$ and Li_xTiO_2 prefer to be in spinel crystal structure. Li sites in the spinel host forms a three dimensional network. In olivine crystal structure (e.g., Li_xFePO_4) Li diffusion occurs through one-dimensional channels. The large variety of crystal structures immensely influences the redistributional phase change and the diffusion process.

Along with capacity and cycle life, charge-discharge rate is a crucial criterion in Li-ion battery design. Discharge rate determines the power level of a battery. The rate of charging remains a critical bottleneck in applying Li-ion technology where fast-charging is an essential criterion such as in electric vehicles. The charge-discharge rate is critically controlled by the ionic diffusion through the cell. The electrolytes allow fast diffusion of Li-ions. Hence diffusion in electrodes typically determines the overall rate of the process. The kinetics often has influence on not only the rate but also the voltage curve for a material. Nevertheless, the diffusion behavior remains poorly understood in many of the modern electrode materials. Typically, the diffusivities in the intercalation compounds have strong dependence on the Li composition.[56, 70] This composition dependence of diffusivities can be critical in determining the optimal rate of charge/discharge for achieving the full capacity. The effect of crystal structure and chemical species on the composition dependence is not well understood. The present thesis contributes to the understanding of these control factors at a fundamental level.

Diffusion behavior is intrinsically difficult to measure experimentally for individual electrodes. Computational techniques such as molecular dynamics are also not ideal to study kinetics for a long-timescale (slow) process such as diffusion involving the cumulative effect of many atoms performing a large number of hops. In this thesis, we will apply an established approach[70] based on statistical mechanics combined with ab initio calculations to understand diffusion in intercalation compounds and in particular, elucidate the role of crystal structure, anion chemistry and diffusing species(Li versus Cu). We will discuss the general formalism based on first-principles energy calculations, cluster expansion and transition state theory in chapter 2. Application of statistical mechanical tools such as kinetic Monte Carlo simulations enables us to determine macroscopic properties such as chemical diffusion coefficients. In chapter 4, we examine Li diffusion in spinel-Li_xTiO_2 as diffusion is fast in this material and the role of crystal structure in affecting diffusion will be explained. In chapter 5, diffusion behavior is studied in the spinel-Li_xTiS_2 with the same crystal structure as spinel-Li_xTiO_2. However, the change of anion alters the site preference for Li intercalation. The role of coordination in the interstitial Li site network is shown to have a crucial influence on diffusion

kinetics. In chapter 6, Cu diffusion is looked into in the same spinel titanium sulfide to understand how the choice of guest species influences the diffusion behavior.

Chapter 2

Methodology

2.1 Introduction

The present thesis relies on first-principles computational techniques to understand thermodynamic and kinetic properties of solids. The link between first-principles electronic structure calculations and macroscopic material properties is established with statistical mechanics. Statistical mechanics defines macroscopic equilibrium properties as long time scale averages of short time scale excitations (microstates) due to atomic and electronic fluctuations. The probability of a particular microstate being sampled is a function of the energy of that microstate. Hence, a statistical mechanical description of the solid state crucially depends on the calculation of the energy of a microstate. Due to the large number of possible microstates under a certain set of thermodynamic boundary conditions, it is impossible to calculate energies for all the microstates from first principles. An effective Hamiltonian enables the extrapolation to the large number of excitations, that contribute to average thermodynamic properties, of a limited number of quantum mechanical energy calculations. The effective Hamiltonians can be subjected to statistical tools such as Monte Carlo simulations to sample different microstates and calculate macroscopic properties as a weighted average of those microstates. Kinetic properties such as diffusion coefficients can also be modeled from small fluctuations that occur at the thermodynamic equilibrium. In the present chapter, we will look into the basics of statistical thermodynamics, different types of effective Hamiltonians and review first-principles calculations that are essential for parameterization of the effective Hamiltonians. In the later part of this chapter, we will discuss the construction of

configurational Hamiltonians by cluster expansion method, the relevant basics of Monte Carlo algorithms and the atomic scale formulation of solid state diffusion.

2.2   Basics of Statistical Thermodynamics

The thermodynamic description of a material is blind to its atomic scale details, though the root of all macro-scale manifestations of the material properties is in the atomic scale phenomena. Statistical mechanics acts as the theoretical bridge between these two scales. Properties of a material under thermodynamic equilibrium do not change with time, while at the atomic scale, the material system samples different microstates due to thermal fluctuations. A microstate refers to a particular electronic and vibrational excitation at the atomic scale for a particular arrangement of atoms. Each microstate has an energy. The observation time in a thermodynamic measurement is significantly larger than the typical time scale of the atomic level thermal fluctuations and over this thermodynamic time scale, many atomic scale microstates are sampled by the material. Therefore, the time-invariant macroscopic properties are the time averages of these micro-scale microstates.[6, 7]

Each microstate (σ) has an energy E_σ, which in principle can be calculated using quantum mechanics by solving Schrodinger equation. For a solid at constant temperature, T, volume, V and number of atoms, N, the probability that the solid is in the microstate σ is, according to statistical mechanics, given by

$$\underline{P}(\sigma) = \frac{\exp\left(-E_\sigma / k_B T\right)}{Q} \tag{2.1}$$

where k_B is the Boltzman's constant and Q is called the partition function.[6] The partition function is a normalization factor, which is the summation of the exponential functions corresponding to all possible microstates of the system under the imposed thermodynamic boundary conditions. It is defined as

$$Q = \sum_\sigma \exp\left(-E_\sigma / k_B T\right) \tag{2.2}$$

10

The free energy, *F,* or the characteristic potential associated with the particular set of the chosen boundary conditions is related to the partition function according to

$$F = -k_B T \ln(Q)$$ (2.3)

For constant *T, V* and *N* (called canonical ensemble), the free energy is called Gibbs free energy and thermodynamic equilibrium is represented by the minimum Gibbs free energy locus.

The statistical mechanical study of the macroscopic properties critically rely on the evaluation of the energies of different microstates. To calculate these energies for a large number of possible microstates, we need a model that accurately describes the functional relationship between the energy and the associated degrees of freedom for all the microstates. The model function for energy is called an effective Hamiltonian. The predictability of the statistical mechanical description of an equilibrium process is substantially controlled by the accuracy of the associated effective Hamiltonian. In the next section, we will discuss the effective Hamiltonians for the processes relevant to the present thesis.

2.3 Effective Hamiltonians

For solids, important microstates involve the electronic, vibrational and the configurational (atomic arrangements) degrees of freedom. Any microstate can be expressed as a linear combination of these excitations. Any one or more than one type of these excitations can play crucial role in the equilibrium behavior of the particular solid. The excitations, which do not directly take part in determining the macroscopic thermodynamic behavior, can be coarse-grained[13, 71] to simplify the relevant statistics and to eliminate unnecessary computation. The coarse-graining idea is based on the fact that all these different excitations are associated with time-scales that vary by a few orders of magnitude. In the present study, the vibrational (in case of cubic to tetragonal phase transformations) and the configrational (in case of the Li-intercalation in Li-ion battery electrodes) excitations have major roles.

A Hamiltonian that takes the important degrees of freedom into account can be used to map a physical process accurately. Here we discuss the role of two major degrees of freedom in solids and how we can construct Hamiltonians to model them.

2.3.1 Vibrational Hamiltonians

At finite temperature, the atoms in a crystalline solid vibrate about their mean position due to thermal excitations. Many structural phase transitions are associated with these thermally active vibrational excitations of the constituting atoms. Different modes of the relative vibrations among the atoms in a solid can be constructed with the help of linearly independent set of quasi-particles (phonons).[39, 72] Phonon-dispersion curves depict the relationship between the frequency (which also defines energy) and the wave vectors. To study these vibrational modes and their effects on the structural phase transitions, one needs an effective Hamiltonian that can generate all relevant microstates for different set of individual displacements. The most common approach to model this kind of Hamiltonian is by considering harmonic springs between the lattice sites. The potential energy can be written as a Taylor expansion with respect to the displacements of individual lattice sites from their equilibrium position. For the simplest case of one-dimensional lattice, it takes the following form.[6]

$$U(\xi_1, \xi_2, ..., \xi_N) = U(0,0,...., 0) + \sum_{j=1}^{N} \left(\frac{\partial U}{\partial \xi_j} \right)_0 \xi_j + \frac{1}{2} \sum_{i=1}^{N} \sum_{j=1}^{N} \left(\frac{\partial^2 U}{\partial \xi_i \partial \xi_j} \right)_0 \xi_i \xi_j + ... \tag{2.4}$$

The zero subscript associated with the derivatives indicates that the derivatives are calculated at the equilibrium position. The second term in the right hand side is zero, as energy is the minimum at the equilibrium position. The first term is a constant, which is the minimum energy of the lattice at equilibrium. This term acts as an additive constant and does not contribute to the energetics. The first significant term in the expression is the third term that involves the second derivative of the energy. This term corresponds to the simple harmonics and truncation after this term is called the *harmonic approximation*.[6, 39]

Vibrational energy of the lattice can also be expressed as a function of the strain matrix at individual lattice sites if the relative displacements of the basis atoms are negligible. Similar to the displacement Hamiltonians, the strain Hamiltonians can be harmonic or anharmonic according to the truncation order. Construction and parameterization of the vibrational Hamiltonian allow us to study the finite temperature thermodynamic behavior of a solid under thermal excitations.

2.3.2 Configurational Hamiltonians

For Li-ion battery electrodes, lithium ions can occupy the interstitial sites in a host structure of transition metal dichalcogenides. Lithium ions and vacancies can arrange in different orders over the available interstitial sites. Each unique arrangement represents a configurational microstate and is associated with a unique energy. The functional relationship between the configurational excitation and the energy of the solid is represented by the configurational Hamiltonians. The configurational degrees of freedom play a major role in the intercalation thermodynamics and hence configurational Hamiltonians have wide significance in this thesis. Cluster expansion is a rigorous tool for constructing the cofigurational Hamiltonians. We will discuss the basics of cluster expansion in section 2.5.

An effective Hamiltonian needs to be parameterized to accurately reproduce the energies of a large number of possible microstates. The input for the parameterization is a set of calculated energies for a finite number of microstates. We rely on the first principles for calculating these input energies. The basics of first-principles calculations are presented in the following section.

2.4 First-principles calculations

The starting point of any electronic structure calculation is the quantum mechanical time dependent Schrodinger equation [73-76] as shown below:

$$-\frac{\hbar^2}{2m}\nabla^2\Psi(\vec{r},t)+V(\vec{r},t)\Psi(\vec{r},t)=i\hbar\frac{\partial\Psi(\vec{r},t)}{\partial t} \tag{2.5}$$

This equation acts as the pivot of quantum mechanics just as Newton's laws of motion do for the classical mechanics. The first term is the kinetic energy while the second one is the potential energy term or the effect of the external potential driving the motion of the particle. The right hand side term is the time evolution term for the wave function Ψ. Ψ contains all available information about the system. Within Born-Openheimer approximation and considering only the electrons of the system, the external potential $V(\vec{r})$ can be approximated as time-invariant.[5, 39, 76] The time-independent part of equation 2.5 is called stationary Schrodinger's equation and it can be written in the following form:

$$H\Psi(\vec{r}) = E\Psi(\vec{r}) \tag{2.6}$$

where, H is the Hamiltonian operator expressed as $H = \left[\left(-\frac{\hbar^2}{2m}\nabla^2\right) + V(\vec{r})\right]$ and E is a scalar representing the total energy of the electron. The goal of first-principles calculations is to solve equation (2.6) for the electrons in the material and calculate the probability distribution, energy eigen states of the electrons and the total ground-state energy.

The Schrodinger equation can be solved starting with the orbital description (e.g. Hartee-Fock.[1, 2, 39, 76]) or starting with the electron density description. The Hartee-Fock method works well for small molecules and becomes extremely complex for bulk solids. Therefore, electron density description is used for calculating electronic structure for the bulk solids.

Electron density can be defined as the probability of finding any of the N electrons within the volume element $d\vec{r}$ but with arbitrary spin while the other N-1 electrons have arbitrary positions and spin in the state represented by ψ.[2] It is an observable unlike ψ and can be measured by X-ray diffraction. Hohenberg-Kohn theorem formally established the one to one correspondence between this electron density and the external potential, hence to the Hamiltonian: "The external potential $V_{ext}(\vec{r})$, within a trivial

additive constant, is a unique functional of the electron density $\rho(\vec{r})$; since, in turn $V_{ext}(\vec{r})$ fixes $\hat{H}$, we see that the full many particle ground state is a unique functional of $\rho(\vec{r})$".[77]

Based on the Hohenberg-Kohn theorem, we can write the ground state energy according to

$$E_0[\rho_0] = T[\rho_0] + E_{ee}[\rho_0] + E_{Ne}[\rho_0] \tag{2.7}$$

Where the first term in the right hand side is the kinetic energy, the second term is the electron-electron interaction energy and the last term is the nucleus-electron interaction energy, all written as a function of the electron density.

If we write the energy due to nucleus-electron interaction as a function of the electron density,

$$E_{Ne}[\rho_0] = \int \rho_0(\vec{r}) V_{Ne} d\vec{r} \tag{2.8}$$

the energy expression takes the following form:

$$E[\rho_0] = \int \rho_0(\vec{r}) V_{Ne} d\vec{r} + T[\rho_0] + E_{ee}[\rho_0] \tag{2.9}$$

The first term in the right hand side depends on the relative positions of the nuclei in the system and hence it is a system dependent part. However, the other two terms in the right hand side are system-independent or universal. Collecting these system independent terms into a new quantity, called the Hohenberg-Kohn functional $F_{HK}[\rho_0]$, we arrive at

$$E[\rho_0] = \int \rho_0(\vec{r}) V_{Ne} d\vec{r} + F_{HK}[\rho_0] \tag{2.10}$$

If the Hohenberg-Kohn functional is evaluated for some arbitrary $\rho(\vec{r})$, it gives the sum of kinetic energy and the electron-electron repulsion energy with the ground state wave function ψ for this $\rho(\vec{r})$. This ψ delivers the lowest energy among many possible wave functions that yield $\rho(\vec{r})$. This functional is very important in the sense that if we knew

this functional exactly, we could have solved many-body Schrodinger equation *exactly*, not approximately. In reality, forms of both kinetic energy term and electron-electron repulsion term are not known. A part of the electron-electron repulsion term can be written as the classical Coulomb potential and the rest of it can be expressed with an unknown non-classical potential in the following manner.

$$E_{ee}[\rho] = \frac{1}{2} \iint \frac{\rho(\vec{r}_1)\rho(\vec{r}_2)}{r_{12}} d\vec{r}_1 d\vec{r}_2 + E_{ncl}[\rho] \tag{2.10}$$

Modeling of this non-classical part is the major challenge to any density based method of solving the Schrodinger equation. The second theorem of Hohenberg and Kohn makes use of the variational principle and establishes the method as a 'ground-state-only' method.

Though Hohenberg and Kohn established electron-density as the key quantity in solving the ground-state electronic structure, initial density-based attempt on solving multi-electron systems was formulated by Llewellyn Thomas and Enrico Fermi shortly after the introduction of the Schrodinger equation.[1, 2]

2.4.1 Density Functional Theory

Density functional theory (DFT) serves as the most widely used method in the field of computation of electronic structure and ground state total energies. DFT uses the advantages of both orbital based methods and the density based methods. While the direct use of the density functional in the Hamiltonian reduces the number of variables by great deal, the functional are not known in terms of the electron density. Kohn and Sham introduced the concept of a non-interacting reference system with one-electron orbitals such that the major part of the kinetic energy can be computed with high accuracy.[78] The remaining part is fairly small and is combined with the non-classical part of the electron-electron interaction energy ($E_{ncl}[\rho]$). The use of both orbital approach and density approach makes DFT computationally viable while not sacrificing accuracy by a great deal.

In Hartee-Fock approach, a single Slater determinant determined from N spin orbitals describes the state of the system. This Slater determinant represents exactly the wave function for N spin orbitals if and only if they are non-interacting. For this non-interacting wave function, the kinetic energy can be expressed exactly as

$$T_{HF} = -\frac{1}{2} \sum_{i=1}^{N} \left\langle \chi_i \middle| \nabla^2 \middle| \chi_i \right\rangle \tag{2.11}$$

The spin orbitals (χ_i) are chosen so that the expectation value of the energy expression (E_{HF}) attains the minimum.

On this same non-interacting system, it is possible to introduce a Hamiltonian of the following form:

$$H_s = -\frac{1}{2} \sum_{i=1}^{N} \nabla_i^2 + \sum_{i=1}^{N} V_s(\vec{r}_i) \tag{2.12}$$

where $V_s(\vec{r})$ represents the effective local potential that the electron experiences. As the Hamiltonian operator does not contain any electron-electron interaction term, it is a Hamiltonian for the non-interacting reference system. This method of forming a multi-electron Hamiltonian from non-interacting single electron Hamiltonians is very similar to that introduced by Hartee and Fock. The only difference is in using a local effective external potential due to all other nuclei and electrons in the system. These orbitals are called Kohn-Sham orbitals. The connection between this hypothetical system to the real system lies in the form of the effective potential. The density determined from these Kohn-Sham hypothetical orbials (φ_i) has to equal the ground state density of the real interacting electrons system.

$$\rho_s(\vec{r}) = \sum_{i}^{N} \sum_{s} \left| \varphi_i(\vec{r}, s) \right|^2 = \rho_0(\vec{r}) \tag{2.13}$$

By calculating the major part of the unknown kinetic energy with exact kinetic energy expression for non-interacting electrons (equation 2.11), Kohn and Sham introduced the following separation of the functional:

$$F[\rho(\vec{r})] = T_s[\rho(\vec{r})] + J[\rho(\vec{r})] + E_{XC}[\rho(\vec{r})] \tag{2.14}$$

E_{XC} is called the exchange-correlation energy and is defined by:

$$E_{XC}[\rho] = (T[\rho] - T_s[\rho]) + (E_{ee}[\rho] - J[\rho]) = T_C[\rho] + E_{ncl}[\rho] \tag{2.15}$$

It is important to note here that the exchange-correlation function contains all energetic contributions everything that is unknown: the residual part of the kinetic energy functional not determined from the non-interacting orbitals and the non-classical part of the electrostatic contributions (self-interaction, exchange and correlation corrections). Up to this point, the density functional theory is exact. All the approximations are made while modeling the exchange-correlation functional.

In light of the Kohn-Sham separation of the energy functional, the total energy of the solid as a function of electron density can be explicitly written in the following form.[2]

$$
\begin{aligned}
E[\rho(\vec{r})] &= T_s[\rho] + J[\rho] + E_{XC}[\rho] + E_{Ne}[\rho] \\
&= T_s[\rho] + \frac{1}{2} \iint \frac{\rho(\vec{r}_1)\rho(\vec{r}_2)}{r_{12}} d\vec{r}_1 d\vec{r}_2 + E_{XC}[\rho] + \int V_{Ne}\rho(\vec{r}) d\vec{r} \\
&= -\frac{1}{2} \sum_i^N \langle \varphi_i | \nabla^2 | \varphi_i \rangle + \frac{1}{2} \sum_i^N \sum_j^N \iint |\varphi_i(\vec{r}_i)|^2 \frac{1}{r_{12}} |\varphi_j(\vec{r}_j)|^2 d\vec{r}_i d\vec{r}_j \\
&\quad + E_{XC}[\rho(\vec{r})] - \sum_i^N \int \sum_A^M \frac{Z_A}{r_{1A}} |\varphi_i(\vec{r}_1)|^2 d\vec{r}_1
\end{aligned}
\tag{2.16}
$$

The exchange-correlation functional (E_{XC}) cannot be written in any explicit form. We can now apply the variational principle and find the condition that the wave function must satisfy to minimize the above energy expression. The condition can be derived to have the following form:

$$\left(-\frac{1}{2}\nabla^2 + \left[\int \frac{\rho(\vec{r}_2)}{r_{12}}d\vec{r}_2 + V_{XC}(\vec{r}_1) - \sum_A^M \frac{Z_A}{r_{1A}}\right]\right)\varphi_i = \left(-\frac{1}{2}\nabla^2 + V_{eff}(\vec{r}_1)\right)\varphi_i = \varepsilon_i\varphi_i \qquad (2.17)$$

By comparing the above equation to the Schodinger equation for a single electron in the non-interacting reference system, it becomes obvious that the term in the square brackets or V_{eff} is identical to the external potential V_s in equation 2.12.

While the Kohn Sham equation resembles the single electron stationary Schrodinger equation, V_{eff} depends on the solution such that the equation has to be solved in a self consistent iterative way.

The exchange correlation energy ($E_{XC}[\rho(\vec{r})]$) is the quantity where all approximations in density functional theory are contained. The first and the most common approximation to model this quantity is called the Local Density Aprroximation (LDA).[78] In this approximation, E_{XC} takes the following form:

$$E_{XC}[\rho] = \int \varepsilon_{XC}[\rho]\rho(\vec{r})d\vec{r} \qquad (2.18)$$

Here, ε_{XC} is the exchange correlation energy density (per unit electron-density). The quantity ε_{XC} is estimated from the value with uniform electron gas with the same density ($\rho(\vec{r})$). This approximation was first put into calculations by Ceperly and Alder (1980).[79] This approach is well suited for solids with delocalized electronic states as the electron density structure is similar to that of a homogeneous electron gas. For individual atoms and molecules, the electron density varies more rapidly rendering LDA a crude approximation.

Instead of using the uniform electron density, the gradient in density can be taken into account to handle the inhomogeneities. However, there is an intrinsic problem in using density gradients. LDA satisfies the symmetry and the scaling properties of the hypothetical exact exchange correlation potential and direct introduction of gradients disrupts this requirement. Perdew introduced a generalized gradient approximation

19

(GGA) which takes care of these requirements.[80, 81] GGA works better than LDA for individual atoms and molecules but it is more complex.

Approximations to density functional theory are associated with certain limitations. LDA underestimates the lattice parameter while GGA overestimates it. LDA also underestimates the band gaps. However, in case of studying the intercalation behavior in transition metal dichalcogenides, it is the formation energies that dictate the thermodynamics. Many errors in the total energy cancel out. GGA is very important in case of magnetic systems and is generally believed to be more accurate than LDA. We have used GGA[82] in all the first-pirnciples calculations in this thesis.

In practical DFT calculations, the core electrons are often represented by a pseudo potential and hence not solved explicitly.[83, 84] This approach is valid as long as the core electrons do not take part in bonding and their energy levels are not shifted when placed in different surroundings. For calculating the bulk properties of crystalline solids, DFT calculations are performed under periodic boundary condition. This periodic condition allows us to apply Bloch's Theorem[39] and solve for a limited number of orbitals specified by a wave number $\vec{k}$ in the reciprocal space of the solid. The orbital energy levels are continuous functions of $\vec{k}$. Therefore they can be solved for a finite number of $\vec{k}$ points and the intermediate values can be interpolated with some suitable scheme. The orbitals are expanded as the sum of plane waves with periodicity of the reciprocal lattice with a pre-selected cutoff for the maximum energy. In the present thesis, we have used PAW (Projector Augmented Wave)[85] pseudopotentials as incorporated in VASP (Vienna Ab-initio Simulation Package)[86-88].

The First-principles calculation methods allow us to calculate the total energies of microstates which are essential input for constructing an effective Hamiltonian. Accurate parameterization of the effective Hamiltonian is the next step in statistical mechanical formulation. For redistributional Hamiltonian, cluster expansion is an established rigorous tool for the parameterization. In the nest section, we will review the basics of the cluster expansion technique.

2.5 Cluster expansion

Cluster expansion is a technique of formulating an effective Hamiltonian to account for configurational degrees of freedom. It has been widely used in alloy theory and can be efficiently used for the modeling of the intercalation process. Intercalation compounds consist of a host crystal structure (typically of transition metal oxide, sulfide or phosphates) that remains the same throughout the intercalation process (except slight relaxation in volume and shape). The interstitial sites within this host structure are available for Li occupancy. In a crystal of M sites, there are 2^M ways of distributing Li ions and vacancies. In a real solid, ionic relaxations do not allow the Li-ions to stay exactly at the crystallographic interstitial positions in the crystal. Nevertheless, it is always (for small relaxations) possible to relate the Li-ions (or vacancies) to the crystallographic sites through a one to one correspondence.
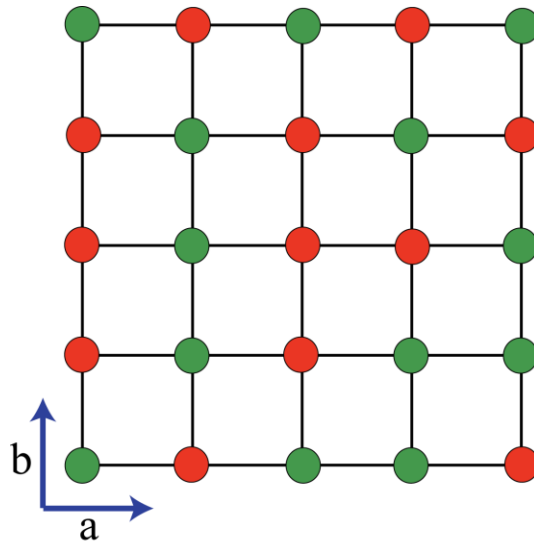
Fig 2.1: An example square crystal with the sites occupied by two different species (red and green)

In fig 2.1, we show a simple example of a square crystal where we can formulate a binary cluster expansion. Each site can be occupied either by a Li ion or by a vacancy. We can assign an occupation variable (σ_i) to the sight i which has a value +1 (-1) if there is a Li-

ion (vacancy). Any arbitrary arrangement of Li-vacancy can be uniquely represented by a vector of +1's and -1's:

$$\vec{\sigma} = \left(\sigma_1, \sigma_{2,}, \sigma_3 ... \sigma_i ... \sigma_M\right)$$ (2.19)
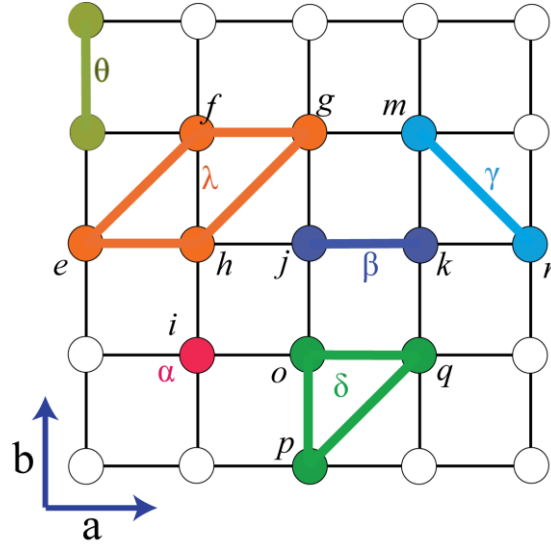
Fig 2.2: Examples of clusters of on a square crystal

On the same crystal, we can find clusters of different sizes (point, pair, triplet, quadruplet etc) as shown in fig 2.2 For a particular cluster, cluster function (ϕ) is defined as the product of the occupation variables at the member sites as shown below.[89]

$$\phi_\alpha(\vec{\sigma}) = \prod_{i \in \alpha} \sigma_i$$ (2.20)

As for an example, if cluster δ is a triplet cluster with two Li-ions and a vacancy at the constituent sites, ϕ_δ will be calculated as (+1) × (+1) × (-1). It can be rigorously proved that these cluster functions for all possible clusters in the lattice form a complete orthonormal basis set in configuration space and any property that depends on configuration can be *exactly* expanded as a linear combination of these basis functions.[89] It is similar to the discrete Fourier series and can be thought of as a generalization of the Ising Hamiltonian. The expansion takes the following form with the unknown parameters (V_α).

$$f(\vec{\sigma}) = V_0 + \sum_\alpha V_\alpha \phi_\alpha(\vec{\sigma}) \tag{2.21}$$

The unknown parameters (V_α) are called the effective cluster interactions (ECI). The ECI's are constant expansion coefficients and should not be confused with the inter-atomic potentials. The cluster expansion is defined strictly for a particular arrangement of interstitial sites. If more than one phase competes for stability having different crystal structures and hence different arrangement of interstitial sites, separate cluster expansions need to be formulated to describe the configurational degrees of freedom over the separate phases.

Symmetry of the underlying lattice has to be taken into account for the cluster expansion formalism.[90] In the square lattice shown in fig 2.2, all the lattice sites are symmetrically equivalent as any one site can be obtained by translating any other site by the linear combination of the lattice vectors. Moreover, the pair cluster θ can be obtained by rotating the cluster β by 90 degrees and subsequently translating it by $-2\vec{a} + \vec{b}$ vector. The rotation by 90 degrees is a member of the space group of the square lattice. A cluster is said to be symmetrically equivalent to another cluster if the first one can be constructed from the latter one by at least one member of the space group of the underlying lattice and a translation vector which is a linear combination of the lattice vectors. Therefore, the cluster θ is symmetrically equivalent to the cluster β. All the symmetrically equivalent clusters will have the same ECI.

Parameterization of the cluster expansion means finding the set of ECI's that reproduces the configuration-dependent variables of the material. For the intercalation process, the relevant variable is the formation enthalpy. Total energies for different Li-vacancy orderings are calculated from the first principles. The formation enthalpies can be calculated from these total energies using the laws of mixture. The quality of the cluster expansion is measured with two metrics: the root mean square (RMS) error and the cross validation (CV) score. The RMS error measures the reproducibility of the formation enthalpies and the cross validation score measures the degree of predictability.[91] In a set of *n* formation energies, we leave one out of the parameterization process and let the

cluster expansion predict the formation enthalpy for the left-out configuration. The less the RMS error and the CV score, the better the fit. We use the matrix inversion algorithm to find the least square fit of the ECI's. A genetic algorithm is used to find the set of optimal clusters that minimizes the CV score and the selection criteria puts more weight on the smaller clusters and adds one cluster only if all the smaller sub-clusters are included in the set.[92] The cluster function forms a complete basis set if the size of the clusters extends up to infinity. But any practical cluster expansion has to be truncated after a certain cluster size. For most of the materials, the cluster expansion consisting of up to four-point clusters have been successfully reproduced the formation enthalpies with reasonable accuracy. Moreover, it has been shown that the CV score of a cluster expansion decreases with the inclusion of larger clusters only up to a certain optimal size (different for different material) and then increases monotonically with the use of larger clusters.[91] As the CV score minimization is an essential criterion for an accurate cluster expansion, we do not use five point or bigger clusters in the cluster expansion in the present thesis.

2.6 Monte Carlo Methods

Monte Carlo Methods represent a class of statistical algorithms.[8, 93-96] It can be successfully applied to study equilibrium properties based on the principles of statistical thermodynamics. At certain boundary conditions, a system samples several configurations each with relative frequency consistent with the probability distribution (equation 2.1). The configurations form a Markov chain and the transition from one configuration to another is associated with certain probability. Over a large number of attempts (called Monte Carlo passes), statistical thermodynamics ensures that the free energy follows this probability distribution. Hence the mean value of that free energy represents the equilibrium free energy.

2.6.1 Canonical Monte Carlo

For a closed system under constant temperature and volume, the statistical ensemble we choose to study the thermodynamic equilibrium is called the canonical ensemble. The

control variables are *T*, *V* and *N*. Under this boundary condition, the characteristic potential is Gibbs free energy and the transition probability under standard Metropolis algorithm[97] is given by the following rule.

$$P = 1 \qquad\qquad \text{if } (E_2 - E_1) \leq 0 \qquad\qquad (2.22a)$$

$$P = \exp\left(-(E_2 - E_1)/k_B T\right) \qquad\qquad \text{if } (E_2 - E_1) > 0 \qquad\qquad (2.22b)$$

where, P is the transition probability for configuration 1 to transform to configuration 2. E_1 and E_2 are the corresponding energies for the two configurations. If this calculated probability is less than a random number between 0 and 1, then the new configuration (2) is accepted. Otherwise, the first configuration (1) is kept.

For the investigation of the cubic to tetragonal phase transitions, we defined one state by a set of lattice strain variables (compared to cubic reference lattice) of all the lattice sites in the computational domain. A change in any of the 6(N+1) strain variables (there are N sites in the domain and 6 independent strain metrics per site, and there are six strain variables for the homogeneous strain of the super cell) means a transition to another state of the system. As the system is a closed system with constant temperature and volume, the canonical Monte Carlo method has been applied to study the thermodynamic equilibrium. Energy of any state of the system is calculated from the effective Hamiltonian parameterized by the first-principles total-energy calculations.

2.6.2 Grand Canonical Monte Carlo

In case of Li-insertion in the intercalation compound, the number of Li-atoms is no longer constant. The control variables are temperature, volume and the external potential. External potential directly controls the chemical potential (μ). Therefore, we take *T*, *V* and μ as the control variables and the thermodynamics is studied with the help of the grand canonical ensembles. The characteristic potential in this case is called the grand canonical potential which is obtained from the following equation.

$$\Omega = E - \mu N \qquad\qquad (2.23)$$

where N is the number of Li atoms. The probabilities are calculated in the similar way except using this grand canonical energy (Ω) instead of the internal energy (E). By minimizing the grand canonical free energy, we can obtain the equilibrium relationship between Li-concentration and chemical potential of Li. This relationship is of importance for battery applications as the open circuit voltage of an intercalation compound electrode with respect to a metallic Li reference anode is related to the chemical potentials of the electrodes.

2.6.3 Kinetic Monte Carlo

Kinetic Monte Carlo is an efficient algorithm to capture the dynamics of the diffusing atoms. At any point of time, the system can jump to several possible end states. The individual atomic hops joining two such states of the system form a cumulative array. Each individual hop has some probability (Γ) of occurrence (according to equation 2.31 in section 2.7) and the whole array can be associated with the cumulative probability (Γ_{Tot}).[98] A random number (u_1) between 0 and 1 is generated and the event (i) is selected so that

$$\Gamma_i = u_1 \Gamma_{Tot} \tag{2.24}$$

The dynamic process is modeled as a continuous-chain Markov process that obeys Poisson statistics. Under this assumption, the hops are instantaneous and the process-time is updated by the time between the jumps. The time between the two states of the system follows the Poisson distribution function with a mean that is the reciprocal of the cumulative probability of the jump. Therefore, the time is updated by,

$$\Delta t = \frac{-\ln u_2}{\Gamma_{Tot}} \tag{2.25}$$

where u_2 is a random number between 0 and 1. The KMC algorithm is efficient because each iteration is guaranteed to produce a transition. In case of diffusion, we follow each Li-ions and record the displacement vectors and update the time after iteration. The averages shown in equation 2.28 and 2.29 (in section 2.7) are taken after a large number

of Monte Carlo passes. Also, for each concentration, we average the relevant quantities for different initial arrangement of Li and vacancies.

2.7 Atomic-scale Formulation of Diffusion

The diffusion coefficient, D, appearing in Fick's first law depends both on the thermodynamic as well as the kinetic properties of the solid. For Li diffusion over the interstitial sites of the host, it is convenient to write D as a product of a thermodynamic factor, Θ, and a self diffusion coefficient, D_J, according to[99]

$$D = \Theta D_J \tag{2.26}$$

The thermodynamic factor

$$\Theta = \frac{\partial\left(\dfrac{\mu_{Li}}{k_B T}\right)}{\partial \ln x} \tag{2.27}$$

measures the deviation from thermodynamic ideality. It is unity in the dilute limit where interactions between different Li ions are negligible and diverges close to an ordered stoichiometric phase where the deviation from ideal solution behavior is the largest. The self-diffusion coefficient measures the mobility of the Li ions over the interstitial sites and can be evaluated at equilibrium with a Kubo-Green expression:[100]

$$D_J = \frac{1}{2dt}\frac{1}{N}\left\langle \left[\sum_{i=1}^{N} \Delta \vec{R}_i(t)\right]^2 \right\rangle \tag{2.28}$$

where d is the dimension of the interstitial network, t is time, N is the total number of lithium ions and $\vec{R}_i(t)$ is the vector connecting the end points of the trajectory of the ith Li ion at time t. The self-diffusion coefficient, D_J, has a similar form as that of the tracer diffusion coefficient, D^*, which is defined as

$$D^* = \frac{1}{2dt}\frac{1}{N}\sum_{i=1}^{N}\left\langle \left[\Delta \vec{R}_i(t)\right]^2 \right\rangle. \tag{2.29}$$

The self-diffusion coefficient is related to the square of the displacement of the center of mass of all diffusing Li ions at equilibrium, thereby accounting for correlations in the trajectories of different Li ions. The self-diffusion coefficient is therefore a measure of the collective mobility of many Li ions. The tracer diffusion coefficient, D^*, in contrast, is related to the square of the displacement of one Li and therefore measures the mobility of individual Li ions. While D_J and D^* are metrics of the kinetics of diffusion, they also depend on the thermodynamic behavior of the solid. The mobility of Li ions can be very sensitive to the equilibrium degree of the short- and long-range order among the Li ions. Often mobility is reduced in the ordered phases having stoichiometric compositions as elementary hops will then introduce some degree of local disordering, which is often accompanied by a significant increase in the energy of solid.

The thermodynamic factor (Eq. 2.27), can be calculated with the grand canonical Monte Carlo simulations by evaluating[99]

$$\Theta = \frac{\langle N \rangle}{\langle (\delta N)^2 \rangle} \tag{2.30}$$

where N is the number of Li atoms in the system (Monte Carlo cell) and δN is the fluctuation around the average $\langle N \rangle$ at constant Li chemical potential μ_{Li}. Both D_J and D^* can be calculated with the kinetic Monte Carlo simulations, which simulates trajectories $\vec{R}_i(t)$ as a function of time. Essential input for a kinetic Monte Carlo simulation[98, 101] is an accurate description of the hop frequencies for the elementary Li-vacancy exchanges. These can be calculated with transition state theory, which for the Li-ion hops into an adjacent vacant site takes the form[102]

$$\Gamma = \nu^* \exp\left(\frac{-\Delta E}{k_B T} \right) \tag{2.31}$$

where ΔE is the activation barrier and ν^* is the vibrational prefactor. Often the Li ions are disordered over the interstitial sites of the host and can sometimes exhibit long-range order at stoichiometric compositions. The migration barriers ΔE appearing in the hop

frequency, Eq. 2.31, depends on the local Li composition and state of disorder and will therefore vary as the migrating ions sample different local environments along their trajectories.
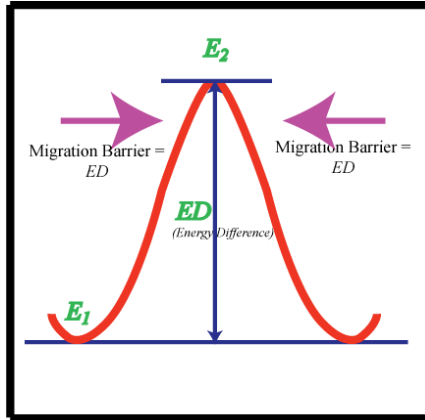
(a)
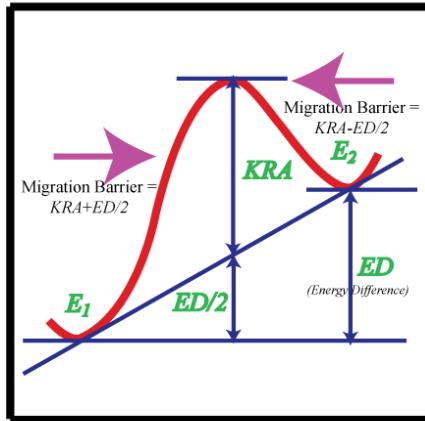
(b)
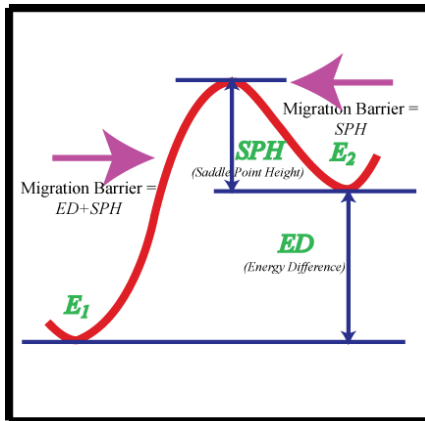
(c)

FIG 2.3: Different shapes of the energy path associated with a nearest neighbor atomic hop: (a) If the saddle point of the hop can be included in the cluster expansion, the migration barrier for any direction of the hop is calculated from the energy difference. Both stable site energy (E_1) and transition state energy (E_2) need to be calculated from the cluster expansion. (b) In case the transition state cannot be included in the cluster expansion, the migration barrier will depend on the direction of the hop. Kinetically resolved barrier (KRA) is the energy-height of the transition state from the straight line joining the end states of the hop (perpendicular to the direction of the hop and at the middle of the two end states). The middle point of the straight line joining the end states is higher by the energy difference from the lower end state. Depending on the hop-direction, we need to either add or subtract this quantity from KRA value to obtain the migration barrier. (c) In case of the transition state not included in the cluster expansion, we can use the direct differences of energies instead of KRA value to calculate the migration barrier.

Several approaches have been formulated and implemented to account for the dependence of migration barriers on local Li-vacancy disorder using a local-cluster expansion. If the transition state can be included in the cluster expansion, the migration barrier can be modeled from the direct difference in energies when the hopping Li stays at the stable site and when it is at the transition state (fig 2.1(a)). When the activated state is a local minimum, the forward migration barrier can be calculated by the summation of two quantities: (i) the kinetically resolved barrier (KRA)[70] and (ii) the difference in the end state energies as shown in fig 2.1(b). The backward migration barrier is calculated by the difference of these two quantities. When the energy height of the transition state from one of the end states remains constant with variations in the local arrangements, the constancy of this quantity can be used to model the migration barrier eliminating the need of a local cluster expansion. As the end state energies are reproducible with the global cluster expansion, the addition of a constant term (saddle point height) yields the migration barrier. The concept is explained schematically in fig 2.1(c). When none of these simplifications work for a solid, a local cluster expansion of the KRA values captures the dependence on the surroundings rigorously. In case of the α-$Li_{1+x}Ti_2O_4$, we

used the method explained in fig 2.1(a), In case of β-Li$_{1+x}$Ti$_2$O$_4$, two different KRA values were used for two different local environments. For modeling the migration barriers in Li$_x$TiS$_2$, third approach (fig 2.1(c)) was used and three different constant values for the saddle point height were used for three different local environments.

The vibrational prefactor (ν^*) in equation 2.31 is a measure of the attempt frequency of a hop. It can be calculated from the ratio of the products of two sets of frequencies according to the following equation as derived by Vineyard. [102]

$$\nu^* = \frac{\displaystyle\prod_{i=1}^{3N-3} \nu_i}{\displaystyle\prod_{i=1}^{3N-4} \nu_i^*} \qquad\qquad (2.32)$$

The numerator represents the product of all normal vibration frequencies at the initial site of the hop and the denominator represents the same at the saddle point. N stands for the number of sites involved in a hop and for a nearest neighbor Li-vacancy exchange, it is 2.

Chapter 3

Mechanical Instabilities and Structural Phase Transitions

3.1 Introduction

Many high temperature crystalline phases undergo structural phase transformations upon cooling. The modification in crystal structure often results in an abrupt change in materials properties. In some materials, a structural phase transformation is accompanied by a large strain, which can be exploited in shape-memory applications, while in others, the crystallographic changes lead to a spontaneous electric polarization within the crystal. A distinction can be made between structural transformations characterized by atomic displacements within a unit cell (type I), as occurs in most ferroelectric oxides, and structural transformations that produce large homogeneous strains (type II), as occurs for example in martensitic transformations involving a Bain distortion.

First-order structural phase transformations occur when the free energy of the high temperature phase crosses the free energy of the low temperature phase. The use of thermodynamic potentials to rationalize phase stability breaks down around a second-order phase transformation due to large fluctuations with diverging correlation lengths as the transition temperature is approached. Nevertheless, the phases participating in the structural phase transformation can still be described thermodynamically in terms of free energies away from the second order transformation temperature.

The conventional thermodynamic description of crystalline phases at finite temperature relies on the assumption of mechanical stability with respect to a homogeneous strain of the unit cell

and/or an internal shuffle of the atoms within the unit cell. This means that the energy or a coarse-grained free energy (when accounting for electronic excitations at finite temperature) should exhibit a local minimum for that crystal structure with respect to shape changes and atomic displacements. For mechanically stable crystal structures, free energies can be calculated within the harmonic (or quasi-harmonic) approximation,[103] while contributions from anharmonic vibrations are often neglected. Recent first-principles investigations of phase stability using various approximations to density functional theory (DFT),[77, 78] however, have shown that a large number of experimentally observed, high temperature phases are predicted to be mechanically unstable at zero Kelvin.[40-42, 104-110] Pure Ti, for example, has a bcc crystal structure above 1150K, while DFT based calculations at zero Kelvin predict that bcc Ti is mechanically unstable and should spontaneously relax to hcp, fcc or the ω phase.[40-42] Various approximations to DFT predict similar phenomena in ferroelectric materials with, for example, the high temperature cubic phases of $BaTiO_3$ and $PbTiO_3$ predicted to be unstable at zero Kelvin with respect to atomic displacements that lead to crystal structures with lower symmetry.[104-106]

First-principles effective Hamiltonians subjected to Monte Carlo simulations have brought fundamental insight about the nature of the anharmonic vibrational excitations that render the high symmetry phases stable at elevated temperature in systems exhibiting type I structural phase transformations, such as $BaTiO_3$ and $PbTiO_3$.[104-106] Far less, however, is understood about type II structural phase transformations involving large homogeneous strains. Here we show that anharmonic vibrational degrees of freedom can play a crucial role in stabilizing the high temperature phases that are both susceptible to a type II structural phase transformation and that are also predicted to be mechanically unstable at zero Kelvin.
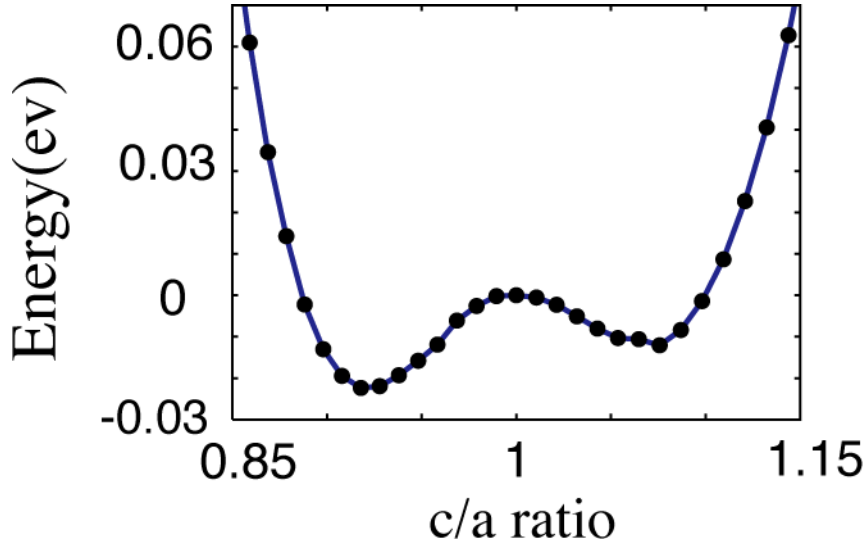
FIG 3.1: Energy of TiH_2 as a function of the *c/a* ratio as calculated within the generalized gradient approximation to DFT (energy is normalized per cubic unit cell, containing 4 Ti atoms and 8 H atoms).

An example of a type II structural phase transformation is the cubic to tetragonal phase transition of TiH_2. The Ti atoms of TiH_2 reside on an fcc sublattice while the H atoms occupy all the tetrahedral interstitial sites. At high temperature, TiH_2 has cubic symmetry but spontaneously transforms to a tetragonal phase below 300 K with a *c/a* ratio less than 1.[111] A first-principles calculation of the energy versus *c/a* ratio within GGA correctly predicts the tetragonal variant to have the lowest energy as illustrated in Fig. 3.1. (The energy versus *c/a*, normalized per cubic unit cell of TiH_2, was calculated with the VASP code[86, 87] using the projector augmented wave method.[85, 88]) Surprisingly, though, the high temperature cubic form (*c/a*=1) is predicted to be mechanically unstable (Fig 3.1) with respect to tetragonal distortions, raising fundamental questions about the true nature of the high temperature cubic phase. The tetragonal distortion of TiH_2 arises from a Jahn-Teller instability that splits a spike in the electronic density of states of cubic TiH_2 at the Fermi level ε_F. Thermal smearing of the electronic states around ε_F could conceivably undo the energy gain of the Jahn-Teller distortion and thereby stabilize the cubic phase above a critical temperature.[112] This was indeed shown to be the case, with thermal electronic excitations qualitatively modifying the shape of the free energy of TiH_2 versus *c/a*, rendering cubic TiH_2 mechanically stable above ~1000 K. This temperature, however, is

35

well above the experimental tetragonal to cubic transition temperature of 300 K, suggesting that electronic excitations alone may not be sufficient to explain the stability of cubic TiH_2. Other excitations involving vibrational degrees of freedom could play an important role, although a calculation of the free energy of TiH_2 as a function of c/a within the harmonic approximation did not alter the mechanical instability of cubic TiH_2 at finite temperature.[113]

In this chapter, we explore the role of anharmonic strain fluctuations at the level of the crystal unit cell in stabilizing the mechanically unstable cubic form of TiH_2 at high temperature.

3.2 Construction of Hamiltonian

We map the TiH_2 crystal onto a cubic lattice representing the corner points of the cubic fcc unit cell of the Ti sublattice. For this cubic reference lattice, we introduce an effective Hamiltonian that accounts for strain anharmonicity and that predicts cubic TiH_2 to be mechanically unstable with respect to tetragonal distortions. We write the Hamiltonian as a sum of functions Φ_ζ associated with different clusters of sites, ζ, of the cubic lattice according to

$$E(...,\vec{u}_i,...) = E_0 + \sum_{\varsigma=pair} \Phi_\varsigma(\vec{u}_i,\vec{u}_j) + \sum_{\xi=triplet} \Phi_\xi(\vec{u}_i,\vec{u}_j,\vec{u}_k) + \sum_{\zeta=quadruplet} \Phi_\zeta(\vec{u}_i,\vec{u}_j,\vec{u}_k,\vec{u}_l) + ... \tag{3.1}$$

where the $\vec{u}_i$ are deviations from ideal positions in the reference cubic lattice of site i, E_o is the energy of the undeformed reference cubic lattice and the summations in principle extend over all possible clusters of sites. Instead of expressing the cluster functions Φ_ζ explicitly in terms of atomic deviations, $\vec{u}_i$, from the cubic reference lattice, it is more convenient to write them as a function of strain variables that serve as a measure of the deformation of the cluster ζ from its ideal shape in the reference cubic crystal. For a pair cluster (e.g., Fig. 3.2a), an appropriate metric for deformation is the stretch of the bond between two cubic lattice points. For a non-collinear three-point cluster or a non-planar four-point cluster, useful metrics of deformation can be extracted from two-dimensional or three-dimensional strain gradient tensors **F** which map the cluster in the cubic reference lattice onto the cluster of the deformed lattice. As a particular example, consider a four-point cluster of the cubic lattice consisting of a central site connected to three nearest neighbor sites along the three cubic directions (Fig. 3.2b). The symmetric Cauchy-

Green tensor, $\mathbf{C}=\mathbf{F}^{\mathrm{T}}\mathbf{F}$, removes any rigid rotation of the cluster around its central atom. Furthermore, its diagonal elements are a measure for the stretch, $S_\alpha = \sqrt{C_{\alpha\alpha}} - 1.0$, of the bonds along the three cubic directions α, while its off-diagonal elements measure shears as they are related to the angles $\theta_{\alpha\beta}$ between the cubic directions of the cluster according to $\cos\theta_{\alpha\beta} = C_{\alpha\beta} / \sqrt{C_{\alpha\alpha} C_{\beta\beta}}$.

(a)   (b)
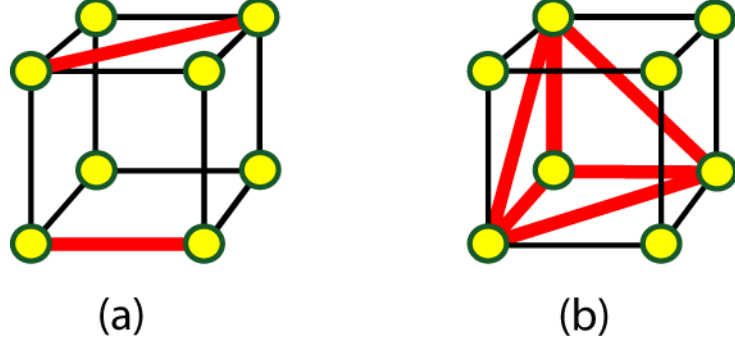
FIG 3.2: (a) first and second nearest neighbor clusters of the cubic lattice and (b) four point cluster of the cubic lattice used in the lattice Hamiltonian (see text).

In its general form, the anharmonic lattice Hamiltonian, Eq. (3.1), offers enough degrees of freedom to accurately reproduce the (free) energy surface for both homogeneous and localized deformations of the cubic lattice. From a practical point of view, however, the Hamiltonian must be truncated for some maximally sized cluster. For TiH$_2$, inclusion of four-point clusters is essential to capture the predicted instability of the cubic phase with respect to a tetragonal distortion. The Hamiltonian, used in the present study, therefore, contains in addition to cluster functions Φ_ζ corresponding to pair clusters up to the second nearest neighbor shell, also a cluster function for the four-point cluster depicted in Fig 3.2b. We express the cluster functions Φ_ζ as polynomials of the metrics of strain for the cluster ζ. For the pair clusters Φ_ζ can be expressed as a polynomial of the stretch of the pair, and if only harmonic contributions are taken into account, we can write $\Phi_\zeta = K_{ij} |\vec{u}_i - \vec{u}_j|^2$, where K_{ij} is related to a spring constant.

The polynomial expression for the cluster function, Φ_ζ, of the four-point cluster must contain higher order terms to capture the anharmonicity of the energy as a function of the *c/a* ratio.

Furthermore, the polynomial corresponding to the four body clusters must satisfy the symmetry associated with the cubic to tetragonal transformation so that it predicts the same (free) energy variation when the cubic lattice is compressed along the x, y or z-axis. It is therefore more convenient to represent the strain of the four-point cluster in terms of linear combinations of the stretches, S_α, and shears, $\cos\theta_{\alpha\beta}$, according to[114, 115]

$$e_1 = (S_1 + S_2 + S_3)/\sqrt{3}, \quad e_2 = (S_1 - S_2)/\sqrt{2}, \quad e_3 = (S_1 + S_2 - 2S_3)/\sqrt{6}$$

$$e_4 = \cos\theta_{12}, \quad e_5 = \cos\theta_{23}, \quad e_6 = \cos\theta_{13}$$

Here, e_1 measures dilation of the cluster, while e_2 and e_3 describe the deviatoric distortion of the cluster. The remaining three terms, e_4, e_5 and e_6, measure the shear strains between the three cubic directions. The most important strain variables in the context of the cubic to tetragonal phase transformation are e_2 and e_3 as they measure the degree of tetragonality, and enable a representation of all symmetrically equivalent tetragonal variants in a two dimensional plot. The cluster function for the four-point cluster, Φ_ζ, can be expressed as a polynomial of the e_i according to[114]

$$\Phi_\zeta = A\left(e_2^2 + e_3^2\right) + Be_3\left(e_3^2 - 3e_2^2\right) + C\left(e_2^2 + e_3^2\right)^2 + Q\left(e_4^2 + e_5^2 + e_6^2\right) \tag{3.2}$$

which satisfies the symmetry relations between the three equivalent tetragonal variants that can form from the cubic lattice. Symmetry constraints require coefficients of any odd power of e_2, e_4, e_5 and e_6 to be zero and only allow selected odd powers of e_3 when multiplied with even powers of e_2. The polynomial must satisfy 3-fold symmetry with respect to e_2 and e_3 as well as mirror symmetry around the e_3 axis and the two axes obtained by rotating the e_3 axis by 120° and -120° to ensure that the same energy is predicted for the symmetrically equivalent tetragonal distortions along the x, y and z directions. In Eq. (3.2), we neglect an explicit dependence on dilation (which is accounted for to some degree by the pair cluster functions) as well as anharmonic contributions from shear strains, e_4, e_5 and e_6. The A, B, C and Q parameters are independent of deformations of the four-point clusters, but could depend on temperature if electronic excitations and harmonic vibrational degrees of freedom of the basis atoms within the cubic unit cell are accounted for. We note that the above expression was originally introduced to

describe the free energy for a cubic to tetragonal transformation at the continuum level.[114, 115] Here we apply the expression to describe a contribution to the energy of deformation of a cluster of four sites in a discrete cubic lattice.

3.3 Results

With pair-cluster functions up to the second nearest neighbor and the cluster function of Eq. (3.2) for the four-point cluster, we have an effective Hamiltonian that can describe the energy of the cubic crystal and its stable tetragonal variants as a function of arbitrary local strain that does not disrupt the connectivity of the cubic lattice. With these terms, the Hamiltonian can be written as

$$E = E_o + \sum_{i,j\in\alpha} K_{ij}\left(\vec{u}_i - \vec{u}_j\right)^2 + \sum_\gamma A\left(e_{2\gamma}^2 + e_{3\gamma}^2\right) + Be_{3\gamma}\left(e_{3\gamma}^2 - 3e_{2\gamma}^2\right) + C\left(e_{2\gamma}^2 + e_{3\gamma}^2\right)^2 + Q\left(e_{4\gamma}^2 + e_{5\gamma}^2 + e_{6\gamma}^2\right) \tag{3.3}$$

The summation over i and j is over all nearest and second nearest neighbor pairs while the summation over γ is over all four point clusters symmetrically equivalent to that of Fig. 3.2(b). The $e_{l\gamma}$ is the lth strain metric (as used in Eq. (3.2)) for the four-body cluster γ.

To accurately represent the anharmonic degrees of freedom in TiH_2, we fit the coefficients K_{ij}, A, B, C and Q of Eq. (3.3) to the first-principles energy landscape for homogeneous and localized deformations of the cubic lattice of TiH_2. The energies of 202 homogeneous and local deformations of the TiH_2 lattice were calculated from the first principles. The first-principles calculations were performed with DFT within GGA as implemented in the VASP code. The core-electron interactions were treated with the projector augmented wave (PAW) method.[85, 88] A plane wave basis set cutoff energy of 400 eV was used and an $8 \times 8 \times 8$ k-point grid was chosen for the cubic unit cell (which contains four units of TiH_2). All homogeneous strains are relative to a cubic reference lattice with a lattice parameter of 4.4316 Å. Volumetric strains were uniformly sampled between -4% and +4% of the reference volume and tetragonal distortions of the cubic cell were sampled by varying the c/a ratio between 0.85 and 1.15. Energies for shear deformations were calculated in three states of tetragonal distortion (c/a = 0.92, c/a = 1.0 and c/a = 1.07) with shear strains taken as large as 7%. We also calculated the energy of local deformations of the lattice using a supercell containing $2 \times 2 \times 2$ cubic unit cells (consisting of

32 TiH_2 units). The lattice site at the center of the supercell (corresponding to a Ti atom) was systematically perturbed and only its first nearest neighbor Ti and hydrogen atoms were allowed to relax completely (these nearest neighbor atoms are basis atoms within the cubic unit cell of TiH_2). For the cubic phase and the stable tetragonal phase (c/a ratio = 0.92), we incrementally perturbed the central Ti atom of the $2 \times 2 \times 2$ supercell in the x, z and body diagonal directions with a maximum excursion of $1/10^{th}$ of the original length of the cubic lattice vector.

A fit to the energies of these deformations yielded the following values for the coefficients of the anharmonic strain Hamiltonian, Eq. (3.3): $K_{ij} = 2.586$ eV/$Å^2$ for the first nearest neighbor spring constant (of the cubic lattice), $K_{ij} = 0.776$ eV/$Å^2$ for the second nearest neighbors spring constant, $A = -9.406$ eV, $B = -0.682$ eV, $C = 140.895$ eV and $Q = 0.009$ eV. In fitting these coefficients, more weight was assigned to the low-energy deformations (relative to the tetragonal ground state) than to the high-energy deformations. High-energy deformations were included in the fit to ensure that the anharmonic strain Hamiltonian does not predict spurious local minima at large deformations. While overall the root mean square (RMS) error between the first-principles energies and those predicted by the Hamiltonian is 203 meV per unit cell, the quality of the fit is significantly better for the low energy excitations. The rms error between first principles energies and those predicted by the Hamiltonian is 3 meV per unit cell for homogeneous deviatoric and shear strains and local deformations of the tetragonal ground state (c/a = 0.92) that lead to an energy increase of less than 50 meV per unit cell above the ground state energy.
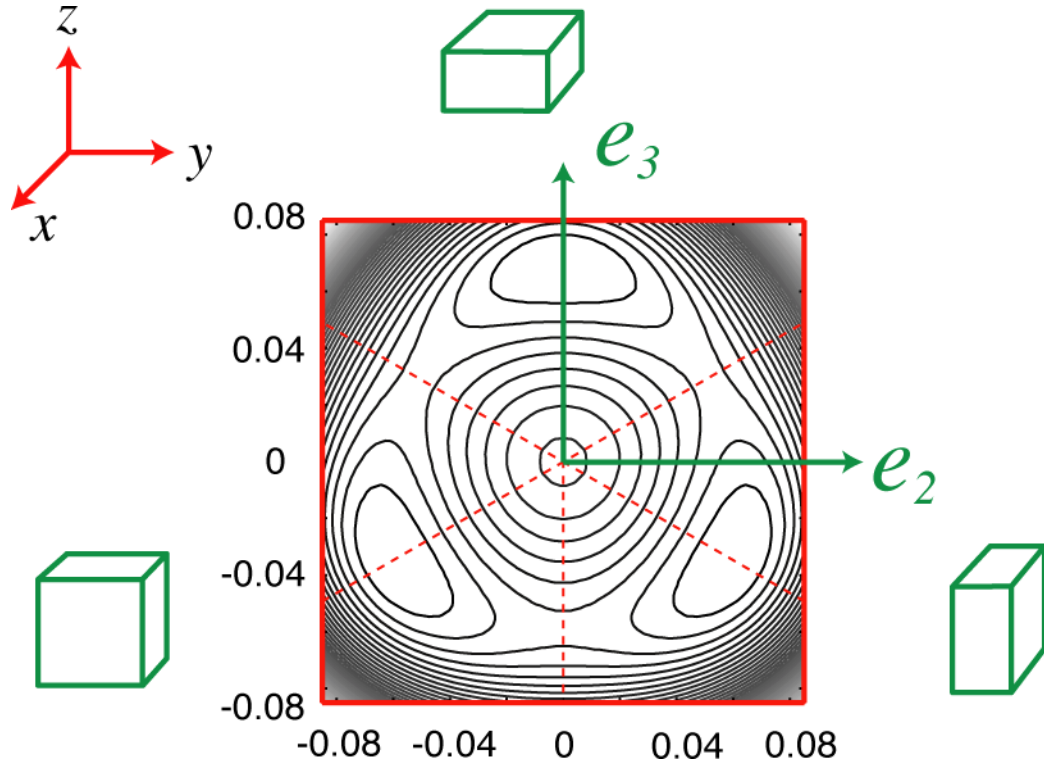
FIG 3.3: Energy contour plot as a function of the deviatoric strain metrics e_2 and e_3 as predicted by the effective strain Hamiltonian (see text). The cubic phase, corresponding to the origin in e_2 and e_3 space, is predicted to be a local maximum, while the three wells correspond to the symmetrically equivalent stable tetragonal distortions of the cubic lattice.

The resulting effective Hamiltonian reproduces an energy minimum for the symmetrically equivalent tetragonal variants along the x, y and z directions and an energy maximum for the cubic lattice. Fig. 3.3 illustrates an energy contour plot predicted by the first-principles parameterized Hamiltonian as a function of e_2 and e_3 for homogeneous deviatoric deformations of the cubic lattice, while all other homogenous strain metrics are set to zero. The cubic lattice corresponds to the origin of the e_2 and e_3 plot and is a local energy maximum. Tetragonal distortions of the cubic lattice along the z-axis are along the e_3 axis with $e_2 = 0$. The Hamiltonian predicts a mininum for positive e_3 at approximately 0.066, which corresponds to a tetragonal distortion along z with a c/a ratio of approximately 0.92. Tetragonal distortions along the x and y axis occur along the dashed lines in Fig. 3.3 rotated from the vertical axis by 120° and -120° respectively.

We subjected the effective Hamiltonian to Monte Carlo simulations to explore the role of anharmonic vibrational degrees of freedom in stabilizing the mechanically unstable cubic phase at elevated temperature. A standard Metropolis Monte Carlo algorithm was used with periodic boundary conditions (the Monte Carlo cell sizes contained 16^3, 24^3 and 32^3 cubic unit cells). We choose a lattice site of the cell at random and perturb it with random distance and direction (bounded by a maximum excursion). The Hamiltonian is used to calculate the energy changes ΔE due to the random perturbations and the perturbation is accepted if ΔE is negative or $\exp(-\Delta E/k_B T)$ is greater than a random number between 0 and 1 (k_B is the Boltzman constant and T is the absolute temperature). During a Monte Carlo pass, each lattice site is visited on average once and distortions of the Monte Carlo supercell are also sampled by random perturbations of the lattice vectors. We performed 6000 Monte Carlo passes at each temperature during which averages of local and macroscopic strain variables were taken.
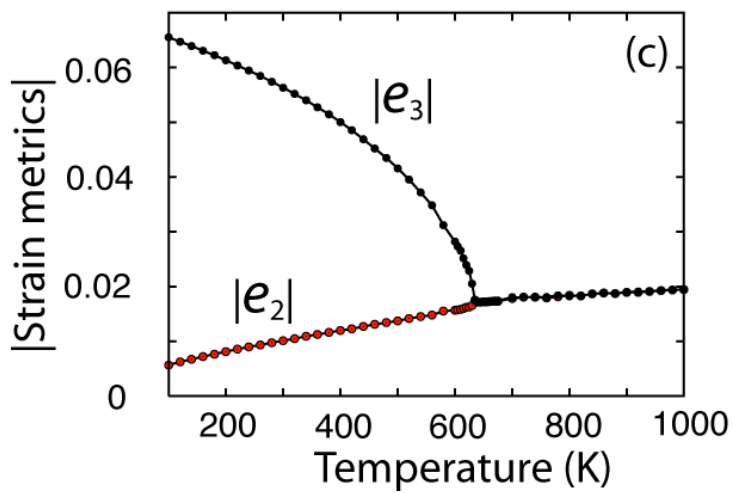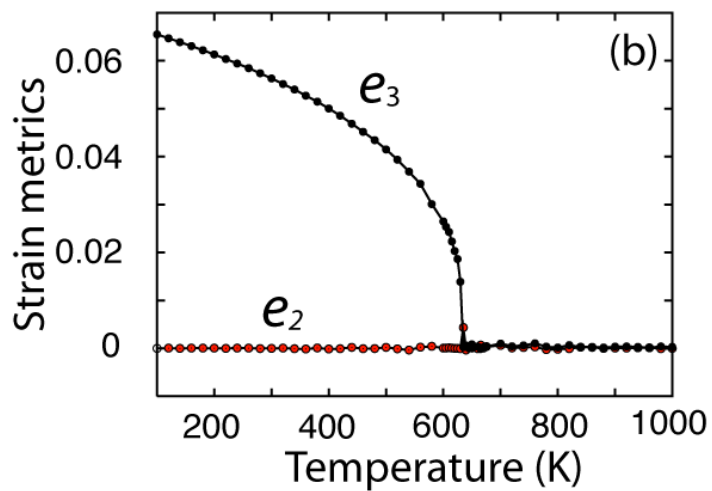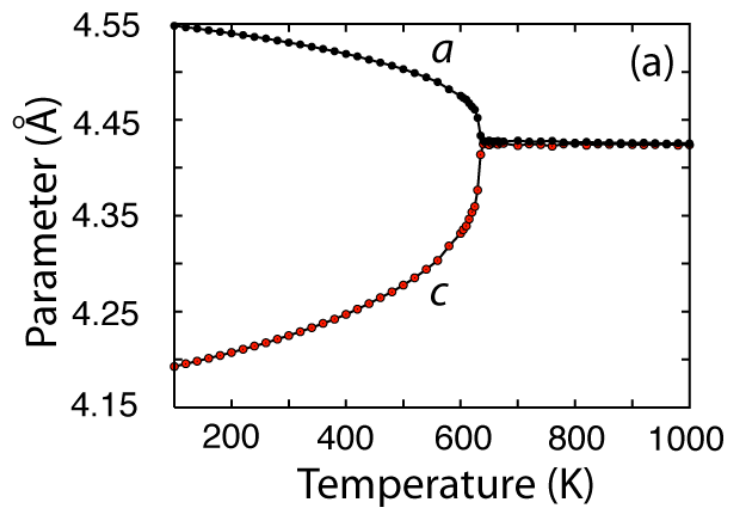
FIG 3.4: (a) Variation of the lattice parameters a and c as a function of temperature calculated with Monte Carlo simulations applied to the effective strain Hamiltonian that predicts the cubic phase to be mechanically unstable; (b) Average values of e_2 and e_3 as a function of temperature (the low temperature tetragonal phase is oriented along the z-axis) and (c) Average values of the absolute values of e_2 and e_3 as a function of temperature.

Figure 3.4(a) illustrates the variation with the temperature of the c and a lattice parameters (c is taken as the smallest of the three lattice parameters and a is taken as the average of the two larger lattice parameters) as calculated during the Monte Carlo simulations. As is clear from Fig. 3.4(a), the system has tetragonal symmetry at low temperature (characterized by a difference in c and a lattice parameters), but transforms to cubic symmetry at high temperature. The c and a lattice parameters converge to each other rapidly as the temperature approaches 635K, undergoing a transition to the cubic lattice where all lattice parameters are equal. The same behavior is predicted during heating and cooling Monte Carlo simulations, with no detectable hysteresis in the transition temperature. These Monte Carlo results clearly show that although the effective Hamiltonian predicts the cubic phase to be mechanically unstable with respect to tetragonal distortions, finite temperature excitations nevertheless lead to a stabilization of a cubic phase at elevated temperature.

Further insight about the true nature of the high temperature cubic phase can be obtained by inspection of the averages of the deviatoric strain metrics, e_2 and e_3. Figure 3.4(b) illustrates the temperature dependence of e_2 and e_3 averaged over all lattice points of the crystal. At low temperature, the system adopts a tetragonal symmetry with the compressed lattice vector along the z axis ($e_2 = 0$ and e_3 is positive). As the temperature increases, the average of e_3 decreases, rapidly converging to zero as the temperature approaches 635K. Above 635K, both e_2 and e_3 are on average equal to zero signifying that at high temperature the system adopts a cubic symmetry on average. Inspection of the averages of the *absolute values* of e_2 and e_3, however, shows that e_2 and e_3 fluctuate significantly within the high temperature cubic phase, sampling both positive and negative values with equal frequency (Fig. 3.4(c)). Furthermore, the averages of the absolute values of e_2 and e_3 are equal above the transition temperature, indicating that there is no preference for any of the three low energy tetragonal variants within the cubic phase. This

indicates that the high temperature cubic phase is in fact characterized by the large temporal fluctuations of spatially localized deviatoric deformations. Within the tetragonal phase below 635K, sizable fluctuations of e_2 are also present (as manifested by a non-zero average value of the absolute value of e_2) and these grow with increasing temperature. At the tetragonal to cubic transition temperature, the absolute values of e_2 and e_3 become equal, indicating that the system samples e_2 and e_3 with circular symmetry.

The finite temperature behavior of this system can be rationalized by inspection of the energy contours of Fig. 3.3, plotted in terms of homogenous deviatoric strains, e_2 and e_3 of the cubic reference lattice. We emphasize that the energy surface of Fig. 3.3 is for homogeneous strains of the lattice, while the true energy surface sampled in the Monte Carlo simulations is more complex and depends on a large number of local deformation variables as well. Local deformations, including local shears, introduce additional energy penalties that are not represented in Fig. 3.3, but are correctly accounted for in the Monte Carlo simulations. At a low temperature, the crystal resides in one of the potential energy wells of Fig. 3 corresponding to one of the three stable tetragonal variants. The values of e_2 and e_3 fluctuate around their values at the local minimum. As the temperature is raised, increased thermal energy allows the system to sample higher energy states, leading to larger excursions of e_2 and e_3 from their values at the local minimum. As the tetragonal to cubic transition temperature is approached, sufficient thermal energy becomes available for the system to overcome the barriers separating the energy wells of the three tetragonal variants, at which point the system loses its tetragonal symmetry and on average adopts cubic symmetry. With sufficient thermal energy, the local minima are no longer deep enough to confine the lattice deformations to regions of phase space characterized by a tetragonal distortion and the system samples states within a potential well that has cubic symmetry, bounded by a rapid increase in potential energy with almost circular symmetry in e_2 and e_3 space. Relative sampling frequency in the e_2-e_3 space can shed more light on the nature of this phase transition. We discuss the variation of relative sampling frequencies at different temperatures in appendix A. The Monte Carlo simulations indicate shorter correlation lengths between the deviatoric metrics of strain between neighboring lattice sites within the cubic phase as compared to the tetragonal phase.

The predicted transition temperature of 635K is higher than the experimental transition temperature of 300K. However, we found that the transition temperature is sensitive to the difference in energy between the tetragonal and cubic phases as well as the *c/a* ratio of the stable tetragonal distortion. A change in the minimum-energy-*c/a* ratio from 0.92 to 0.94 (which is the experimentally found value of *c/a* ratio for the tetragonal phase[111]) reduces the transition temperature to 350 K (which is very close to the experimental value of 300 K[111]). Furthermore, the strain Hamiltonian is fit to the zero Kelvin energy surface. At finite temperature, electronic excitations and harmonic vibrational excitations of the basis atoms within the cubic cell lead to a reduction in the free energy difference between the cubic phase and the tetragonal phase.[113] Inclusion of this temperature dependence in the effective Hamiltonian is also likely to reduce the predicted transition temperature. The systematic construction of effective lattice Hamiltonians that incorporate the integrated-out degrees of freedom that do not explicitly participate in a structural phase transformation has been described by Rabe and Wagmare.[116]

3.4 Conclusion

We have shown that anharmonic vibrational degrees of freedom can play a crucial role in stabilizing the high temperature phases that are predicted to be mechanically unstable at zero Kelvin and that undergo a structural phase transformation involving large homogeneous strains upon cooling. This finding indicates that the thermodynamic properties of many high temperature phases are likely to be more complex than is commonly assumed in analyses of phase stability that rely on the (quasi) harmonic approximation.

Chapter 4

Phase stability and non-dilute Li diffusion in spinel lithium titanate

4.1 Introduction

Charge and discharge rates of Li-ion batteries depend sensitively on Li ion mobility within the electrode materials. Most electrode materials of reversible Li-ion batteries are intercalation compounds that accommodate Li ions in the interstitial sites of a crystalline host.[43] Lithium ions diffuse in and out of the intercalation compound by exchanging with vacancies. Often the Li concentration within the host can be varied from very dilute concentrations to the fully concentrated limit. Hence, Li diffusion predominantly occurs at non-dilute concentrations where interactions among Li ions play an important role in influencing mobility.

Lithium intercalation compounds exhibit a wide variety of crystal structures and chemistries.[43, 60, 61, 117] Transition metal oxides such as Li_xCoO_2, $Li_x(Ni_{1/2}Mn_{1/2})O_2$ and $Li_x(Co_{1/3}Ni_{1/3}Mn_{1/3})O_2$ have a layered crystal structure that accommodate Li ions between transition metal oxide slabs, thereby restricting Li diffusion to two-dimensional layers. Crystallographic features of the lithium sites in layered Li_xCoO_2 and Li_xTiS_2, for example, result in a diffusion mechanism predominantly mediated by di-vacancies,[56, 70, 118] which becomes inefficient at high Li concentrations where the number of vacancies becomes small. Diffusion in the layered intercalation compounds is also affected by the dimensional variations of the host crystal structure. The contraction of the c-lattice parameter (perpendicular to the Li-layers) with decreasing Li concentration in

Li_xCoO_2 and Li_xTiS_2 results in an increase of migration barriers, causing the diffusion coefficient to decrease at low Li concentration.[56, 70] Intercalation compounds such as Li_xFePO_4 have an olivine crystal structure[46] in which Li diffusion is restricted to one-dimensional channels.[69] One-dimensional diffusion has important consequences for the rate capabilities of the olivine compounds as well as the kinetic mechanisms of the two-phase reaction from $LiFePO_4$ to $FePO_4$.[119-122] The crystal structures of other intercalation compounds such as spinel-$Li_xMn_2O_4$[123] or anatase-TiO_2[124, 125] consist of three-dimensional interstitial networks, and it is generally believed that the higher dimensional networks lead to enhanced Li mobility.

While several in-depth studies have been performed on Li diffusion in layered intercalation compounds,[56, 70] much remains to be understood about the dependence of diffusion mechanisms on crystal structure and composition in non-layered intercalation compounds. In this chapter, we perform a first-principles investigation of lithium diffusion in the spinel crystal structure as a function of lithium concentration, focusing on $Li_{1+x}Ti_2O_4$.[62, 126, 127] The spinel form of $Li_{1+x}Ti_2O_4$ is crystallographically identical to spinel $Li_xMn_2O_4$.[123, 128] Though the manganese spinel variant is currently used as a cathode in Li-ion batteries for automotive applications, its electronic structure is significantly more complex than that of spinel $Li_{1+x}Ti_2O_4$, exhibiting localized charge ordering,[129] local and cooperative Jahn-Teller distortions,[130] and complex magnetic ordering,[131-133] all varying with Li concentration. The arrangements of Mn^{3+} and Mn^{4+} ions in spinel $Li_xMn_2O_4$, for example, are likely correlated to the arrangements of Li ions and could result in a coupling between Li hops and rearrangements of charge ordering over the Mn-sublattice. This electronic complexity is for a large part absent in $Li_{1+x}Ti_2O_4$, thereby simplifying the study of both its thermodynamic[134] and kinetic properties and allowing us to isolate the role of the spinel crystal structure on lithium diffusion at non-dilute concentrations.

Unlike most lithium transition metal oxides that serve as cathodes in Li-ion batteries, the $Li_{1+x}Ti_2O_4$ spinel electrode exhibits a low voltage, making it a viable anode in lithium batteries. Especially the Li-excess variant, $Li_{1+x}(Li_{1/6}Ti_{5/6})O_2$, has proven very attractive

as a high rate anode material[126, 127, 135-138] in part since its cubic lattice parameter varies negligibly with Li concentration, thereby making it less susceptible to mechanical fatigue that results from the repeated Li removal and insertion. The spinel titanate also operates above the voltage of solid-electrolyte interface (SEI) formation, which is in part responsible for the limited cycle life times of graphitic anodes.[139, 140]

We start our study with an investigation of the thermodynamics of Li intercalation in $Li_{1+x}Ti_2O_4$ spinel from first principles, using a cluster expansion in combination with Monte Carlo simulations. Next we analyze elementary Li hop mechanisms at a variety of Li compositions and in various states of Li-vacancy order/disorder. These results are then used in kinetic Monte Carlo simulations where Li diffusion coefficients are calculated as a function of Li concentration. A cluster expansion is implemented in the kinetic Monte Carlo simulations to rigorously account for variations in the migration barriers with Li composition and local Li-vacancy (dis)order. We conclude with a discussion of the unique features of the spinel crystal structure with respect to Li diffusion and how they lead to the enhanced mobility compared to the layered intercalation compounds.

4.2 Results

The spinel form of $Li_{1+x}Ti_2O_4$, which belongs to the $Fd\bar{3}m$ space group, consists of an oxygen fcc sublattice ($32e$ sites) with the titanium atoms filling half of the available octahedral interstitial sites of the oxygen sublattice ($16d$ sites). The other half of the octahedral sites, designated $16c$, and one eighth of the available tetrahedral sites, designated $8a$, can be occupied by Li.[60] The remaining interstitial sites share faces with oxygen octahedra surrounding titanium and are, therefore, energetically too costly for lithium occupancy. The crystal structure of spinel and the interstitial Li sites are shown in figure 4.1.
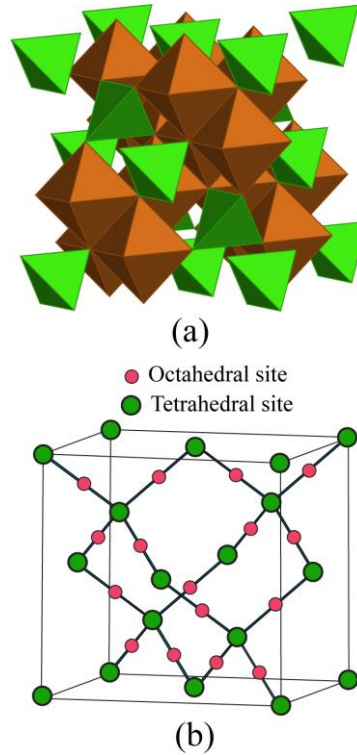
FIG 4.1: (a) Crystal structure of $Li_{1+x}Ti_2O_4$ spinel. Li ions can occupy the $8a$ sites (center of the green LiO_4 tetrahedrons). Ti ions are located at the $16d$ sites (center of the brown TiO_6 octahedrons) (b) The Li sublattice in spinel host consists of a diamond network of $8a$ tetrahedral sites (green circles) with the octahedral $16c$ sites (pink circles) halfway in-between two nearest neighbor tetrahedral sites.

The tetrahedral $8a$ sites form a diamond sublattice. The octahedral $16c$ sites reside half-way between neighboring tetrahedral sites. Each tetrahedral site, therefore, has four octahedral nearest neighbor sites, while each octahedral site has two nearest neighbor tetrahedral sites. There are twice as many octahedral $16c$ sites as tetrahedral 8a sites.

4.2.1 Formation energies and cluster expansion

To construct a cluster expansion for the configurational energy, we calculated the formation energies of 123 symmetrically non-equivalent lithium-vacancy configurations over the interstitial sites of the $Li_{1+x}Ti_2O_4$ spinel using DFT (VASP within GGA). Configurations were generated in periodic supercells having varying sizes. Fourteen

configurations had the primitive unit cell consisting of 4 Ti and 8 O atoms; 64 configurations had a supercell consisting of two primitive cells; 40 configurations had a cubic supercell consisting of 4 primitive cells and 5 configurations had a supercell consisting of 8 primitive cells (2×2×2). The coordinates of all atoms were fully relaxed. An energy cutoff of 400 eV was used and an 8×8×8 k-point was used in the reciprocal lattice of the primitive cell. For the cubic supercell and the supercell with 8 primtive cells, we used a 4×4×4 k-point grid. Of the 123 configurations investigated, fifteen relaxed to other configurations, reducing the number of fully-relaxed, symmetrically-distinct configurations to 108. The formation energies of these configurations were calculated with respect to the energies of delithiated spinel Ti_2O_4 (keeping the spinel symmetry) and fully lithiated $Li_2Ti_2O_4$ (with Li filling all octahedral 16c sites) according to:

$$E_{formation} = E - \frac{1}{2}(1+x)E_{Li_2Ti_2O_4} - \frac{1}{2}(1-x)E_{Ti_2O_4} \qquad (4.1)$$

and are illustrated in figure 4.2 (the formation energies are per primitive cell, which contains 4 Ti and 8 O).
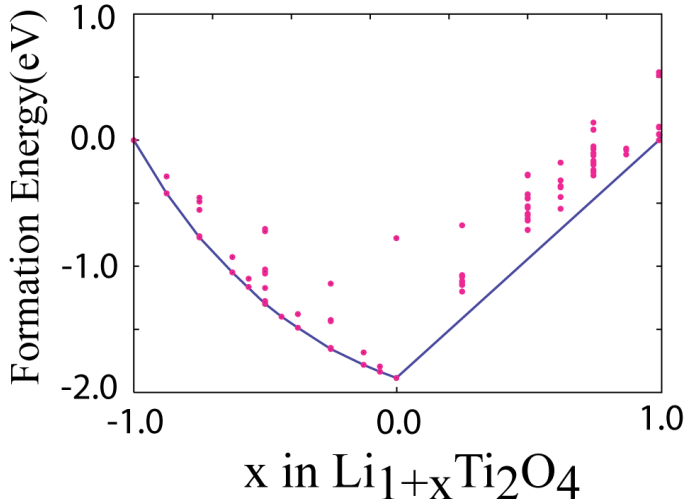
FIG 4.2: Formation energies of different configurations calculated from first-principles and the associated convex hull. The hull points are connected by the blue hull-line. Formation energies are per primitive cell consisting of 4 Ti and 8 Oxygen atoms.

The blue line in Fig. 4.2 represents the convex hull of the formation energies. The convex hull is equivalent to the well-known common tangent construction applied to free energies to determine phase stability as a function of composition. The formation energies residing on the convex hull in Fig. 4.2 are equal to the free energies of the stable ordered phases of $Li_{1+x}Ti_2O_4$ at zero Kelvin, where the entropy is equal to zero. The equilibrium state of $Li_{1+x}Ti_2O_4$ when x has a value between pairs of the stable ordered phases consists of a two-phase mixture of the two stable phases. The energy of the two-phase mixture resides on the common tangent at the composition x.

The DFT formation energies of Fig. 4.2 provide important insights about the behavior of Li insertion into spinel $Li_{1+x}Ti_2O_4$. In the concentration range $-1.0 < x < 0.0$, all low energy configurations consist of tetrahedral Li, in agreement with a previous first-principles study of this system.[134] Octahedral occupancy in the same composition range is mechanically unstable (see section 4.1.3). Initial configurations with octahedral lithium either relax to a configuration with only tetrahedral occupancy or, if the symmetry of the configuration prevents Li relaxation out of an octahedral site, relax to a high-energy configuration corresponding to a saddle point in the energy landscape. At $x = 1$, in contrast, the ground state structure consists of only octahedral Li ions. A miscibility gap (i.e. two-phase coexistence) exists in the range $0.0 < x < 1.0$ as can be seen by the absence of any ground states in that concentration range and as was predicted previously.[134]

The uniform and dense distribution of ground states for $-1.0 < x < 0.0$ suggests that a solid-solution like behavior, where no particular ordering of lithium and vacancies is preferred, should dominate at moderate temperatures. This behavior changes once all tetrahedral sites of the host are occupied at $x = 0$. For $x > 0$, the configurations either consist of mixed tetrahedral and octahedral occupancy by Li or exclusively octahedral occupancy by Li. Although the energy of the crystal is minimized when Li occupies tetrahedral sites, the addition of Li to $LiTi_2O_4$, in which all the tetrahedral sites are filled, must occur by filling octahedral sites. This can occur in two ways: (i) if existing tetrahedral Li are not displaced, the additional Li must fill octahedral sites that are nearest

neighbors to the filled tetrahedral sites, thereby incurring a large energy penalty; (ii) Li addition to octahedral sites can also be accompanied by the displacement of tetrahedral Li to energetically less favorable but more abundant octahedral sites. In either case, the energy of the configuration with intermediate Li composition is higher than that of a two-phase mixture of $LiTi_2O_4$ and $Li_2Ti_2O_4$.

Experimentally, it is not possible to remove all the Li ions from spinel $Li_{1+x}Ti_2O_4$. Voltage curves have only been measured up to a composition of $x = - 0.2$,[127] while studies using chemical delithiation indicate that Ti atoms begin to rearrange over the interstitial sites of the oxygen sublattice to adopt more stable arrangements as more and more Li are removed from spinel $LiTi_2O_4$.[141] The energy of delithiated spinel Ti_2O_4, for example, is higher than that of anatase TiO_2 by 557 meV per TiO_2 formula unit (both have the same fcc oxygen sublattice but a different Ti ordering over the octahedral sites). This shows that delithiated spinel has a significantly higher energy than other polymorphs of TiO_2 thereby making it susceptible to transformation. Even when the Ti atoms are constrained to remain in the $16d$ sites of the spinel crystal structure, we found that the removal of symmetry constraints during total energy minimization of delithiated spinel Ti_2O_4 results in severe structural relaxations of the oxygen and titanium ions to the degree that it no longer resembles a spinel host structure.

Of the 108 symmetrically distinct configurations illustrated in Fig. 4.2, 70 were used to fit the ECI's of a cluster expansion for the configurational energy of Li-vacancy order/disorder over the tetrahedral and octahedral sites of $Li_{1+x}Ti_2O_4$. Two configurations in the dilute lithium regime were left out of the fit as they relaxed to structures that no longer resemble spinel while an additional thirty six high-energy configurations were left out to facilitate a more rapid convergence of the truncated cluster expansion.[142] For statistical mechanical averaging, a key requirement of the cluster expansion is that it accurately predicts low energy configurations. We also fit to differences in energies between configurations in which a Li is initially in a tetrahedral site and then in an adjacent octahedral site. Since the octahedral sites are mechanically unstable when $x < 0$, we used the nudged elastic band method to calculate the GGA saddle point energies of

the octahedral sites. Fitting to differences in energy between octahedral and tetrahedral Li occupancy was done to ensure an accurate prediction of migration barriers, since as will be described in section 4.2.3, the octahedral sites correspond to activated states when $x <$ 0. Nine such differences in energy were used in the cluster expansion fit. The resulting cluster expansion consists of an empty cluster V_0, two point clusters (one for tetrahedral and the other for octahedral site), nine pair clusters, seven triplets and five quadruplets. The overall rms error was 9 meV and CV score was 18 meV per TiO_2 formula unit.

4.2.2 Thermodynamics

Grand canonical Monte Carlo simulations were applied to the cluster expansion to calculate thermodynamic averages. We used 6000 Monte Carlo passes of which the first 2000 passes were for equilibration and the last 4000 were used for averaging. Each Li site is visited on average once during a Monte Carlo pass. Output from grand canonical Monte Carlo simulations includes the equilibrium Li composition and average grand canonical energy as a function of chemical potential and temperature. This relationship is of importance as the open circuit voltage of an intercalation compound electrode with respect to a metallic Li reference anode is related to the chemical potentials of the electrodes according to

$$V(x) = -\frac{\mu_{Li} - \mu_{Li}^{reference}}{Fz} \tag{4.2}$$

where z is the electron charge carried by one Li ion, F is Faraday's constant and μ_{Li} is the Li chemical potential of the intercalation compound. $\mu_{Li}^{reference}$ is the Li chemical potential of a pure Li reference electrode.

Figure 4.3 shows the calculated voltage curve for $Li_{1+x}Ti_2O_4$ as a function of x obtained by inserting the calculated chemical potential into Eq. (4.2) and using the energy of bcc Li for the chemical potential of the reference anode.
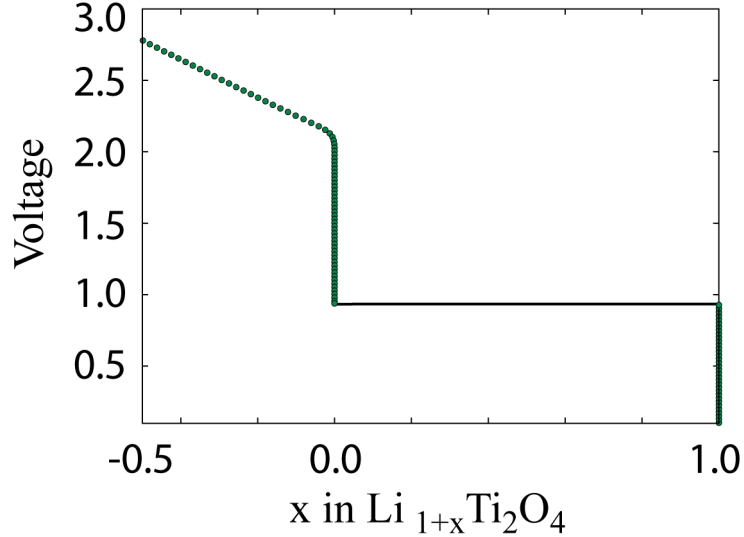
FIG 4.3: Equilibrium voltage curve as a function of lithium concentration (at room temperature), calculated with grand canonical Monte Carlo simulations. The plateau between $x = 0.0$ and $x = 1.0$ indicates two-phase coexistence.

The plateau in the voltage curve signifies a two-phase coexistence between $LiTi_2O_4$ and $Li_2Ti_2O_4$. We will refer to $Li_{1+x}Ti_2O_4$ with $x < 0$ as the α phase and $Li_{1+x}Ti_2O_4$ with $x \sim 1$ as the β phase. The smooth decrease in voltage with increasing Li content in the α phase indicates solid solution behavior as expected from the first-principles formation energies. The plateau voltage is approximately 0.94 volt while the experimental voltage curve[127] exhibits a plateau at 1.34 volt. The discrepancy can be attributed to the underestimation by LDA and GGA of voltages in transition metal oxide intercalation compounds due to self-interaction in the d orbitals of the transition metals.[143] The step in the voltage at $x = 0$ is approximately 1.2 volt. Colbow *et al.*[127] measured the voltage curve of $Li_{1+x}Ti_2O_4$ down to a Li concentration of $x = - 0.2$. Their measured voltage curves indicate that the voltage increases by approximately 1.4 volt when charging $Li_{1+x}Ti_2O_4$ from the plateau voltage to $x = - 0.2$. The corresponding difference in the calculated voltage curve is 1.2 volts. Apart from a systematic under-prediction of the equilibrium voltage curve, both the qualitative shape and the relative variation in voltage are in very good agreement with experiment.

A phase diagram, mapping phase stability as a function of temperature and composition, can also be constructed based on the output from Monte Carlo simulations. Using the well-established free energy integration techniques[144] (i.e. $dG = \mu dN$ at constant T and $d(\beta\Phi) = \Omega d\beta$ at constant μ_{Li}, where G is the Gibbs free energy, $\Phi = G - \mu_{Li}N$, $\Omega = E - \mu_{Li}N$ and $\beta = 1/k_B T$), it is possible to calculate the Gibbs free energy as a function of composition at various temperatures. Regions of two-phase coexistence can then be determined with the common tangent construction applied to the Gibbs free energy (or equivalently by determining the crossing of Φ's for different phases as a function of μ_{Li}). Free energy integration, however, requires a value for the free energy in a particular reference state. Convenient reference states correspond to those in which the configurational entropy is negligible, such as at dilute concentration and well-ordered phases at low temperature. The free energy of the phase is then very close to its energy and can be approximated with a low-temperature expansion technique.[145]
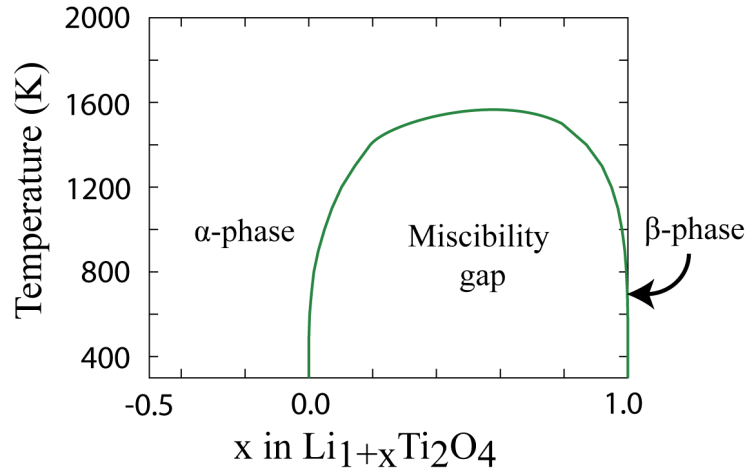
FIG 4.4: Calculated phase diagram as a function of temperature and lithium concentration. For low to moderate temperature, Li ions occupy tetrahedral sites for $x <$ 0.0 (α-phase). Li-ions occupy octahedral sites at $x = 1.0$ (β-phase). There is a miscibility gap between the two phases for $0.0 < x < 1.0$. The miscibility gap disappears above 1500 K.

Figure 4.4 shows the calculated phase diagram for $Li_{1+x}Ti_2O_4$, which exhibits a miscibility gap between the α phase (with exclusively tetrahedral occupancy) and the β phase (with exclusively octahedral occupancy). The equilibrium concentrations of the coexisting phases at fixed temperature define the boundary of the miscibility gap. The steep nature of the two-phase boundary suggests that both the phases are very stable even at high temperatures until the system is completely disordered above 1500 K.
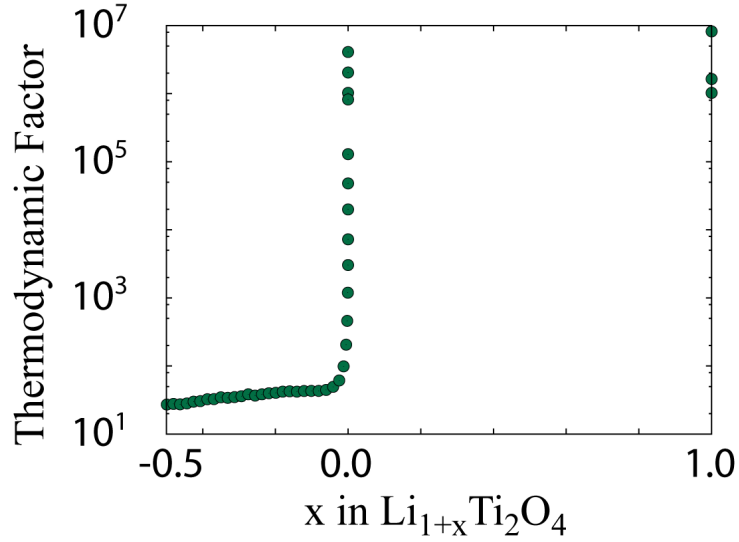
FIG 4.5: Variation of thermodynamic factor (Θ) as a function of lithium composition. Note that the thermodynamic factor diverges near the stoichiometric phases ($x = 0.0$ and $x = 1.0$)

The thermodynamic factor (Θ) is an important part of the chemical diffusion coefficient and can be calculated in grand canonical Monte Carlo simulations by keeping track of the fluctuations of the number of lithium atoms at constant μ_{Li} according to Eq. 2.27. Figure 4.5 shows the variation of the thermodynamic factor with Li concentration at room temperature. In the α phase, Θ ranges between 20 and 40 but diverges as x approaches 0 in $Li_{1+x}Ti_2O_4$ when all tetrahedral Li sites are filled. The thermodynamic factor also diverges in β-$Li_2Ti_2O_4$ in which all octahedral Li sites are occupied. Both $LiTi_2O_4$ and $Li_2Ti_2O_4$ correspond to the well-ordered phases and therefore deviate strongly from thermodynamic ideality. In stoichiometric phases, with a dilute concentration of

vacancies over the occupied sublattice, it can be shown that the thermodynamic factor scales with the inverse of the vacancy composition. The thermodynamic factor is not defined in the two-phase region ($0 < x < 1$).

4.2.3 Diffusion

4.2.3.1 Elementary hop mechanisms and barriers

The mechanisms of lithium diffusion are qualitatively very different in α and β phases due to the change in Li site occupancy from tetrahedral sites in α-$Li_{1+x}Ti_2O_4$ ($x < 0$) to octahedral sites in β-$Li_2Ti_2O_4$. Furthermore, as diffusion typically occurs in the non-dilute concentration regime, interactions between the nearby diffusing lithium ions also affect migration barriers for a particular atomic hop mechanism. We explored hop mechanisms and migration barriers from first-principles as a function of Li concentration using the nudged elastic band (NEB) method as implemented in VASP. NEB calculations were performed within a cubic supercell of $Li_{1+x}Ti_2O_4$ containing 32 oxygen, 16 titanium and variable number of lithium ions. Migration barriers were also calculated in larger supercells containing 64 oxygen, 32 titanium and variable Li ions.
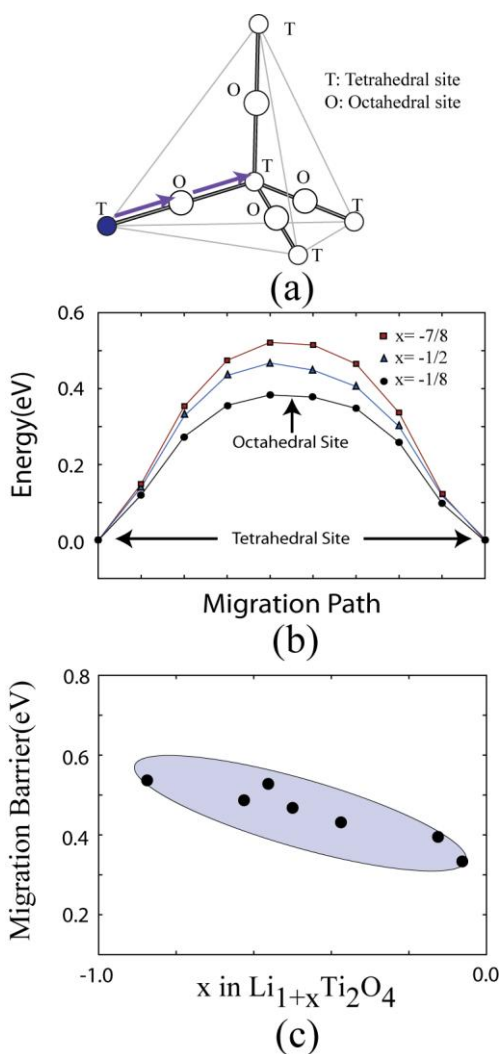
FIG 4.6: Migration barrier for different lithium concentrations in the α-phase ($x < 0$) (a) Lithium ion path during a hop (shown by the arrow) between two tetrahedral sites (marked as 'T') through the intermediate octahedral site (marked as 'O'). (b) Change in energy as a Li-ion hops in a particular configuration for three lithium compositions (Red squares: $x = -7/8$, blue triangles: $x = -1/2$ and black circles: $x = -1/8$). (c) Trend of migration barriers with lithium composition

Figure 4.6(a) shows the lithium ion migration path as it hops between the two nearest neighbor tetrahedral sites. Figure 4.6(b) shows the energy along the migration path between adjacent tetrahedral Li sites in representative Li-vacancy configurations at three different concentrations ($x = -7/8, -1/2, -1/8$) in the α-phase (i.e. Li occupies the

tetrahedral sites). A Li hop between the neighboring tetrahedral sites must pass through an octahedral site. The curve at $x = -1/2$, for example, is for a Li hop in one of many possible Li-vacancy configurations within the cubic unit cell used for these calculations. A striking feature of all three curves is that the octahedral site is never a local minimum but rather a saddle point (i.e. a maximum along the hop direction and a minimum perpendicular to the hop direction) for all compositions considered in the α phase ($-1 < x < 0$). This is contrary to the common belief that the octahedral sites of spinel intercalation compounds, such as $Li_{1+x}Mn_2O_4$ and $Li_{1+x}Ni_{0.5}Mn_{1.5}O_2$, while energetically less favorable than tetrahedral sites for $x < 0$ are nevertheless a local minimum. The results of Fig. 4.6(b) show that this is not the case for $Li_{1+x}Ti_2O_4$; rather the octahedral site is the activated state of the hop. This is in agreement with the recent NMR evidence on Li-excess spinel titanate.[146] Fig. 4.6(b) also shows a variation of the migration barrier with Li concentration, systematically decreasing as the Li concentration increases. This is also illustrated in Fig. 4.6(c), which shows the migration barriers at seven different concentrations in α-$Li_{1+x}Ti_2O_4$. At each concentration, there are many possible Li-vacancy configurations. In Fig. 4.6(b) we have only considered one configuration at each concentration, however, there will be some variability in migration barriers for different Li-vacancy configurations, even at the same Li concentration. Overall, Fig. 4.6(b) shows a clear trend of the decreasing migration barriers with the increasing Li concentration. We point out that at very dilute Li concentrations (i.e. $x = -15/16$), large relaxations within the 2×2×2 supercell resulted in a structure that no longer resembles the spinel host. The migration barrier calculated at this concentration is not included in Fig. 4.6(c).

Li diffusion in β-$Li_2Ti_2O_4$ is qualitatively different from that in α-$Li_{1+x}Ti_2O_4$ ($x < 0$) as Li occupies octahedral sites now. The grand canonical Monte Carlo simulations (Sec. 4.1.2) indicate that β-$Li_2Ti_2O_4$ is only stable in a very narrow concentration interval. Hence diffusion will be primarily mediated by a dilute concentration of vacancies. Occasionally though, several vacancies may encounter each other, thereby forming vacancy complexes that result in diffusion mechanisms differing from that of a single vacancy hop mechanism. With the nudged elastic band method, we investigated two types of hops: (i) the migration of an octahedral Li to a neighboring vacant octahedral site

(Fig. 4.7(a)) and (ii) the migration of an octahedral Li to a neighboring vacant octahedral site that is next to a second octahedral vacancy (Fig. 4.7(b)). A Li ion migrating between the nearest neighbor octahedral sites must perform a curved hop through an adjacent tetrahedral site as illustrated in Fig. 4.7(a) and (b).
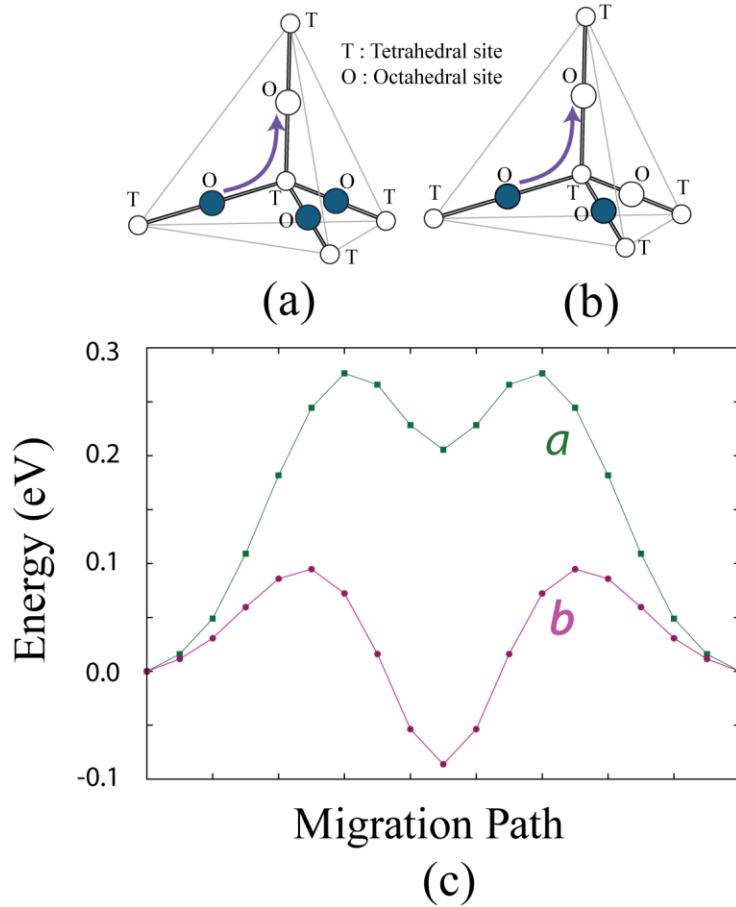
FIG 4.7: Migration energy barrier for different hop environments in β-phase (a) Lithium ion path for a hop with a single vacancy. Octahedral sites are marked as 'O' and tetrahedral sites are marked as 'T'. Blue circles represent occupied octahedral sites and vacant octahedral sites are hollow circles. The hop-path is shown by the arrow. (b) Lithium ion path for a hop with two octahedral vacancies. Color-codes are the same as in figure-(a). (c) Change in energy along the path for a hopping lithium ion in the neighborhood of single vacancy (green squares at the top, curve *a*) and in the neighborhood of two vacancies (pink circles at the bottom, curve *b*)

Figure 4.7(c) shows the calculated energy along the migration paths for the two hops of Fig. 4.7(a) and 4.7(b) as calculated with the NEB method. Curve a in Fig. 4.7(c) (green squares) corresponds to the energy path when an octahedral lithium hops to a neighboring octahedral vacancy through an intermediate tetrahedral site. The tetrahedral site is a local minimum but higher in energy (~200 meV) compared to the octahedral site. The migration barrier for the octahedral to tetrahedral Li hop is ~280 meV, while for the tetrahedral to octahedral hop, it is ~80 meV. When there are two vacancies in the nearest neighbor octahedral sites, the energy curve changes substantially (curve b in Fig. 4.7(c)). The tetrahedral site now becomes more stable than the octahedral site (~90 meV). As a result, the migration barrier for the octahedral to tetrahedral hop is lower (~100 meV) than that for the tetrahedral to octahedral hop (~190 meV). Both of the migration barriers were calculated in the same cubic cell used for most of the barrier calculations in α phase.

The local stability of the intermediate tetrahedral sites in β-$Li_2Ti_2O_4$ in presence of the octahedral single and di-vacancies implies that the hops between the neighboring octahedral sites occur as a sequence of two sub-hops (octahedral → tetrahedral, tetrahedral → octahedral). This is in contrast to the hops between the tetrahedral sites in α-$Li_{1+x}Ti_2O_4$ ($x < 0$) where, as described above, the intermediate octahedral sites are the activated states (i.e., saddle points).

When three octahedral vacancies in β-$Li_2Ti_2O_4$ encounter each other, the energy landscape becomes even more complex. We found that a configuration consisting of three octahedral vacancies surrounding a common vacant tetrahedral site is mechanically unstable: the fourth nearest neighbor octahedral lithium of the vacant tetrahedral site spontaneously relaxes to the tetrahedral vacant site. This implies that once three octahedral vacancies coalesce, tetrahedral occupancy occurs spontaneously. Migration of this tetrahedral Li, however, cannot occur by means of a nearest neighbor tetrahedral to octahedral hop since the end state of this hop is mechanically unstable. One possible mechanism with which a tetrahedral Li surrounded by four octahedral vacancies in β-$Li_2Ti_2O_4$ can migrate is through a coordinated two-atom hop as illustrated in Fig. 4.8. We

did not investigate these possibilities in detail and restrict our analysis to octahedral to tetrahedral hops in the immediate vicinity of the single octahedral vacancies and pairs of octahedral vacancies.
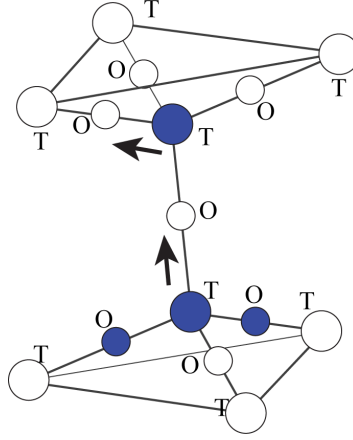
FIG 4.8: An example of a simultaneous two-atom hop. Octahedral sites are marked as 'O' and tetrahedral sites are marked as 'T'. Blue circles represent occupied octahedral sites and vacant sites are hollow circles. Two arrows indicate simultaneous hops of two atoms.

4.2.3.2 Kinetic Monte Carlo simulations

Having established the elementary hop mechanisms in α-$Li_{1+x}Ti_2O_4$ and in stoichiometric β-$Li_2Ti_2O_4$, we next calculated collective Li diffusion coefficients with the kinetic Monte Carlo simulations. The kinetic Monte Carlo simulations sample Li trajectories over the interstitial sites of the Ti_2O_4 spinel host structure, whereby each elementary hop occurs with a frequency given by the transition state theory according to Eq. (2.31). At non-dilute concentrations, the Li ions and vacancies in α-$Li_{1+x}Ti_2O_4$ are disordered, so that the migration barriers, ΔE, appearing in Eq. (2.31) will vary along the trajectory of each Li ion as they depend on the local arrangement of Li ions and vacancies surrounding the Li performing a hop. In α-$Li_{1+x}Ti_2O_4$, the migration barrier for elementary hops between the neighboring tetrahedral sites is the difference in energy between the intermediate octahedral site and the initial tetrahedral site. These energy differences can be calculated directly with the cluster expansion for the configurational

energy described in Sec. 4.2.1. The cluster expansion predicts the configurational energy over both the tetrahedral and octahedral sites of spinel $Li_{1+x}Ti_2O_4$, and as described in Sec. 4.2.1, was optimized to reproduce energy differences between octahedral and tetrahedral site occupancy.

In β-$Li_2Ti_2O_4$, both the octahedral and tetrahedral sites correspond to the local minima and the elementary hops occur between the adjacent octahedral and tetrahedral sites. In this case, the cluster expansion can only be used to predict the end states of the hop. To calculate the migration barriers within the kinetic Monte Carlo in β-$Li_2Ti_2O_4$, we used a method that relies on a cluster expansion for the energies of the end-states of a hop combined with a kinetically resolved activation barrier, ΔE_{KRA}, as described in ref[70]. ΔE_{KRA} for a given hop mechanism corresponds to the average of the forward and backward migration barriers. The actual migration barrier in a particular direction is then equal to ΔE_{KRA} plus the average of the end-state energies minus the energy of the initial state. The dependence of ΔE_{KRA} on the configuration of the surrounding Li ions can be described with a local cluster expansion.[70] In our kinetic Monte Carlo simulations of diffusion in β-$Li_2Ti_2O_4$, we only considered dilute vacancy concentrations (i.e. one vacancy or two vacancies in the Monte Carlo cell) so that the degree of disorder around the migrating Li ions is minimal. In our simulations, we simply used a constant value for ΔE_{KRA} (162 meV) for an octahedral-tetrahedral hop surrounded by an isolated octahedral vacancy and a different value for ΔE_{KRA} (143 meV) for a octahedral-tetrahedral hop surrounded by an octahedral di-vacancy.

The vibrational prefactors, v^*, appearing in Eq. (2.31) were calculated within the local harmonic approximation.[147] Any variation of v^* with concentration and configuration was not taken into account in this study. In α-$Li_{1+x}Ti_2O_4$, we calculated v^* for a lithium hop into an isolated vacancy within the cubic cell (1/8 vacancies over the tetrahedral sites). We used this value of v^*(13.4 THz) over the whole composition range in the kinetic Monte Carlo simulations of α-$Li_{1+x}Ti_2O_4$. In β-$Li_2Ti_2O_4$, we calculated v^* for an octahedral to tetrahedral hop next to a single vacancy among 16 octahedral sites in the

cubic cell. The vibrational prefactor was averaged over the forward and backward hop directions (octahedral → tetrahedral and tetrahedral → octahedral). This averaged value (5.9 THz) was used in the kinetic Monte Carlo simulations for β - $Li_2Ti_2O_4$.

We calculated the self and tracer diffusion coefficients described in Sec. 2.7 by simulating representative Li-ion trajectories in the kinetic Monte Carlo simulations. We used a standard kinetic Monte Carlo algorithm, first proposed by Bortz *et al*.[98, 101] A lithium vacancy configuration representative of the equilibrium state at the temperature and composition of interest was chosen as the initial state of each simulation. For the α phase ($Li_{1+x}Ti_2O_4$, $x<0$) we used a Monte Carlo cell containing 8×8×8 primitive cells (containing 3072 tetrahedral and octahedral sites). 3000 Monte Carlo passes were performed starting from each initial configuration and the trajectories were averaged after 1000 passes (each Monte Carlo pass corresponds to N Li hops where N is the number of Li sites). At each temperature and composition, 100 independent simulations were performed starting from different initial Li-vacancy configurations. At each temperature and composition, self and tracer diffusion coefficients, (as described in Eq. (2.28) and (2.29)), were averaged after every Monte Carlo pass and over independent simulations with different initial configurations.

For the stoichiometric β phase ($Li_2Ti_2O_4$), we calculated diffusion coefficients using kinetic Monte Carlo cells containing either one octahedral vacancy or two octahedral vacancies. In the simulations containing two vacancies, we found that a fraction of the hops proceeds through the di-vacancy mechanism illustrated in Fig. 4.7(b) in which the intermediate tetrahedral occupancy is energetically more favorable than the octahedral end states (Fig. 4.7(c)). The remaining hops proceeded as isolated single vacancy hops. The fraction of divacancy hops depends on the vacancy concentration, which we varied by changing the kinetic Monte Carlo cell size. We found, for example, that approximately 16% of the hops occurred according to the divacancy mechanism for a vacancy concentration of 0.23%, 10% for a vacancy concentration of 0.1% and 7% for vacancy concentration of 0.05%. These vacancy concentrations over the octahedral sites of β - $Li_2Ti_2O_4$ correspond to Li concentrations that are within the predicted two-phase

miscibility gap of the phase diagram of Fig. 4, indicating that the fraction of divacancy hops in stoichiometric β-Li$_2$Ti$_2$O$_4$ is small. By adjusting the kinetic Monte Carlo cell size (to sample different vacancy concentrations), we determined that both the tracer and self-diffusion coefficients scale linearly with vacancy concentration, even for the simulations that contained two octahedral vacancies.
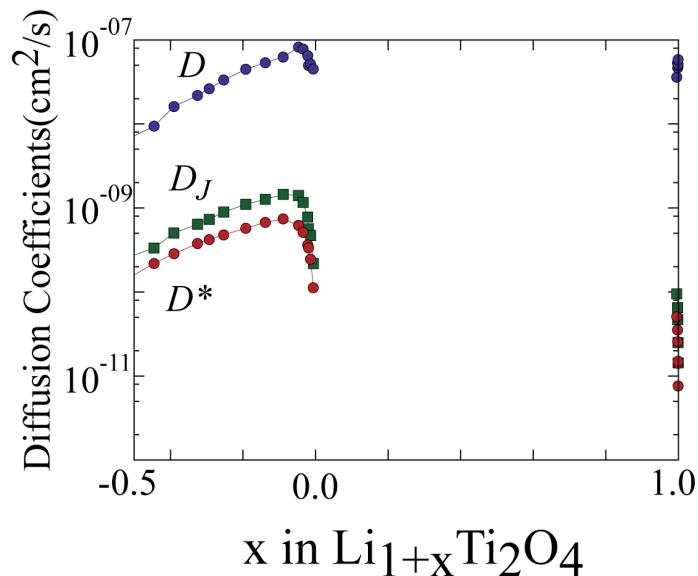
FIG 4.9: Calculated diffusion coefficients as a function of lithium composition. Red circles: tracer diffusion coefficient (D^*), green squares: self-diffusion coefficient (Dj), purple circles: chemical diffusion coefficient (D)

Figure 4.9 illustrates the calculated diffusion coefficients as a function of lithium concentration at room temperature. The chemical diffusion coefficient, D, was calculated by multiplying the self-diffusion coefficient, D_J, with the thermodynamic factor, Θ (of Fig. 4.5). All three diffusion metrics increase with the increasing concentration in α-Li$_{1+x}$Ti$_2$O$_4$ except as the Li concentration approaches $x = 0$. The increase of D^* and D_J in α-Li$_{1+x}$Ti$_2$O$_4$ has its origin in the gradual lowering of the migration barriers with Li concentration, as is predicted with DFT calculations described in Sec. 4.2.3.1 (Fig. 4.6(c)) and reproduced by the cluster expansion used in the kinetic Monte Carlo simulations. As the stoichiometric composition of LiTi$_2$O$_4$ is approached, however, D^* and D_J decrease sharply due to the reduction in the number of tetrahedral vacancies. The

tracer diffusion coefficient is always less than the self-diffusion coefficient. Close to stoichiometric compositions (i.e. $LiTi_2O_4$ and $Li_2Ti_2O_4$), both $D*$ and D_J scale with the vacancy concentration, while the thermodynamic factor scales with the inverse of the Li-sublattice vacancy concentration. The dependencies of D_j and Θ on vacancy concentration in stoichiometric phases cancel each other out when the self-diffusion coefficient and thermodynamic factor are multiplied together to obtain the chemical diffusion coefficient (D). Note that the chemical diffusion coefficients have very similar values in the α and β phases in spite of the fact that the Li hop mechanisms are very different in the two phases.
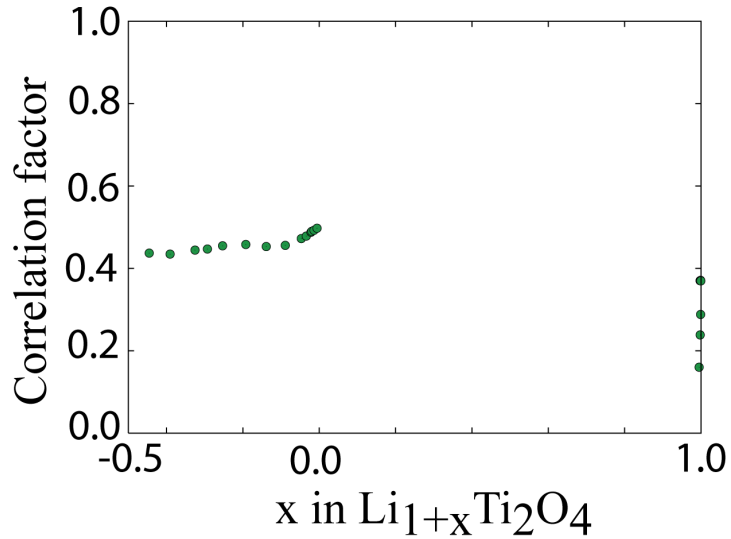
FIG 4.10: Variation of the correlation factor with lithium composition

The correlated motion of lithium ions at non-dilute Li concentrations can be measured with the correlation factor f which is defined as

$$f = \frac{\langle \vec{r}(t)^2 \rangle}{na^2},$$
(4.3)

where $\langle \vec{r}(t)^2 \rangle$ is the average of the squared distance a lithium ion travels after a time t, n is the number of hops and a is the hop distance. The correlation factor, f, measures the degree with which the actual Li tracer diffusion coefficient ($D*$) deviates from what it

would be if Li ions performed a random walk. The correlation factor is equal to one when subsequent Li hops are uncorrelated, as occurs in the dilute limit. However, at non-dilute Li concentrations, Li-ions interact with each other energetically and block potential sites for hops to occur to, thereby introducing correlations between successive Li hops. Figure 4.10 illustrates the calculated variation of the correlation factor f with lithium composition at room temperature. Compaan and Haven analytically calculated the correlation factor in the diamond crystal to be 0.5 in presence of a single vacancy.[148] Figure 4.10 shows that f is slightly less than 0.5 between $-0.5 < x < 0$, becoming equal to 0.5 as x approaches 0, where the vacancy concentration over the tetrahedral sites goes to zero. The correlation factor in the β phase is lower than in the α phase. In the presence of a single vacancy in the β phase, f does not depend on the vacancy composition for small vacancy concentrations, having a value of approximately 0.37. In Monte Carlo cells containing two vacancies, however, f varies strongly with vacancy concentration, decreasing as the vacancy concentration increases. Hops between the nearest neighbor octahedral sites in β-$Li_2Ti_2O_4$ are modeled within the kinetic Monte Carlo simulations as occurring in two steps through the intermediate tetrahedral site. The fact that the Li ions are assumed to thermalize in the tetrahedral sites increases the fraction of return hops to the initial octahedral site.

4.3 Discussion

Intercalation compounds used as electrodes in Li ion batteries come in a wide variety of crystal structures. The crystal structure of an intercalation compound can have a strong influence on the electrochemical properties of an electrode material, including the voltage profile and the concentration dependence of the Li diffusion coefficient. Here we performed a comprehensive study of Li diffusion in the spinel crystal structure, focusing in particular on $Li_{1+x}Ti_2O_4$. The spinel crystal structure is more complex than many other intercalation compounds used as electrodes in Li-ion batteries in that it consists of both tetrahedral and octahedral sites that can be occupied by Li. Below $x = 0$ in spinel $Li_{1+x}Ti_2O_4$, Li occupies the tetrahedral sites, while at $x = 1$, Li occupies the more numerous, but energetically less favorable octahedral sites. A miscibility gap exists

between $x = 0$ and $x = 1$ due to the strong repulsion between pairs of Li ions occupying the nearest neighbor tetrahedral and octahedral sites. Spinel $Li_{1+x}Ti_2O_4$ is very similar in structure to the Li-excess spinel, $Li_{1+x}(Li_{1/6}Ti_{5/6})_2O_2$, an attractive anode material. Both the titanate spinel and its Li-excess variant exhibit the rare trait that their lattice parameters vary negligibly with Li concentration (between $x = 0$ and 1), making them less susceptible than other intercalation compounds to mechanical degradation during Li removal and reinsertion. Our study of the titanate spinel also sheds light on diffusion mechanisms in $Li_xMn_2O_4$ spinel, although the existence of charge ordering over the Mn ions is likely to complicate Li transport in the Mn spinel.

While only a limited concentration interval is accessible experimentally below $x = 0$ in $Li_{1+x}Ti_2O_4$, an advantage of a computational study is that it enables us to investigate the characteristics of Li diffusion within the spinel crystal structure even at concentrations where the host is metastable. Our study of Li diffusion for $x < 0$ has yielded the surprising prediction that the octahedral sites, intermediate between neighboring tetrahedral sites, are in fact the transition states (i.e. saddle points on the energy surface) for elementary Li hops. This is in contrast to what has been predicted for the octahedral sites in the spinel form of $Li_{1+x}Mn_2O_4$, where the octahedral sites for $x < 0$ are local minima.[149] Furthermore, we have found that the difference in energy between the octahedral site and the tetrahedral site decreases with the increasing Li concentration x. Hence the migration barriers for elementary Li hops between tetrahedral sites decreases as more Li ions fill the tetrahedral sites. This trend does not arise solely from a change in crystal dimensions with Li concentration, as was predicted for the layered intercalation compounds.[56, 70] The same trend was found when calculating the migration barriers at different concentrations while holding supercell volume at each concentration fixed to a common value. The decrease in migration barrier with the increasing Li concentration has an electrostatic origin, as an increase in the Li content leads to a progressive reduction of the effective Ti valence from Ti^{4+} at $x = -1$ to $Ti^{3.5+}$ at $x = 0$. Indeed, we found that the difference between the electrostatic energy of Li in the octahedral site and the tetrahedral site decreases as the Ti valence decreases. We expect a similar trend in other spinels, including $Li_{1+x}Mn_2O_4$.

At $x = 1$, where the Li ions occupy octahedral sites, diffusion becomes more complex. The tetrahedral sites between the nearest neighbor octahedral sites are now local minima and hops between octahedral sites proceed in two steps. Furthermore, in presence of a di-vacancy of octahedral sites, the intermediate tetrahedral site actually becomes more stable than the end states.

When serving as an anode, only the voltage plateau between $x = 0$ and 1 in spinel $Li_{1+x}Ti_2O_4$ is cycled over. The plateau signifies two-phase coexistence between $LiTi_2O_4$ and $Li_2Ti_2O_4$ and the insertion or removal of Li ions from the two-phase mixture will require the migration of interfaces separating the coexisting phases. The kinetics of this process can be treated as a standard moving boundary problem,[150] where the velocity of the interface separating $LiTi_2O_4$ domains (tetrahedral occupancy) from $Li_2Ti_2O_4$ domains (octahedral occupancy) depends on the diffusion coefficients within the coexisting phases. Our study has shown that the diffusion coefficients of $LiTi_2O_4$ and $Li_2Ti_2O_4$ do not significantly differ from each other, in spite of the qualitative differences in hop mechanisms at the atomic scale for $x = 0$ and $x = 1$. If the interface between the coexisting phases has a sluggish mobility and thereby becomes the rate-limiting step of Li extraction and insertion, then the additional kinetic coefficients relating interface velocity to differences in thermodynamic potentials across the interface must be determined. At this stage, our understanding of the mobility of interfaces in intercalation compounds remains very limited.[151]

An important difference between the spinel crystal structure and the layered crystal structures of Li_xCoO_2, Li_xTiS_2 and $Li_x(Co_{1/3}Ni_{1/3}Mn_{1/3})O_2$ among others is the dimensionality of the interstitial network. The layered intercalation compounds limit Li diffusion to two-dimensional triangular lattices. Individual Li hops between the neighboring octahedral sites of the layered intercalation compounds pass through an adjacent tetrahedral site and the migration barriers for these hops are significantly reduced if they occur into a di-vacancy.[56, 70] At high Li concentrations, the self and tracer diffusion coefficients therefore scale with the di-vacancy concentration, which to first order is equal to x_V^2 (where, x_V is concentration of vacancy). In spinel $Li_{1+x}Ti_2O_4$

when $x < 0$ in contrast, diffusion is mediated by a single vacancy mechanism such that the tracer and self-diffusion coefficients depend linearly on the vacancy concentration. The correlation factors of Li diffusion also differ substantially between the layered intercalation compounds and spinel, with that of the spinel phase being a factor of 5-10 times larger than that of the layered intercalation compounds at high Li concentrations.[70] The efficiency of redistributing Li ions through a di-vacancy mechanism over a two-dimensional network is significantly lower than through a single vacancy mechanism in a 3-dimensional network. Hence for the same migration barrier for individual hops, the spinel crystal structure should offer Li ions a higher mobility (as measured by D^* and D_J) compared to the layered intercalation compounds.

The present study can be extended to the Li-excess variant, $Li_{1+x}(Li_{1/6}Ti_{5/6})O$, with similar methodological and computational infrastructure. In Li-excess spinel, the excess Li ions occupy a fraction of the Ti octahedral $16d$ sites. The Ti-sublattice will then also exhibit configurational degrees of freedom arising from all possible ways of arranging Li and Ti. The additional configurational degrees of freedom can be treated with a coupled sublattice cluster expansion.[152, 153]

4.4 Conclusions

We have performed a first-principles investigation of the concentration dependent Li diffusion coefficient in spinel $Li_{1+x}Ti_2O_4$ by applying kinetic Monte Carlo simulations to a first-principles cluster expansion of the configurational energy of Li-vacancy disorder over the interstitial sites of the Ti_2O_4 host. Spinel transition metal oxide intercalation compounds such as $Li_xMn_2O_4$ and $Li_{1+x}(Li_{1/6}Ti_{5/6})O_2$ are important electrode materials for Li-ion batteries. The present study has demonstrated that the octahedral sites are activated states for Li hops between the neighboring tetrahedral sites when $x < 0$ in $Li_{1+x}Ti_2O_4$. Furthermore, the migration barriers for hops between the neighboring tetrahedral sites are sensitive to Li concentration, decreasing with increasing x. We have been able to attribute this decrease with an increase in the effective Ti valence states as Li is added to the host, which penalizes the octahedral site more than the tetrahedral site. In $Li_2Ti_2O_4$, Li ions

occupy octahedral sites and migrate by passing through intermediate tetrahedral sites, which are predicted to be locally stable (as opposed to being saddle points in the energy landscape). The predicted Li diffusion coefficient varies by several orders of magnitude with Li concentration for $x < 0$. In spite of the qualitative difference in hop mechanisms in $LiTi_2O_4$ and $Li_2Ti_2O_4$, their Li diffusion coefficients are nevertheless very similar in value. Our study provides insight about the effect of crystallographic features in spinel and layered intercalation compounds on Li mobility.

Chapter 5

Competing mechanisms of non-dilute Li-diffusion in spinel-Li$_x$TiS$_2$

5.1 Introduction

Diffusion of Li-ions directly dictates the charge-discharge rate and the thermodynamic reversibility of the Li-ion battery electrodes. While graphite is the most common anode material,[49, 154, 155] transition metal intercalation compounds serve as the cathode materials in present day Li-ion batteries.[43, 44, 128, 156-159] These intercalation compounds have a reasonably stable host structure that deforms negligibly with the change in Li-concentration. Li-ions sit in the interstitial sites of this host.

Both the crystal structure and the chemical composition of the host have significant effect on the Li-diffusion kinetics. The Li-diffusion network can be one-dimensional (e.g., Olivine such as LiFePO$_4$),[69, 160] two-dimensional (e.g., layered LiCoO$_2$)[56, 70, 118, 161] or three-dimensional (e.g., spinel-LiTiO$_2$).[47, 60, 61, 128, 135, 162] It is generally expected that the higher the dimensionality of Li-diffusion network, the higher the diffusivities. However, the nature of this dependence of Li-mobility on the interstitial sites is not clear, especially in the non-dilute regime. Moreover, within similar crystal structure, cations and anions can vary widely. A typical positive electrode is made of oxides or sulfides of the transition metals such as, Co, Mn, Ti, Ni. In general, oxides give higher voltage than sulfides while sulfides are kinetically more efficient than oxides.

Again, the nature of this effect of anions on the diffusion kinetics needs to be characterized.

There have been several first-principles studies on diffusion behavior of Li in the intercalation compounds in recent years. In layered $O3$-$LiCoO_2$, it has been shown that the clusters of the two nearest neighbor vacancies (di-vacancy) form the major diffusion mediating defect cluster in the two-dimensional sheets of interstitial sites.[70] Moreover, it has been observed that there is a systematic elongation of c-lattice parameter with the increasing Li-concentration.[163] This change in crystal dimension brings down the migration energy associated with the individual Li-hops. Hence, there is an increasing trend in Li-mobility with concentration. Diffusivity drops again at the dilute-vacancy limit where diffusion mediating di-vacancies become rare. Similar trend of the c-lattice parameter is observed during the Li-intercalation in the graphite-anodes.[49, 164] In the layered form of Li_xTiS_2, similar kinetic behavior is observed where di-vacancies play the crucial role of diffusion mediation and there is significant c-lattice parameter change with Li-composition.[56] Diffusion in spinel-Li_xTiO_2, on the other hand, occurs in the three dimensional network of interstitial sites as discussed in chapter 4 of the present thesis. There is negligible lattice parameter change with Li-intercalation and the single vacancies are the diffusion mediating defects. Moreover, in spinel-Li_xTiO_2, diffusion has been observed to be significantly faster compared to layered-Li_xTiS_2.

In the present study, we elucidate Li-diffusion in spinel titanium sulfide. Knowledge of diffusion in this material can complement the previous studies, as it can compare two anion-chemistries and two crystal structures at the same time keeping everything else the same. The present study would complete the comparison triangle and help associate the changes in kinetic behavior with the changes in chemical components or crystal structures. In this compound, Li occupies the octahedral sites instead of the tetrahedral sites. The hop-mediating tetrahedral sites are coordinated with four octahedral nearest neighbors, while for layered Li_xTiS_2, the intermediate tetrahedral site of the hop is coordinated to only two nearest neighbor octahedral sites. Therefore, spinel-Li_xTiS_2 offers greater opportunity to study the effects of various local environments. We use a

coupled approach of the electronic structure method and the cluster expansion technique combined with the statistical mechanical tool such as Monte Carlo simulations to illustrate both thermodynamic and kinetic behavior. We first examine the elementary hop mechanisms and their relative importance. In the kinetic Monte Carlo simulations, we track the relative frequencies of different mechanisms and relate the observed kinetic behavior to these frequencies. To conclude, we discuss the overall understanding gained from this study in the context of the general diffusion process in intercalation compounds.

5.2 Results

5.2.1 Crystal structure and site stability

Spinel titanium sufide is isostructural with spinel titanium oxide. The sulfur atoms take the place of the oxygen atoms. The spinel form of titanium sulfide acts as a robust host for Li intercalation. The host structure deforms negligibly over the relevant Li-composition range. Fig 5.1 illustrates the spinel crystal structure and the available interstitial sites.
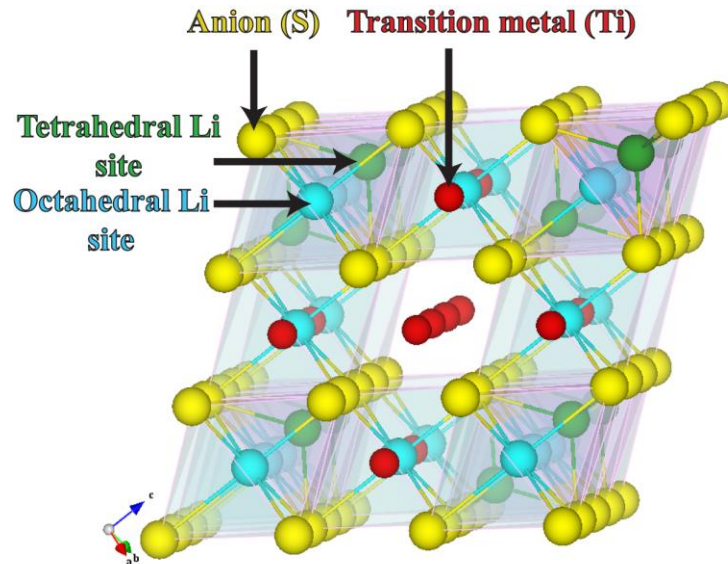
FIG 5.1: Crystal structure of Li_xTiS_2. Sulfur atoms (Yellow) form an FCC lattice. Ti atoms (Red) occupy half of the octahedral sites. The other half of the octahedral sites (Cyan) and all the tetrahedral sites (Green) are available for lithium intercalation.

We calculated the total energies of 159 symmetrically non-equivalent arrangements of Li and vacancies over the interstitial sites (both tetrahedral and octahedral) in super cells consisting of up to 4 primitive cells from first principles. A uniformly dense grid of k-points ($8\times8\times8$ k-points per primitive cell) was chosen for all these calculations based on the k-point convergence test. The formation energies of these configurations have been calculated with reference to the delithiated spinel (Ti_2S_4) and fully lithiated spinel ($Li_2Ti_2S_4$) having one lithium per transition metal atom. All the ground states on the convex hull contain only octahedral Li. The configurations with tetrahedral Li are higher in energy compared to the octahedrally occupied members at the same composition. This demonstrates that Li prefers the octahedral sites over the tetrahedral sites and this behavior persists over the entire composition range between TiS_2 and $LiTiS_2$.

We fit a cluster expansion consisting of 30 Effective Cluster Interactions (ECI) to the 159 DFT formation energies. The cluster expansion has a RMS error of 1.75 meV per Li_xTiS_2 formula unit and a weighted cross-validation score of 6 meV per Li_xTiS_2 formula unit.

In the Grand canonical Monte Carlo simulation, at room temperature (with 1000 passes for equilibration and 3000 passes for averaging), equilibrium composition of Li is tracked for different chemical potentials. The smooth change of chemical potential indicates solid solution behavior for the entire composition range (plot not shown here). The site occupancies at moderate temperature are also tracked in Monte Carlo simulation and it is observed (plot not shown here) that the tetrahedral sites are never occupied by Li-ions even at room temperature.

5.2.2 Elementary Li-hops and migration barriers

Macroscopic diffusion in intercalation compounds occurs as a result of many elementary Li hops to neighboring vacancies. In spinel-Li_xTiS_2, DFT energy calculations and the finite temperature Monte Carlo simulations predict that Li ions prefer the octahedral sites. The tetrahedral sites are higher in energy but are local minima. The Li-migration path between the octahedral sites is curved and passes through a tetrahedral site. This path is a low energy path and the NEB calculation of this hop predicts the tetrahedral sites to be a

local minimum. Hence, a Li ion thermalizes in the tetrahedral site continuing to another octahedral vacancy or hopping back to the original octahedral site it started from. The end state energies as well as the associated migration barrier depend on the local arrangement of Li and vacancies, especially at non-dilute Li-concentrations. This local environment dependence needs to be accounted for to accurately quantify the non-dilute Li-diffusion in spinel-$Li_x TiS_2$.

A Li ion at octahedral site hopping into the nearest neighbor tetrahedral vacancy, sees different immediate local environments. The tetrahedral vacancy has four nearest neighbor octahedral sites, one of which is occupied by the hopping Li. Among the other three octahedral sites, number of Li ions varies from zero to three. If it is zero, the hop is called a triple-vacancy hop as the end state of the hop, the tetrahedral site, is surrounded by three vacancies at the initial state (fig 5.2(c)). In similar argument, there can be di-vacancy (fig 5.2(b)) or single-vacancy (fig 5.2(a)) hops. If all three octahedral sites (other than the one with the hopping Li) are occupied, it is a case of the zero-vacancy hop, following the similar nomenclature. A zero-vacancy hop is never possible as the end state is not energetically stable.

It is worth noting at this point that though the tetrahedral sites are stable and Li ions thermalize at these sites, octahedral sites are the only sites occupied at equilibrium for the whole range of Li-concentration (according to the Monte Carlo simulations). Diffusion is a non-equilibrium process. Nevertheless, it can be shown that diffusion is governed by the perturbations around the equilibrium. Hence, hops originating from the octahedral sites (octahedral hops) are the important hops that govern the diffusion process. Hops originating from the tetrahedral sites (tetrahedral hops) occur only as a subsequent event of an octahedral hop. Therefore, migration barriers associated with the octahedral hops critically control diffusion behavior. Dependence of these migration barriers on local environments needs proper investigation.

The energy paths for the Li-hops were calculated through NEB calculation as implemented in VASP. All NEB calculations have been done under constant volume constraint and the volume has been chosen to be the average of the volumes of the two

fully relaxed end-states. We explored local-environment effect on the migration barriers in a cubic super cell consisting of 32 oxygen, 16 titanium and variable number of lithium ions. Fig 5.2 shows the path and energy for several important atomic hops. In fig 5.2(a), the physical arrangement of the nearest neighbor cell around the unit cell is shown when a Li ion at the octahedral site hops to the nearest neighbor tetrahedral vacancy with a single octahedral vacancy around it. The octahedral sites further from the nearest neighbor ones of the tetrahedral site are occupied by Li. Only the octahedra around the hop are shown and the rest of the super cell has been omitted for the sake of clarity. Figures 5.2(b) and 5.2(c) depict the arrangements when two and three nearest neighbor octahedral vacancies are available around the hop, respectively. The corresponding migration energy paths are shown in fig 5.2(d). Fig 5.2(d) clearly shows that different immediate hop-environments result in very different migration barriers. For the single-vacancy hop (circles), the energy barrier is very high (~600 meV), while for the di-vacancy hop (solid squares), it is ~420 meV and for the triple-vacancy hop (hollow squares), it is the lowest (~230 meV). These are the values of energy barriers that an octahedral Li needs to overcome to hop to the nearest neighbor tetrahedral vacancy.

(a)

(b)

(c)

(d)

79
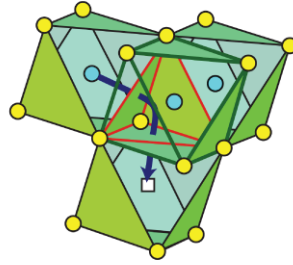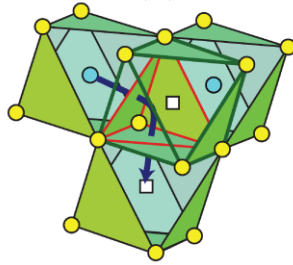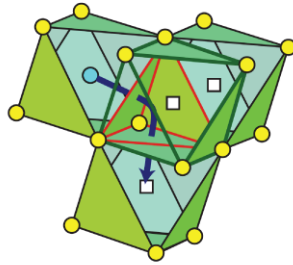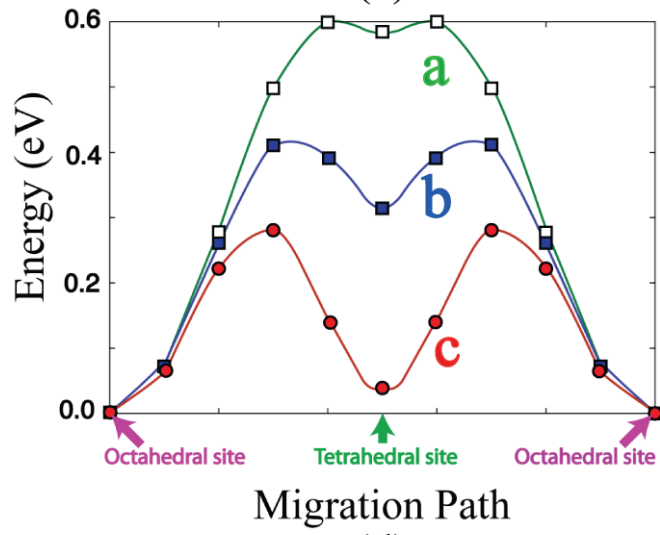
FIG 5.2: Migration paths for three different immediate environments. Curvilinear Li-hop between two nearest neighbor octahedral sites through the intermediate tetrahedral sites with (a) a single vacancy (b) two vacancies (c) three vacancies among four nearest neighbor octahedral sites. (d) Energy paths associated with each of these hops. The top curve (hollow squares), the middle curve (filled blue squares) and the bottom curve (filled red circles) correspond to the energy paths for single-, di- and triple vacancy environments, respectively.

We further explored migration barriers in different configurations at different Li-concentrations in the same cubic super cell. Fig 5.3 shows the migration barriers for Li-hops from the octahedral sites to the tetrahedral sites in three different nearest neighbor Li-occupancies but having different Li-concentrations and Li-vacancy configurations further away from the migrating Li. In this figure, hollow squares correspond to single vacancy hops; the filled squares and circles correspond to di- and triple-vacancy hops respectively. We can observe that there are three distinct bands of energy barrier values, each corresponding to a particular immediate hop-environment. The lowest band of energy barriers corresponds to the triple vacancy hops (a Li hopping into a tetrahedral site surrounded by three vacancies). There are some variations in barrier for different configurations at the same concentration and a pronounced variation with concentration. The migration barriers for triple vacancy hops tend to decrease with the increasing Li-content. Similarly, for di-vacancy hops (filled squares), there is some configurational dependence along with a weaker composition dependence compared to the triple vacancy hops, also decreasing with the increasing Li concentration.
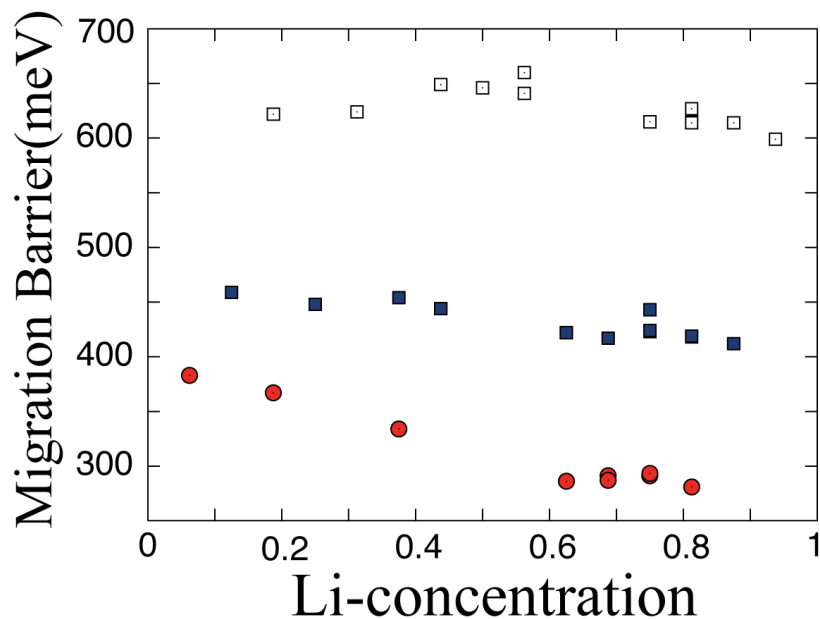
FIG 5.3: Migration barriers for octahedral hops for different mechanisms at different Li-compositions. The hollow squares, the blue filled squares and the red filled circles represent migration barriers for single-, di- and triple vacancy mechanisms, respectively.
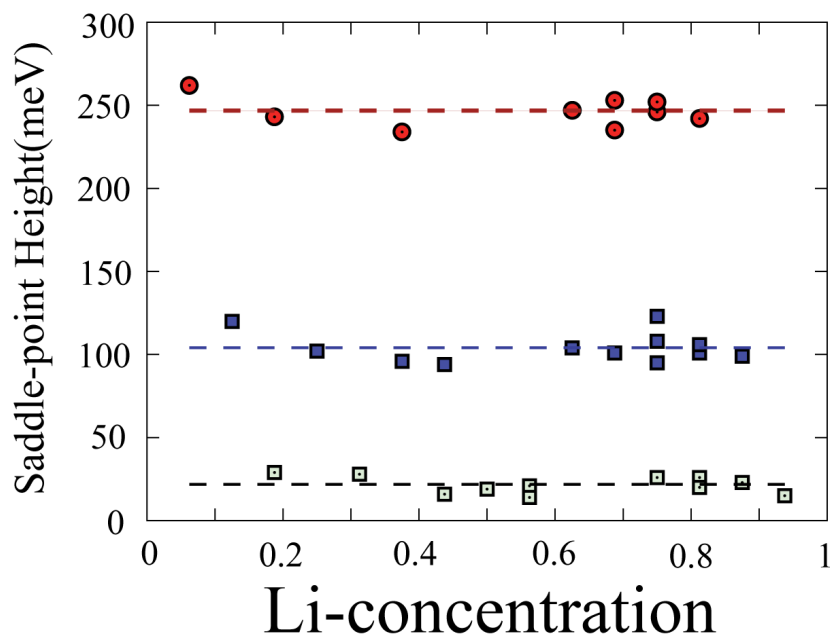
FIG 5.4: Saddle point heights (compared to the tetrahedral site energy) for different mechanisms at different Li-compositions. The hollow squares, the blue filled squares and

the red filled circles represent saddle point heights for single-, di- and triple vacancy mechanisms, respectively. A dashed line represents the average value of the saddle point height for the coresponding hop-mechanism.

Fig 5.3 showed some variation of the migration barrier for the octahedral hops (octahedral $\rightarrow$ tetrahedral). If we look at the saddle-point height from the tetrahedral site energy, this variation with composition is negligibly small (fig 5.4). This fact was used for calculating the migration barriers in the kinetic Monte Carlo simulations. The migration barrier for an octahedral hop can be reconstructed by the summation of the two terms: (i) the difference of energies between the tetrahedral and the octahedral Li (ii) the energy height of the saddle-point from the tetrahedral site. This has been schematically shown in figure 2.1(c). Our cluster expansion encompasses both the octahedral and the tetrahedral sites. Therefore, it reproduces both the end-state energies, hence the energy difference, with reasonable accuracy. The energy height of the saddle point from the tetrahedral reference site is not reproduced by the cluster expansion. The data points in fig 5.4 correspond to the same calculations that fig 5.3 shows the results for. Here, we observe similar bands of energies for three immediate local environments. We note that the fluctuations between different concentrations and different configurations for the same concentration are small. The dashed lines shown in each band represent the arithmetic mean of all the values in that band. The deviations from this mean value is not more than 20 meV in any band. If we take these mean values as the constant energy heights for three immediate local environments, we accept the error bar to be within this 20 meV. The cluster expansion has an RMS error of 1.75 meV per Li_xTiS_2 formula unit and for the calculation cell with 16 Ti atoms the error accumulates over 20 meV. Also the accepted error bar for DFT calculations is 5 meV per formula unit. In allowing a range of 20 meV variation in saddle point heights we are not outside the error bar that we accept for the cluster expansion and DFT calculations. Therefore, we model the saddle point energy heights to be three constants each for a particular immediate local environment: 22 meV for the single vacancy hop, 104 meV for the di-vacancy hop and 247 meV for the triple vacancy hop. By taking a constant value for the whole band of saddle-point heights,

we acknowledge the fact that the information only about the nearest neighbor occupations around a hop is sufficient to determine the migration barrier.

5.2.2 Diffusion behavior of lithium

To study Li diffusion in Ti_2S_4 spinel host, we use kinetic Monte Carlo (KMC) simulations. The migration barriers are calculated using the cluster expansion parameterized by the first-principles energies. Along with the effective Hamiltonian (the cluster expansion), we use a model for the saddle point energy heights to reproduce migration barrier for an arbitrary configuration at any concentration. We have calculated vibrational prefactor (v^*) by calculating frequencies from first-principles within the local harmonic approximation. The dependence of the vibrational prefactor on changes in composition as well as the changes in hop-environment was found to be small. Therefore, we used two values corresponding to each direction: 3.1 THz for the octahedral hops and 7.1 THz for the tetrahedral hops.

In the KMC simulations, for each initial configuration, we used 1000 Monte Carlo passes for equilibration and another 1000 for averaging different displacement metrics and fluctuation variables. We used 100 initial configurations for one concentration and averaged the relevant quantities over these different ensemble runs.
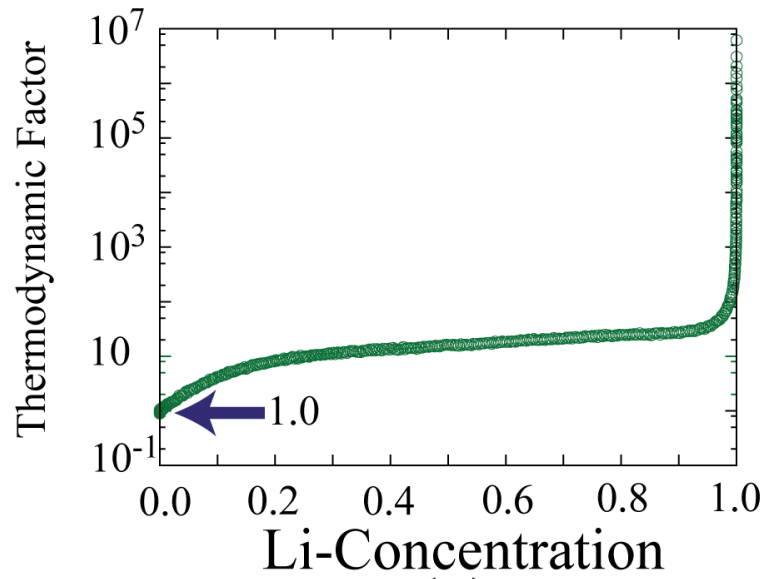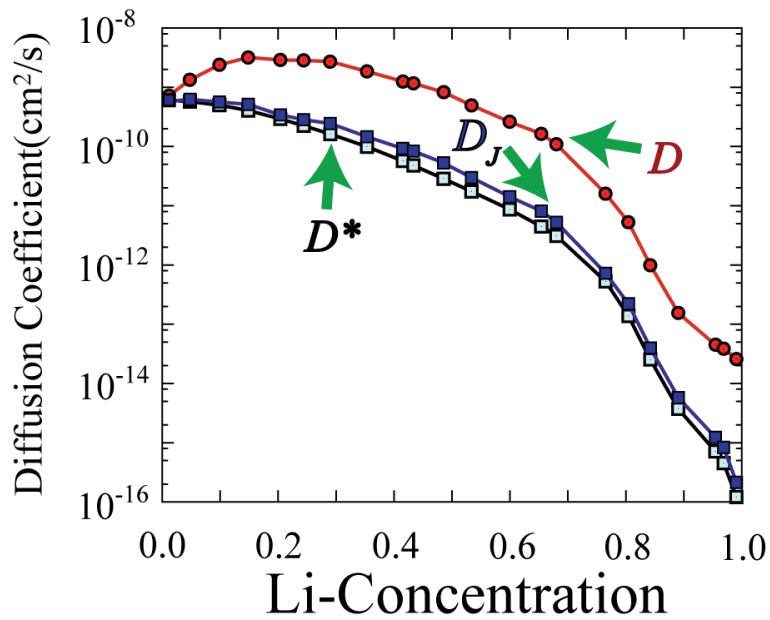
FIG 5.5: (a) Variation of thermodynamic factor with lithium concentration. At dilute lithium limit, the factor matches with the theoretical value of unity. (b) Variation of diffusion metrics as functions of lithium concentration. The hollow squares, the filled blue squares and the filled red circles represent tracer diffusion coefficient, self diffusion coefficient and chemical diffusion coefficient, respectively.

The different diffusion metrics are plotted at fig 5.5(b). The curve represented by the hollow squares shows the variation of tracer diffusion coefficient (D^*). The curve with the solid squares corresponds to the jump diffusion coefficient (D_J). Both D_J and D^* decrease monotonically with concentration having similar curve-shapes, D_J having slightly greater numerical value compared to D^*. The values of D^* and D_J range from ~10^{-8} cm^2/s and ~10^{-16} cm^2/s, spreading over a window of 8 orders of magnitude. In Fig 5.5(a), the thermodynamic factor (Θ), as calculated in the grand canonical Monte Carlo simulations, is plotted as a function of Li-concentration. Θ is unity at the dilute limit, consistent with the fact that as $x \rightarrow 0$, the Li-ions behave as in an ideal solution. It increases rapidly by an order of magnitude as the Li-concentration increases ranging between 10 and 30 for most Li-concentrations. Θ diverges close to the stoichiometric phase of the fully lithiated spinel where Li-ions fill all the octahedral sites. The product of this thermodynamic factor and the jump diffusion coefficient yields the chemical diffusion coefficient (D) (red circles in fig 5.5(b)). D is numerically identical to D_J in the dilute limit, as Θ is unity. Near this dilute limit, it increases with the increase in Θ. However D_J drops much more rapidly than Θ increases and this results in the gradual drop in the chemical diffusion coefficient. Near the fully-lithiated limit, the rapid increase in Θ causes D to drop at a slower rate than D_J. The chemical diffusion coefficient varies between ~10^{-8} cm^2/s to ~ 10^{-13} cm^2/s. This variation has significant implications for the charge-discharge behavior of TiS_2 spinel system and stresses the fact that the study of non-dilute diffusion is critical in understanding the intercalation kinetics.
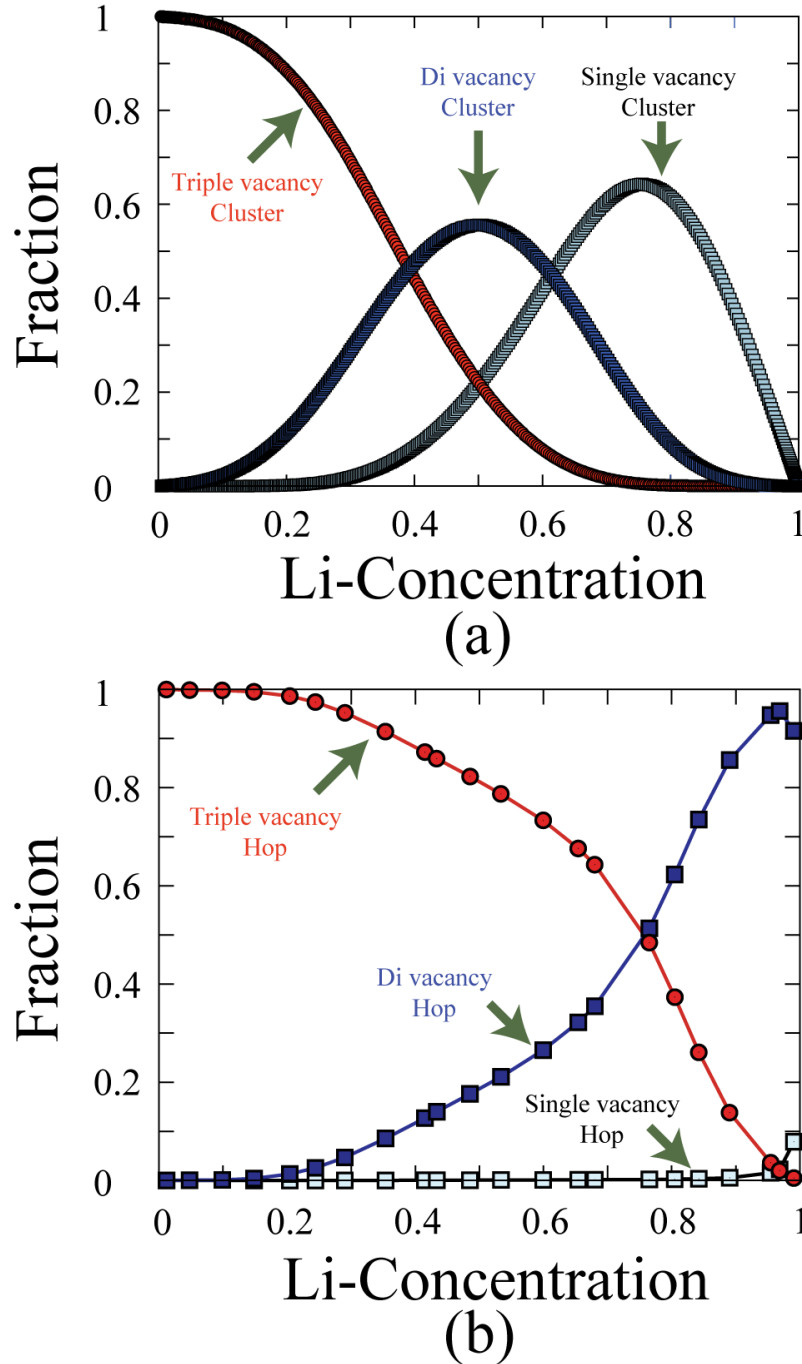
FIG 5.6: (a) Variation of the fractions of average availability of single-, di- and triple-vacancy environments. The possibility of zero-vacancy environment is kept out of the count as it does not contribute to the diffusion process. (b) Average fraction of frequencies of the different hop mechanisms as sampled in the kinetic Monte Carlo simulations. The hollow squares, the filled blue squares and the filled red circles

represent fraction of frequencies corresponding to single-, di- and triple-vacancy hops, respectively.

The large variation of D and D_J with Li-composition is a direct result of the strong dependence of the migration barriers on the local Li-environments. The average availability of these local environments can be tracked in the grand canonical Monte Carlo simulations. Fig 5.6(a) shows the relative abundance of the single-, di- and triple-vacancy environments around each candidate diffusive Li-atom. At low Li-concentration, almost all the diffusing Li-atoms encounter the triple-vacancy environments (red circles in fig 5.6(a)). On the other hand, at high Li-composition, single-vacancy environment (hollow squares) dominates significantly in relative abundance. In the mid-stage of lithiation, all three environments occur in significant numbers while di-vacancy ones (solid squares) dominate over the others. At the lithiated limit, the vacancy becomes extremely rare and all the hop environments cease to exist. The zero-vacancy environments (which are insignificant from the diffusion point of view) are kept out of the count in fig 5.6(a). Therefore, the sum does not add up to unity, especially at the non-dilute Li-concentrations, where the number of zero-vacancy environments increases with Li-composition.

The availability of a particular environment does not necessarily mean that a Li executes a diffusive hop in that environment. Each of these environments has a different migration barrier. As the probability associated with a particular hop is related to the negative exponential of the barrier energy, a triple vacancy hop is the most probable one, when all three types of hop environments are equally available. However, as we observe from fig 5.6(a), different hop-environments are prevalent in the different stages of intercalation. Therefore, these variations in availability put bias on how frequently a particular hop-environment is sampled. Fig 5.6(b) shows the relative frequency of the hop-environments sampled in the diffusion process, as tracked in the kinetic Monte Carlo simulations. As any one of the three relevant environments is associated with each Li-hop, the sum of these fractions at any concentration is unity. At low lithium concentration, the triple vacancy environments are the most abundant and the triple vacancy hops substantially

dominate over the other two types of hop. However, as di-vacancy environments become more readily available at higher Li-concentration, a considerable fraction of di-vacancy hops occurs. In the dilute vacancy limit, the system is left with mostly single vacancy environments barring a few di-vacancy environments. It is only then when a few single vacancy hops are executed by the Li-ions. This trend is consistent with the order of the migration barriers associated with each hop-environment. The fraction of the sampled frequency for di-vacancy hops goes up with the increasing di-vacancy availability and dominates over triple-vacancy hops over concentrations of 75%. At the dilute vacancy limit, di-vacancy hops become rare compared to the single-vacancy hops and hence the fraction of di-vacancy hops drops. This drop is due to the small fraction of Li-ions choosing the high-energy-barrier single vacancy option.
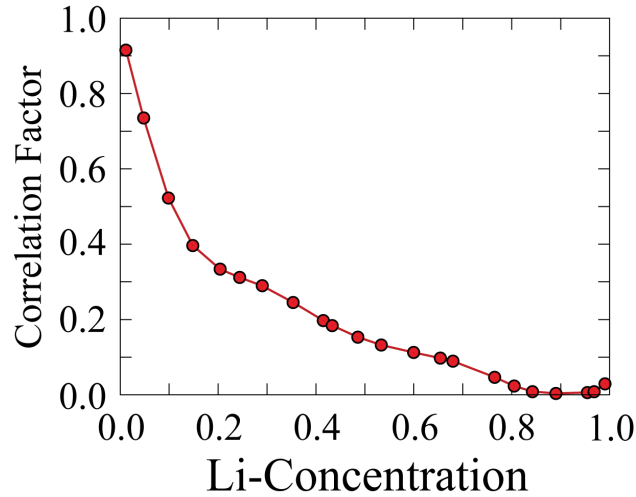
FIG 5.7: Variation of lithium correlation factor with concentration.

The correlation factor (f) measures the deviation of the tracer diffusion coefficient (D*) from what it would be, if all successive Li-hops were uncorrelated (i.e., random walk). Mathematically the correlation factor can be calculated from eq. 4.3. At the dilute limit, successive hops of the sparsely distributed Li-ions will be largely uncorrelated and the correlation factor tends to unity. On the other hand, at the dilute vacancy limit (high Li concentration), correlations between successive Li-hops will be significant. The analytical estimate of the correlation factor [148, 165] at the dilute vacancy limit can be obtained from the coordination number of the end points of the Li-hops (1-2/z, where z is

the coordination number).[165] Each octahedral Li is coordinated to two nearest neighbor tetrahedral vacancies. Therefore, z takes a value 2 and the formula predicts the correlation factor to be zero. In figure 5.7, we show the correlation factor calculated from the KMC simulations. At both the limits, it matches perfectly with the analytical estimates. It tends to unity in the dilute Li limit and decreases smoothly to zero as the correlation between different Li-hops becomes more and more pronounced.

5.3 Discussion

The study of Li diffusion in TiS_2-spinel elucidates some fundamental aspects of diffusion in the intercalation compounds in general. Spinel has an interesting crystal structure which offers two kinds of interstitial sites, octahedral and tetrahedral. Depending on the pair of anion and the concentration of the diffusing species, the octahedral or the tetrahedral sites are populated during the intercalation process. In the case of Li-diffusion, both the octahedral and the tetrahedral sites play a crucial role. The tetrahedral sites are predicted to be higher in energy from zero-Kelvin DFT calculations and even at room temperature they are not occupied. However, these tetrahedral sites are the intermediate stable sites as Li-ions hop between octahedral sites during the diffusion process. In chapter 4, studies of Li-intercalation in titanium oxide spinel ($Li_{1+x}Ti_2O_4$) show that the system is phase-separated between the tetrahedral and the octahedral Li-occupancies. In the phase with the tetrahedral Li-occupancy, the octahedral sites are the saddle points. On the other hand, in the phase with the octahedral Li-occupancy, the tetrahedral sites are the local minima and the degree of stability of the tetrahedral sites is directly affected by the occupation of the nearest neighbor octahedral sites, as in the case of $Li_xTi_2S_4$. However, in $Li_{1+x}Ti_2O_4$, these two distinct behaviors are found in two different phases stable at different levels of Li-intercalation separated by a miscibility gap. In the manganese oxide spinel, we see similar site preference by intercalating Li-ions as in titanium oxide spinel[60, 128] and observe similar behavior in the Li-excess variant of titanate spinel ($Li_{1+x}(Li_{1/6}Ti_{5/6})_2O_4$).[127, 135-138] This comparison highlights the effect of anion on the site stability and electrochemical behavior of the spinel host.

We explored the dependence of migration barriers on configuration and composition extensively in the present study. We have looked into 33 different Li-hops covering different configurations of the surrounding Li-sites and the whole composition range. The clear segregation of the energy barrier data points in three bands, for the three types of surrounding occupations of the immediate vicinity of the hop, demonstrate how strongly migration barriers depend on the immediate local environment. The decreasing trend of the migration barrier for the triple- and di-vacancy octahedral hops with Li-concentration can be attributed to the monotonic increase of lattice volume with composition, where lattice constant changes by 4% over the composition range (result not shown here).

It is observed that the interplay between the two factors, the relative abundance and the relative preference of the competing mechanisms, govern the diffusion process in the non-dilute regime. In the case of the layered intercalation compounds (such as, Li_xCoO_2 or layered-Li_xTiS_2), only one mechanism (di-vacancy mechanism) dominates the diffusion process in the whole concentration range and diffusivity drops sharply with the drop in the availability of this mechanism at the dilute vacancy limit.[56, 70] In the dilute phase of spinel-titanate (with tetrahedral Li-occupancy), single-vacancy hop is the only available mechanism and it remains effective very close to the dilute vacancy limit. In case of Li_xTiS_2-spinel, different mechanisms take over in different stages of intercalation. In the significant part of the concentration range, triple- and di-vacancy mechanisms vie for the dominance and only at the dilute vacancy limit, single vacancy hops contribute slightly in the diffusion process. This is reflected in the non-dilute diffusivity values (specifically D_J and D^* values) as they drop steadily with concentration consistent with the relative dominance of the hops and associated migration barriers. The present study contributes to the extension of the understanding of the diffusion kinetics in the intercalation compounds from the previous fundamental investigations on other materials.

We gain some fundamental insight from the present study both for the design of future materials and for developing intuitions for predicting the kinetic behavior of the new intercalation compounds. Hops with an intermediate site, having coordination of multiple nearest neighbors, have a significant effect on the diffusion kinetics. In the dilute phase of

$Li_{1+x}Ti_2O_4$ (with tetrahedral Li-ions), a Li-ion jumps between two tetrahedral sites through the intermediate octahedral site, which is a saddle point. The intermediate octahedral site is coordinated only to the end states of the hop. The occupation status of the end states is predetermined and there is no option of alternation. This fact leaves the system with only one available mechanism of diffusion – a single vacancy hop. The migration barrier associated with that hop solely dictates the diffusivity in the non-dilute regime. In the case of Li_xTiS_2, any hop consists of the two octahedral end states and an intermediate stable tetrahedral site. The intermediate site is coordinated with the four nearest neighbor octahedral sites. This results in the flexibility of the diffusing Li-ions to choose from the three possible mechanisms: triple-, di- and single-vacancy hops. The choice is based on the relative energy barriers of the hops. If the single vacancy hop has a high energy barrier, the diffusing ion can bypass that hop and be able to diffuse efficiently through lower energy di- or triple vacancy hops. The availability of the alternative paths contributes to the efficiency of the kinetics. Therefore, it is essential to explore the coordination of the intermediate site of a hop in understanding diffusion kinetics in a new intercalation compound.

5.4 Conclusion

We have performed a comprehensive study of Li diffusion in spinel-Li_xTiS_2. This chapter elucidates the effect of crystal structure and anion chemistry on diffusion kinetics in intercalation compounds. It complements chapter 4 by elucidating the effect of anion on the site preference and hence the diffusion paths. Titanium sulfide spinel also offered more possible hop mechanisms compared to titanate spinel. The competitive migration energy values for three mechanisms do not allow a single mechanism to dominate for the whole composition range as in case of layered intercalation compounds or spinel titanate. It is observed that the multiple-coordination for the intermediate site of a hop increases efficiency of diffusion kinetics. This is an important observation for the design of kinetically favorable materials.

Chapter 6

Non-dilute Cu-diffusion in spinel-$Cu_x TiS_2$

6.1 Introduction

In the previous two chapters we have discussed the Li-diffusion behavior in spinel crystal structure. We have examined both oxide spinel and sulfide spinel for the same transition metal, titanium. The change in anion significantly affected the diffusion behavior. In this chapter, we are going to report how change in diffusing species can alter the diffusion process on the same crystal structure. This will complete the comparison triangle with crystal structure, anion-chemistry and diffusing species as three vertices.

Diffusion of Cu has critical influence in the performance of $Cu_{0.5}TiS_2$ electrodes that rely upon the displacement reaction.[166] Before the charging of the cell, the delithiated electrode contains Cu-ions at the interstitial sites of the TiS_2 host. During charging Li-ions displace the Cu-ions and metallic Cu-beads accumulate on the surface of the electrode. During the discharging process, when Li ions move out from the cathode host, Cu-ions move back to the interstitial sites. This displacement reaction has completely different voltage curves for the charge and the discharge process.[166] The enormous hysteresis in the electrochemical behavior can be elucidated from the kinetic behavior of Li and Cu in the titanium sulfide spinel host.

6.2 Results

6.2.1 Crystal structure and site stability

The host structure of TiS_2 has been described in chapter 5 (fig. 5.1). Cu ions prefer to be in the tetrahedral sites for the whole composition range (between Ti_2S_4 and $CuTi_2S_4$). The octahedral sites are saddle points rather than local minima (fig 6.2). Hence for the whole composition range, tetrahedral sites are the only interstitial sites available for Cu intercalation. We calculated 22 non-equivalent configurations of Cu and vacancy arrangement over the tetrahedral lattice. The reference states are set at the two ends of the composition range. The calculated formation energies and the associated convex hull are shown in fig 6.1(a). These formation energies were used to parameterize a cluster expansion consisting of 10 ECI's, which has less than 0.5 meV RMS error and 2.75 meV weighted cross-validation score per TiS_2 formula unit. When we subject the cluster expansion Hamiltonian to the grand canonical Monte Carlo simulation, we track the equilibrium chemical potential as a function of Cu-concentration (fig 6.1(b)). The smooth variation and absence of steps and plateaus in the chemical potential plot indicate that Cu forms a solid solution with the TiS_2 spinel host.
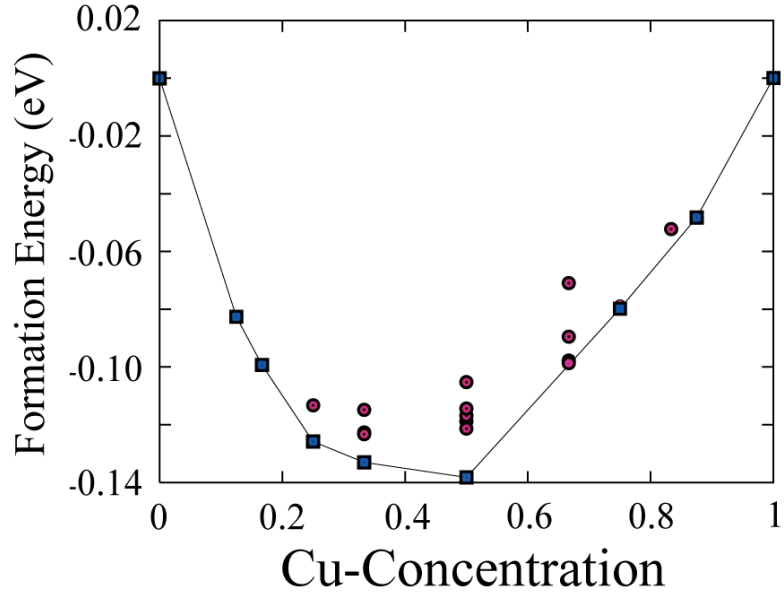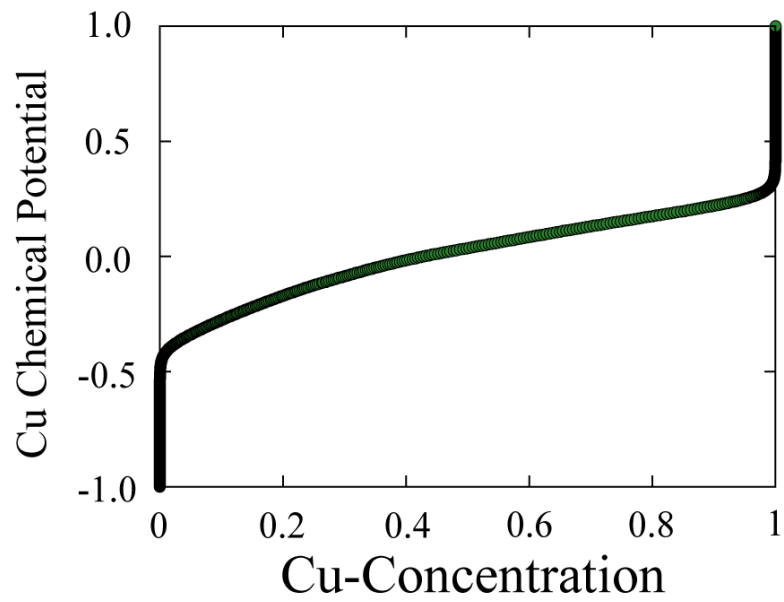
FIG 6.1: (a) Formation energies and the associated convex hull for different Cu-vacancy orderings at different Cu-concentration. The convex hull is represented by the blue line connecting the filled blue squares. (b) Equilibrium chemical potential curve as a function of Cu concentration as tracked in the grand canonical Monte Carlo simulations.

6.2.2 Elementary hops and migration barrier

For the study of diffusion behavior, we first looked at the individual atomic hops for Cu. We used the similar cubic super cell for NEB calculations for Cu-hops as described for Li-hops in chapter 5. The super cell consisted of 16 TiS_2 formula units. A Cu atom hops from one tetrahedral site to its nearest neighbor tetrahedral vacancy straight through the intermediate octahedral site. The energy paths along the hops at different Cu-concentrations are shown in fig 6.2. We have looked into the hops at two extreme concentrations: a single Cu and a single vacancy in the super cell along with two other intermediate compositions. In all these cases, the intermediate octahedral site is always a saddle point rather than a local minimum. This behavior is similar to the Li-diffusion in the α-phase of $Li_{1+x}Ti_2O_4$ (fig 4.6(b)). Also, we observe that the migration barriers associated with these hops are significantly higher compared to Li-hops (vide fig. 5.2(d)) and this high value (~935 meV) is almost invariant to the change in compositions and configuration of surrounding interstitial sites. The slight variation of the migration barrier (~50 meV range) can be attributed to the volume expansion of the host lattice with Cu-intercalation, shown by the lattice constant variation plot in fig 6.3.
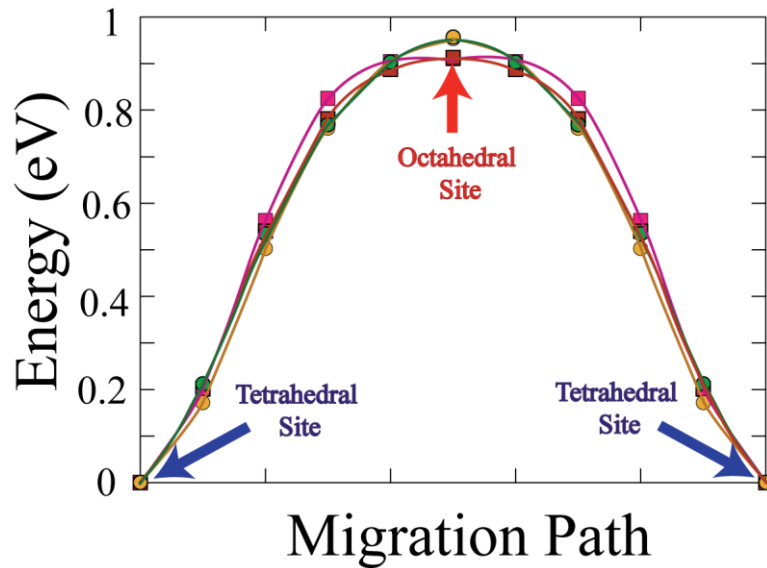
FIG 6.2: Migration energies for the nearest neighbor Cu-hop at different Cu concentrations. The end states are tetrahedral sites. The images for the NEB calculation are placed at equal distances along the straight line path joining the end states.
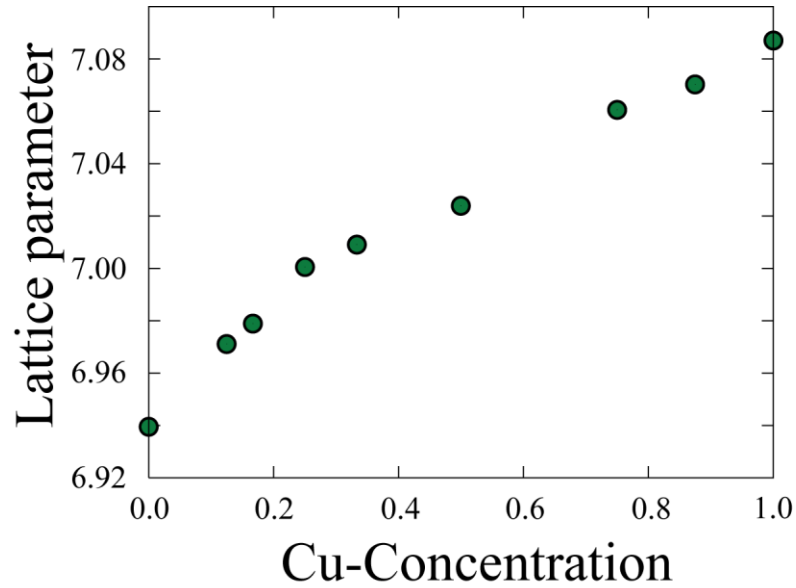
FIG 6.3: Variation of equilibrium lattice parameter of $Cu_xTi_2S_4$ with change in x.

6.2.3 Diffusion behavior of Cu

The cluster expansion described in section 6.2.1 was subjected to the kinetic Monte Carlo simulations to elucidate the diffusion behavior of Cu. In the grand canonical Monte Carlo simulations, we calculated the thermodynamic factor (fig 6.4(a)) as a function of Cu composition, which is an essential quantity in calculating the chemical diffusion coefficient. Here we note the similarity between the thermodynamic factor plots for Li- and Cu-intercalation in the spinel host. (fig 5.5(a) and fig 6.4(a)). This similarity of shape corresponds to the fact that both Li-TiS$_2$ and Cu-TiS2 pairs form solid solutions.
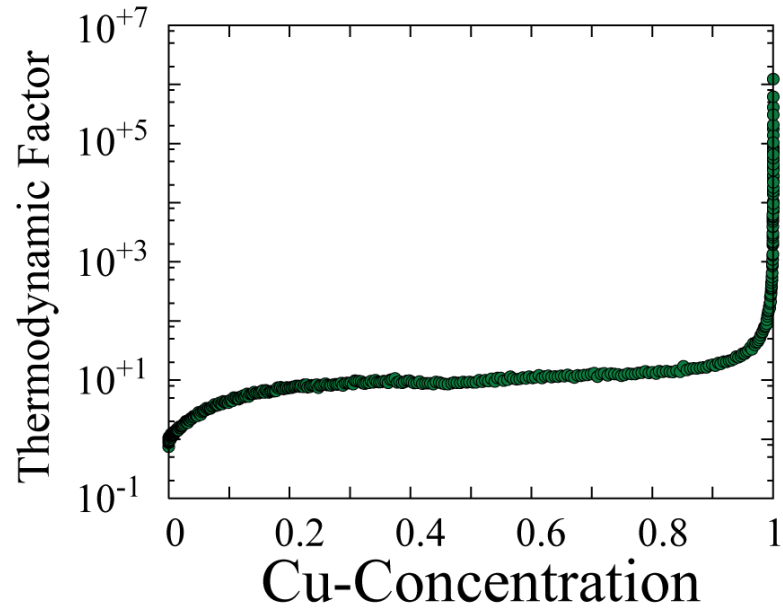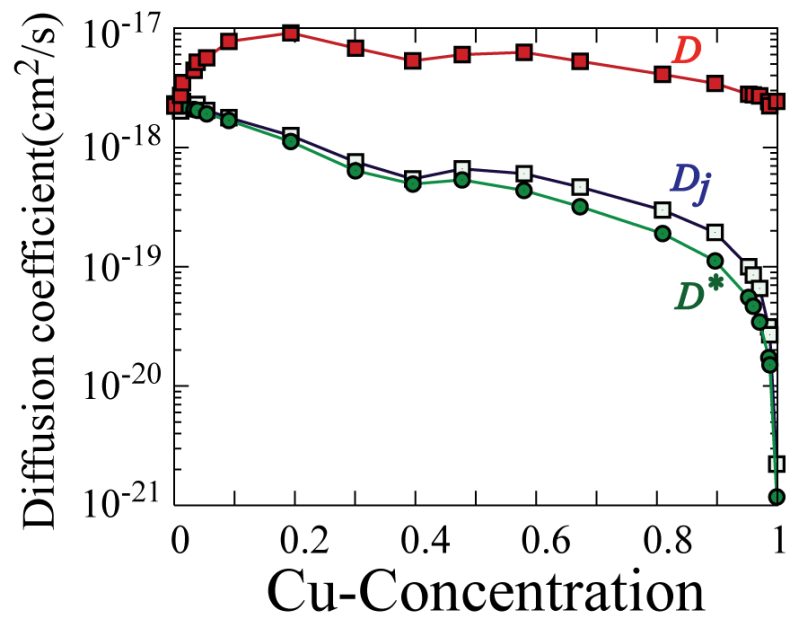
FIG 6.4: (a) Variation of thermodynamic factor with copper concentration. (b) Variation of diffusion metrics as functions of copper concentration. The filled green circles, the hollow squares and the filled red squares represent tracer diffusion coefficient, self diffusion coefficient and chemical diffusion coefficient, respectively.

In the kinetic Monte Carlo simulation, we used the cluster expansion to extrapolate the stable state energies for the system and associate a fixed KRA value (935 meV) to all Cu hops. 1000 Monte Carlo passes were allowed for equilibration and 2000 passes were used for averaging. The final averaging was done over 100 starting ensembles corresponding to each concentration. A constant vibrational prefactor of 1.0×10^{13} was used for the whole composition range. Fig 6.4(b) shows different diffusion metrics for Cu. The curve with the filled squares represents the tracer diffusion coefficient and the curve with hollow circles represents the jump diffusion coefficient. D_J is always greater than D^*. Variation in both D_J and D^* does not depend on the variation of the migration barrier with concentration due to the invariance of the migration barrier. Diffusion mediating vacancies become more and more rare as Cu concentration increases. This makes both D^* and D_J to drop with Cu-concentration and this drop is 3 orders of magnitude over the whole composition range. The high value of migration barrier, causes Cu diffusion to be very slow in sulfide spinel. The product of D_J and Θ represents the chemical diffusion coefficient and it is shown by the filled red squares in fig 6.4(b). The increasing Θ with the increasing Cu concentration, makes D to be almost constant over the concentration range varying only within a single order of magnitude. If we compare the values of diffusion coefficients for Li- and Cu-diffusion, we notice almost seven orders of magnitude difference on average. Therefore, for the titanium sulfide host, Li-diffusion is almost instantaneous compared to Cu-diffusion.

This large difference in Li- and Cu-diffusion rates results in completely different voltage curves during charge and discharge processes in $CuTi_2S_4$ electrodes. During discharge, Li-ions are inserted in the electrode while Cu-ions are extruded to make room for the Li-ions. The process follows the equilibrium path on the phase plane that represents the equilibrium among three phases, $CuTi_2S_4$, $LiTiS_2$ and metallic Cu. The rate of discharge depends critically on the Cu-diffusion as the slowest sub-process determines the process-rate. The charging process is distinctly segregated into two processes: (i) Li-ions are extruded form the host crystal (ii) Cu-ions are reinserted into the host from the metallic Cu-beads. The voltage curve reflects only the first process and hence it follows the equilibrium path between two phases: vacant host of TiS_2 and lithiated host $LiTiS_2$.

Therefore, the enormous hysteresis of the displacement reaction has its origin in the large difference in diffusion rates for the two species.

6.3 Conclusion

The study of Cu-diffusion in TiS_2-spinel host illustrates the effect of guest species on both electrochemistry and diffusion process. This adds another axis to the axes of comparison based on the crystal structure and anion species. The large difference in diffusivities of Cu and Li explains the different voltage curves for the charging and discharging process and the large hysteresis associated with the displacement reaction in $CuTi_2S_4$.

Chapter 7

Conclusions

In the present thesis, we have investigated the thermally and chemically activated phase transitions and diffusion of guest species in crystalline solids from the first principles. In chapter 1, we have reviewed the general ideas and classifications of phase transitions and the factors influencing them. The two types of phase transitions, structural and redistributional, were introduced with examples. Thermally activated structural phase transition was categorized with respect to the physical processes involved. Redistributional phase changes were discussed in the context of Li-ion battery electrodes because of their technological importance. Along with the equilibrium properties, the importance of understanding the kinetics of the transport of guest species in the electrodes was emphasized.

In the second chapter, the details of methodology were reviewed and presented in a concise form. First of all, we presented the role of statistical thermodynamics in relating the zero-Kelvin ab-initio total energies to the moderate temperature macroscopic equilibrium and kinetic properties. The essential input to the statistical mechanical calculations is an effective Hamiltonian. The effective Hamiltonians can evaluate the energies of a large number of microstates while they are constructed from a finite number of ab-initio energies. The construction of the effective Hamiltonians for the relevant degrees of freedom was discussed in this chapter. The principles and methods for the first principles calculations were summarized. The principle of cluster expansion technique for the construction of the redistributional Hamiltonians and relevant algorithms for statistical mechanical calculations were then presented. At the end of this chapter, it was discussed how the macroscopic diffusion process can be formulated from the atomic

scale fluctuations though the principles of irreversible thermodynamics and transition state theory.

In chapter 3, a thermally activated structural phase transition was elucidated at the fundamental level. We examined a particular example of cubic to tetragonal phase transition in stoichiometric TiH_2 where the high temperature cubic phase was mechanically unstable at zero Kelvin. An anharmonic strain Hamiltonian was formulated including the symmetry associated with the cubic to tetragonal transformation. The parameterization of the Hamiltonian relied upon the first principles total energy calculations of a number of deformed structures (with respect to the reference cubic structure) under homogeneous and local strains. The effective Hamiltonian was able to reproduce the basic features of the energy landscape relevant to the cubic to tetragonal phase transition. Moderate to high temperature equilibrium behavior of the system was investigated with Monte Carlo simulations. The inclusion of anharmonic terms in the effective Hamiltonian could explain the high temperature cubic phase even when it is not mechanically stable at zero Kelvin. Non-zero absolute value of the order parameter of the transition revealed the true nature of the high temperature cubic phase. The experimentally observed cubic phase is essentially spatial and temporal average of the tetragonal variants. The discrepancy in the predicted transition temperature was attributed to some mismatch between the experimentally observed degree of tetragonality and as calculated from the first principles. The quantitative accuracy could be improved with temperature dependent expansion coefficients. However, the key issuess in this study were: (i) the role of anharmonic terms in the strain Hamiltonians in explaining the existence of mechanically unstable high symmetry phase at higher temperature and (ii) the true nature of the high temperature high symmetry phase. Both of these were elucidated in this chapter.

In chapter 4, we comprehensively studied thermodynamic and kinetic properties of lithium titanate spinel as an electrode material in Li-ion batteries. The chosen material represents a class of electrode materials with spinel crystal structure with favorable diffusion behavior. The most prominent member of this class is the manganese spinel

($Li_xMn_2O_4$). However, intercalation and diffusion process in manganese spinel is associated with complex charge and magnetic ordering. Titanium spinel offers no such electronic complexity and hence ideal for studying the effect of crystal structure in Li-intercalation process. The three dimensional network of interstitial lithium sites allow us to understand the effect of dimensionality on diffusion process. In $Li_{1+x}Ti_2O_4$, there are two symmetrically distinguishable interstitial sites: tetrahedral and octahedral. From the first-principles calculation of total energies for several lithium-vacancy orderings over these interstitial sites, it was observed that tetrahedral sites are preferred at low lithium concentration and the octahedral sites are preferred at the lithiated limit. In the low-concentration α-phase (tetrahedrally occupied), lithium ions form a solid solution with the titanate host. In the voltage curve, we observe a smooth variation. The fully lithiated β-phase has all the available octahedral sites occupied by Li-ions. There is a miscibility gap between these two distinct phases between $x = 0$ and $x = 1$ in $Li_{1+x}Ti_2O_4$. The calculated voltage curve matches remarkably with the experimental evidence in shape, step size and range of voltages. The equilibrium behavior of $Li_{1+x}Ti_2O_4$ with change in x was investigated at different temperatures. Using free-energy integration technique, a temperature-concentration phase diagram was constructed. The phase diagram illustrates that the miscibility gap between α- and β-phase exists up to high temperature where it narrows down until above 1500 K, everything becomes completely disordered.

The major focus of chapter 4 was the study of the diffusion behavior of lithium ions in Ti_2O_4-host structure. In the α- phase, the nearest neighbor migration paths are straight line paths and the migration energy has a decreasing trend with lithium concentration. From the migration barrier plots we observe that the intermediated octahedral sites are never a local minimum as assumed in the previous studies of diffusion in spinel structures. In the β-phase, diffusion mechanisms change completely with the change in the site preference. The lowest energy nearest neighbor atomic path between two octahedral sites is curvilinear and the intermediate tetrahedral site is a local minima. The migration barrier is very sensitive to the immediate local environment and two hop mechanisms compete in the β-phase: (i) single vacancy and (ii) divacancy. The single

vacancy mechanism is associated with a higher migration barrier. However single vacancies are more abundant compared to the pair of vacancies in stoichiometric β-hase. It was observed that because of this abundance, the single vacancy mechanism dominates substantially in the diffusion process in the β-phase. In the α-phase, decreasing trend of migration barrier with lithium concentration is reflected in the increasing trend of self- and tracer-diffusion coefficients. Near the stoichiometric α-phase, diffusion mediating vacancies become rare and that causes drop in the diffusion metrics. The product of self-diffusion coefficient and the thermodynamic factor results in the chemical diffusion coefficients. The diffusion coefficients are significantly larger compared to the layered intercalation compounds while the migration barriers are in the similar range. This proved the three dimensional diffusion (in spinel) is more efficient than the two-dimensional diffusion (in layered materials).

The study of non-dilute Li diffusion in titanate spinel elucidated some fundamental aspects of diffusion in the intercalation compounds. The effect of dimensionality and the difference in diffusion mediating defects were demonstrated. The thermodynamic behavior of $Li_{1+x}Ti_2O_4$ established it as an efficient candidate anode material with reversible electrochemical behavior and negligible misfit strain with lithium insertion. Favorable diffusion behavior makes it attractive for the high rate applications.

In chapter 5, the diffusion process in titanium sulfide spinel was examined. Titanium sulfide spinel is iso-structural with titanate spinel. The change in anion causes the site preference to change. For the titanium sulfide, the octahedral sites are the preferred sites for the lithium intercalation for the whole concentration range. Any nearest neighbor lithium hop passes through the intermediate tetrahedral site and hence the hop is curvilinear. Unlike titanate spinel, an octahedral lithium is energetically stable even with the three vacant octahedral nearest neighbors. We identified the three possible mechanisms of diffusion: single-, di- and triple-vacancy mechanisms. The migration barriers for these mechanisms have a decreasing trend with the increase in the number of surrounding vacancies. The relative abundance of the three possible environments was tracked in the grand canonical Monte Carlo simulations. In the kinetic Monte Carlo, we

studied the average fraction of three different hops chosen by the migrating lithium ions. The interplay between the opposite trends of two contributing factors, the relative abundance and the associated migration barrier, determines the fraction of the different hops to change with concentrations and leads to a very significant design insight. From the previous studies on layered intercalation compounds (with two-dimensional diffusion), the di-vacancy mechanism dominates in the diffusion process substantially during the entire process of lithium intercalation. The abundance and migration barrier associated with these di-vacancies critically control the kinetics. In case of olivines where diffusion occurs through one dimensional channels, again a single mechanism is important and hence controls the rate. In the case of three dimensional diffusion such as in spinel, there are more than one mechanisms that play crucial role in the diffusion kinetics. In case of the octahedral phase (β) of titanate spinel, there are two available mechanisms (single- and di-vacancy). In the case of the titanium sulfide spinel, three mechanisms are available to the migrating lithium ions and they play significant roles in different concentration regimes. The more the number of available mechanisms, the more efficient the kinetics.

Moreover, this study on titanium sulfide spinel emphasizes another aspect: the coordination of the intermediate site of a hop renders the kinetics more efficient. The intermediate tetrahedral site of a hop in Li_xTiS_2 is coordinated to four nearest neighbor octahedral sites. This multiple coordination results in multiple mechanisms and hence a better kinetics. This observation provides key insight for the future design of the fast diffusing materials, not only for the Li-ion battery electrodes, but also for any other diffusion dominated system.

In chapter 6, we have investigated copper diffusion in titanium sulfide spinel. This study helped us to understand the effect of the guest species on the diffusion process. It has broader significance as in $CuTi_2S_4$ electrode, displacement reaction occurs where lithium ions replaces copper ions during discharging and copper comes out on the surface as metallic Cu-beads. During the charging of the cell, lithium ions get removed from the electrode while copper ions reoccupy the interstitial sites of the TiS_2-spinel host structure.

To understand this displacement reaction, it is essential to study Cu-diffusion in TiS$_2$-spinel. Fully relaxed DFT calculations of Cu-vacancy orderings over the interstitial sites revealed that the tetrahedral sites are preferred by the Cu-ions. The NEB calculations of the nearest neighbor Cu-hops between two tetrahedral sites illustrate that the octahedral sites are not only high energy but also energetically unstable sites. The site preference does not alter with Cu-concentration (between Ti$_2$S$_4$ and CuTi$_2$S$_4$). The chemical potential curve as a function of Cu concentration showed the solid solution like behavior without any preferred ordering between Cu-ions and the vacancies over the interstitial sites. The migration barrier for the nearest neighbor Cu-hops has insignificant variation with Cu concentration or number of available vacancies in the local surroundings (unlike Li-hops). The migration barriers are much higher compared to that for the Li-hops. The slight variation of the migration barrier values were due to the change in lattice parameter with Cu concentration. The invariance of migration barrier with concentration results in the defect-concentration (availability of vacancies) having a very significant role in controlling the kinetics. We observed three orders of magnitude drop in self-diffusion coefficient value in the relevant concentration window of Cu. Near stoichiometric phase, thermodynamic factor diverges rapidly to high values and this stabilizes the chemical diffusion coefficient to have almost a constant value for the whole concentration range. The chemical diffusion coefficient has a value, seven orders of magnitude less on average than that for Li-diffusion. Therefore, compared to Cu-diffusion, Li-diffusion is practically instantaneous. The large difference in diffusivities of two species in TiS$_2$ spinel host has significant implications in the reversibility of the displacement reaction. During discharging, Li-ions move into the host, Cu-ions move out at the same time, the whole process follows the equilibrium path on the phase plane in equilibrium with the metallic copper. However, the charging process does not retract this path reversibly. Li-ions quickly move out of the host structure and subsequently Cu-ions slowly move into it. Hence, the charging curve follows the equilibrium path between Li$_2$Ti$_2$S$_4$ and Ti$_2$S$_4$. This difference in charge-discharge curves results in enormous hysteresis and it is governed by the kinetics of the two species diffusing in the same host crystal.

We have used a thorough theoretical and computational framework for elucidating the structural and redistributional phase transformations and interstitial diffusion in crystalline solids. An example of the thermally activated tetragonal to cubic phase transition was looked into in detail. The vital role of the anharmonic terms in the strain Hamiltonians in modeling of these transitions was illustrated. We explained the stability of the high temperature phase while it is mechanically unstable at zero Kelvin through the statistical mechanical calculations on the anharmonic strain Hamiltonian. The true nature of the high temperature and high symmetry phase was also shown to have changed the conventional understanding. The redistributional phase transformations were demonstrated with the intercalation process in the technologically attractive Li-ion battery electrodes. The thesis systematically uses a detailed procedure for understanding the macroscopic thermodynamics and the diffusion kinetics in the intercalation compounds in the Li-ion battery electrodes. Dependence of the equilibrium and diffusion behavior, on crystal structure, choice of anion and the diffusing species were illustrated through three chapters. The reasons behind efficient kinetic behavior in materials with three dimensional diffusion paths were explained. The present thesis explains previous observations, provides fundamental insights, and inspires future endeavors in the area of computational material modeling.

Appendix A

Frequency map for vibrational microstates

In Monte Carlo simulations, we can track different strain metrics associated with each vibrational excitations. The sampling frequency depends on the atomic scale energy landscape. The excitations causing low energy states are sampled more frequently and the high energy excitations are rarely sampled. With increase in temperature, increased thermal energy allows the system to sample higher energy excitations more frequently. Therefore the temperature dependence of sampling frequencies illustrates the fundamental nature of the temperature dependent structural phase transitions.

In case of cubic to tetragonal phase transformation, variables e_2 and e_3 are the relevant metrics to track the transformation. Moreover, focus on two independent strain metrics allow us to plot the frequencies in a three dimensional plot. In Monte Carlo simulation, we measure all strain metrics for each accepted excitation for a lattice site. On an e_2-e_3 grid, the number of attempt is incremented if the deviatoric strain metrics fall in a particular e_2-e_3 interval. The total number of successful attempts for each grid-cell is normalized by the number of sites in the simulation cell and the number of Monte Carlo passes. This normalized attempt count represents the relative sampling frequency in e_2-e_3 space.

Fig A.1 illustrates the relative frequency map for low temperature (100 K). In fig A.1(a), the three dimensional plot is shown where frequencies are plotted as the height above the e_2-e_3 plane and in fig A.1(b), the same plot is shown as the top-view to highlight the location of sampling peak on the e_2-e_3 plane. At low temperature, the initial ground state was chosen to be the tetragonal variant with z-axis compression. This tetragonal distortion is represented by the point on e_3 axis. Fig A.1(b) shows that the all the high frequency distortions are around this tetragonal ground state.
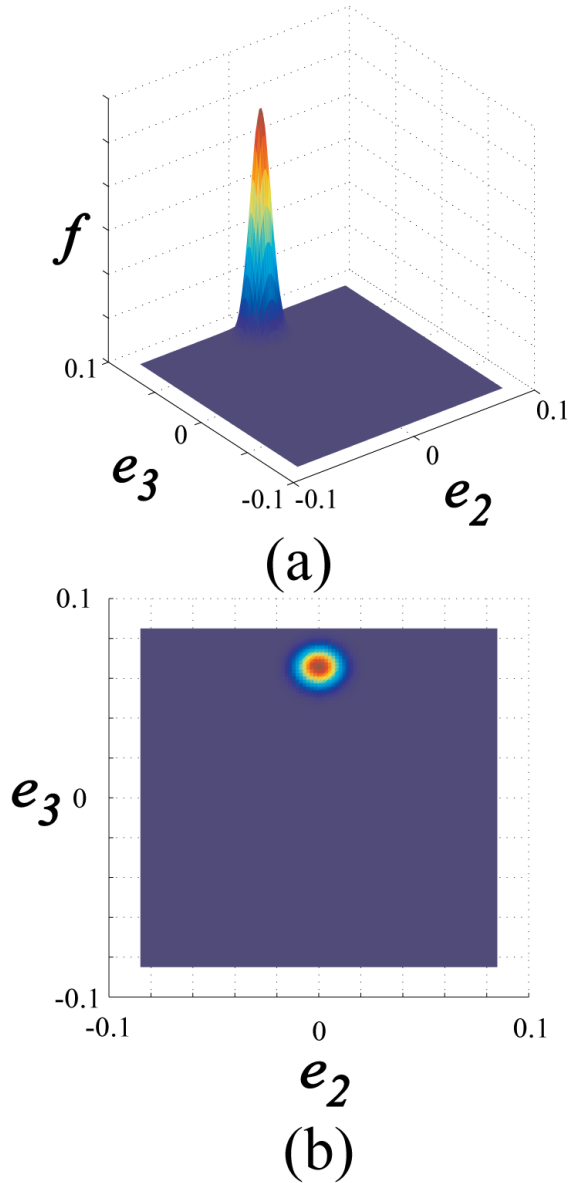
FIG A.1: Frequency map at low temperature (100 K) (a) Three dimension view of frequency map where frequencies are plotted as heights from the e_2-e_3 plane (b) two dimensional top-view of the frequency map where the position of high frequency points are located on the e_2-e_3 plane.

In fig A.2 similar frequencies were plotted above the transition temperature where cubic phase is observed. Here we observe, similar bell-shaped frequency landscape. However, the bell spans a wider region in e_2-e_3 plane and it is centered around the origin, which represents the cubic phase.
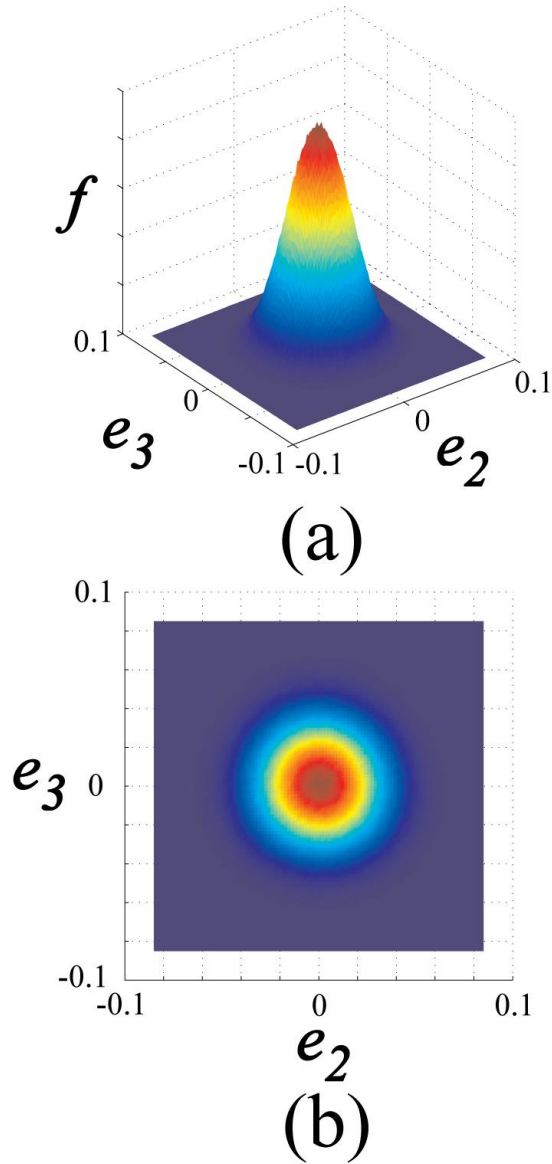
FIG A.2: Frequency map at high temperature (700 K) (a) Three dimension view of frequency map where frequencies are plotted as heights from the e_2-e_3 plane (b) two dimensional top-view of the frequency map where the position of high frequency points are located on the e_2-e_3 plane.

Above the transition temperature, shape of the frequency map has circular symmetry around the origin and hence on average the phase resembles the pure cubic phase. The wide span of the bell shaped curve indicates that the thermal energy of the system is high enough to sample microstates corresponding to large deviatoric strains. Absence of three

local minima corresponding to the three equivalent tetragonal variants in the frequency plot illustrates that the description of the high temperature cubic phase as the average of three tetragonal variants is over simplified. The energy landscape is much more complex than that shown in fig 3.3. The energy contour plot in fig 3.3 shows the energy landscape under homogeneous deviatoric strains only. It does not account for the local strains that include dilation and shear components. In Monte Carlo simulation, though, the energy penalties due to other strain components are accurately accounted for and the frequency map on the e_2-e_3 plane demonstrates the true nature of the high temperature cubic phase. In reality, the thermal energy of the system is so high above the transition temperature that it cannot see the local tetragonal wells. Hence it samples all kinds of excitations around the cubic phase with circular symmetry without being restricted to the tetragonal energy wells.

Bibliography

1. Parr, R.G. and W. Yang, *Density-functional theory of atoms and molecules*. International series of monographs on chemistry. 1989, New York: Oxford University Press ; Clarendon Press. ix, 333 p.
2. Koch, W. and M.C. Holthausen, *A chemist's guide to density functional theory*. 2001, Weinheim: Wiley-VCH. xiii, 300 p.
3. Szabo, A. and N.S. Ostlund, *Modern quantum chemistry: introduction to advanced electronic structure theory*. 1982, New York: Free Press ; Collier Macmillan. xvi, 446 p.
4. Kohn, W., A.D. Becke, and R.G. Parr, *Density functional theory of electronic structure.* Journal of Physical Chemistry, 1996. **100**(31): p. 12974-12980.
5. Shankar, R., *Principles of quantum mechanics*. 1980, New York: Plenum Press. xviii, 612 p.
6. McQuarrie, D.A., *Statistical thermodynamics*. 1973, Mill Valley, Calif.: University Science Books. xi, 343 p.
7. Pathria, R.K., *Statistical mechanics*. International series of monographs in natural philosophy. 1993, Oxford: Pergamon Press. xiii, 529 p.
8. Binder, K. and D.W. Heermann, *Monte Carlo simulation in statistical physics: an introduction*. Springer series in solid-state sciences. 1988, Berlin: Springer-Verlag. viii, 127 p.
9. Rice, O.K., *Statistical mechanics, thermodynamics, and kinetics*. A Series of books in chemistry. 1967, San Francisco: W. H. Freeman. vii, 586 p.
10. Reif, F., *Fundamentals of statistical and thermal physics*. McGraw-Hill series in fundamentals of physics. 1965, New York: McGraw-Hill. x, 651 p.
11. Stanley, H.E., *Introduction to phase transitions and critical phenomena*. International series of monographs on physics. 1971, New York: Oxford University Press. xx, 308 p.
12. Yeomans, J.M., *Statistical Mechanics of Phase Transitions.* Oxford Science Publications, 1992.
13. Mazenko, G., *Fluctuations, order, and defects*. 2003, Hoboken, N.J.: Wiley-Interscience. xvi, 673 p.
14. Papon, P., et al., *The Physics of Phase Transitions Concepts and Applications*. 2006, Berlin Heidelberg: Springer-Verlag GmbH.
15. Krauss, G., *Steels: heat treatment and processing principles*. 1990, Materials Park, Ohio: ASM International. xvi, 497 p.
16. Rosenberg, S.J. and T.G. Digges, *Heat treatment and properties of iron and steel*. [U.S.] National Bureau of Standards. 1960, Washington: U. S. Govt. Print. Off. 40 p.
17. Funakubo, H., *Shape memory alloys*. Precision machinery and robotics. 1987, New York: Gordon and Breach Science Publishers. xii, 275 p.
18. Duerig, T.W., *Engineering aspects of shape memory alloys*. 1990, London: Butterworth-Heinemann. xi, 499 p.
19. Fremond, M., S. Miyazaki, and S. International Centre for Mechanical, *Shape memory alloys / M. Fremond, S. Miyazaki*. CISM courses and lectures. 1996, Wien: Springer. 147 p.
20. Linden, D. and T.B. Reddy, *Handbook of batteries*. McGraw-Hill handbooks. 2002, New York: McGraw-Hill. 1 v. (various pagings).
21. Tarascon, J.M. and M. Armand, *Issues and challenges facing rechargeable lithium batteries.* Nature, 2001. **414**(6861): p. 359-367.

22.   Fujimoto, M., *The physics of structural phase transitions*. 1997, New York: Springer. xi, 247 p.

23.   Christian, J.W., *The theory of transformations in metals and alloys: an advanced textbook in physical metallurgy*. International series of monographs in metal physics and physical metallurgy. 1965, Oxford: Pergamon Press. xvi, 973 p.

24.   Khachaturii︠a︡︠n, A.G., *Theory of structural transformations in solids*. 1983, New York: Wiley. xiii, 574 p.

25.   Frey, M.H. and D.A. Payne, *Grain-size effect on structure and phase transformations for barium titanate*. Physical Review B, 1996. **54**(5): p. 3158-3168.

26.   Lemanov, V.V., et al., *Phase transitions and glasslike behavior in Sr1-xBaxTiO3*. Physical Review B, 1996. **54**(5): p. 3151-3157.

27.   Padilla, J. and D. Vanderbilt, *Ab initio study of BaTiO3 surfaces*. Physical Review B, 1997. **56**(3): p. 1625-1631.

28.   Bhattacharya, K., *WEDGE-LIKE MICROSTRUCTURE IN MARTENSITES*. Acta Metallurgica Et Materialia, 1991. **39**(10): p. 2431-2444.

29.   Hane, K.F. and T.W. Shield, *Symmetry and microstructure in martensites*. Philosophical Magazine a-Physics of Condensed Matter Structure Defects and Mechanical Properties, 1998. **78**(6): p. 1215-1252.

30.   Yashima, M., et al., *DIFFUSIONLESS TETRAGONAL CUBIC TRANSFORMATION TEMPERATURE IN ZIRCONIA CERIA SOLID-SOLUTIONS*. Journal of the American Ceramic Society, 1993. **76**(11): p. 2865-2868.

31.   Wojtowicz, P.J., *THEORETICAL MODEL FOR TETRAGONAL-TO-CUBIC PHASE TRANSFORMATIONS IN TRANSITION METAL SPINELS*. Physical Review, 1959. **116**(1): p. 32-45.

32.   Bowles, J.S., C.S. Barrett, and L. Guttman, *CRYSTALLOGRAPHY OF CUBIC-TETRAGONAL TRANSFORMATION IN THE INDIUM-THALLIUM SYSTEM*. Transactions of the American Institute of Mining and Metallurgical Engineers, 1950. **188**(12): p. 1478-1485.

33.   Heuer, A.H., R. Chaim, and V. Lanteri, *THE DISPLACIVE CUBIC-]TETRAGONAL TRANSFORMATION IN ZRO2 ALLOYS*. Acta Metallurgica, 1987. **35**(3): p. 661-666.

34.   Glazer, A.M. and H.D. Megaw, *STRUCTURE OF SODIUM NIOBATE (T2) AT 600 DEGREES C, AND CUBIC-TETRAGONAL TRANSITION IN RELATION TO SOFT-PHONON MODES*. Philosophical Magazine, 1972. **25**(5): p. 1119-&.

35.   Ihrig, H., et al., *CUBIC-TO-TETRAGONAL TRANSFORMATION AND SUSCEPTIBILITY IN LAAGXIN1-X ALLOYS*. Physical Review B, 1973. **8**(10): p. 4525-4533.

36.   Salje, E.K.H., et al., *The cubic-tetragonal phase transition in strontium titanate: excess specific heat measurements and evidence for a near-tricritical, mean field type transition mechanism*. Journal of Physics-Condensed Matter, 1998. **10**(25): p. 5535-5543.

37.   Christensen, N.E. and S. Satpathy, *PRESSURE-INDUCED CUBIC TO TETRAGONAL TRANSITION IN CSI*. Physical Review Letters, 1985. **55**(6): p. 600-603.

38.   Onuki, A., *Phase transition dynamics*. 2002, Cambridge: Cambridge University Press. x, 714 p.

39.   Ashcroft, N.W. and N.D. Mermin, *Solid state physics*. 1976, New York: Holt, Rinehart and Winston. xxi, 826 p.

40.   Craievich, P.J., et al., *LOCAL STABILITY OF NONEQUILIBRIUM PHASES*. Physical Review Letters, 1994. **72**(19): p. 3076-3079.

41.   Craievich, P.J., et al., *Structural instabilities of excited phases*. Physical Review B, 1997. **55**(2): p. 787-797.

42.	Persson, K., M. Ekman, and V. Ozolins, *Phonon instabilities in bcc Sc, Ti, La, and Hf.* Physical Review B, 2000. **61**(17): p. 11221-11224.

43.	Whittingham, M.S., *Lithium batteries and cathode materials.* Chemical Reviews, 2004. **104**(10): p. 4271-4301.

44.	Koksbang, R., et al., *Cathode materials for lithium rocking chair batteries.* Solid State Ionics, 1996. **84**(1-2): p. 1-21.

45.	Ozawa, K., *LITHIUM-ION RECHARGEABLE BATTERIES WITH LICOO2 AND CARBON ELECTRODES - THE LICOO2 C SYSTEM.* Solid State Ionics, 1994. **69**(3-4): p. 212-221.

46.	Padhi, A.K., K.S. Nanjundaswamy, and J.B. Goodenough, *Phospho-olivines as positive-electrode materials for rechargeable lithium batteries.* Journal of the Electrochemical Society, 1997. **144**(4): p. 1188-1194.

47.	Tarascon, J.M. and D. Guyomard, *THE LI1+XMN2O4/C ROCKING-CHAIR SYSTEM - A REVIEW.* Electrochimica Acta, 1993. **38**(9): p. 1221-1231.

48.	Thackeray, M.M., et al., *SPINEL ELECTRODES FROM THE LI-MN-O SYSTEM FOR RECHARGEABLE LITHIUM BATTERY APPLICATIONS.* Journal of the Electrochemical Society, 1992. **139**(2): p. 363-366.

49.	Chusid, O., et al., *ELECTROCHEMICAL AND SPECTROSCOPIC STUDIES OF CARBON ELECTRODES IN LITHIUM BATTERY ELECTROLYTE SYSTEMS.* Journal of Power Sources, 1993. **43**(1-3): p. 47-64.

50.	Endo, M., et al., *Recent development of carbon materials for Li ion batteries.* Carbon, 2000. **38**(2): p. 183-197.

51.	Basu, S., *Early studies on anodic properties of lithium intercalated graphite.* Journal of Power Sources, 1999. **81**: p. 200-206.

52.	Yazami, R. and P. Touzain, *A REVERSIBLE GRAPHITE LITHIUM NEGATIVE ELECTRODE FOR ELECTROCHEMICAL GENERATORS.* Journal of Power Sources, 1983. **9**(3-4): p. 365-371.

53.	Whittingham, M.S., *ELECTRICAL ENERGY-STORAGE AND INTERCALATION CHEMISTRY.* Science, 1976. **192**(4244): p. 1126-1127.

54.	Whittingham, M.S., *CHEMISTRY OF INTERCALATION COMPOUNDS - METAL GUESTS IN CHALCOGENIDE HOSTS.* Progress in Solid State Chemistry, 1978. **12**(1): p. 41-99.

55.	Whittingham, M.S. and F.R. Gamble, *LITHIUM INTERCALATES OF TRANSITION-METAL DICHALCOGENIDES.* Materials Research Bulletin, 1975. **10**(5): p. 363-371.

56.	Van der Ven, A., et al., *Nondilute diffusion from first principles: Li diffusion in LixTiS2.* Physical Review B, 2008. **78**(10).

57.	Whittingham, M.S., *STORING ENERGY BY INTERCALATION.* Chemtech, 1979. **9**(12): p. 766-770.

58.	Holleck, G.L. and J.R. Driscoll, *TRANSITION-METAL SULFIDES AS CATHODES FOR SECONDARY LITHIUM BATTERIES .2. TITANIUM SULFIDES.* Electrochimica Acta, 1977. **22**(6): p. 647-655.

59.	Mizushima, K., et al., *LIXCOO2 "(OLESS-THANXLESS-THAN-OR-EQUAL-TO1) - A NEW CATHODE MATERIAL FOR BATTERIES OF HIGH-ENERGY DENSITY.* Materials Research Bulletin, 1980. **15**(6): p. 783-789.

60.	Thackeray, M.M., *Manganese oxides for lithium batteries.* Progress in Solid State Chemistry, 1997. **25**(1-2): p. 1-71.

61.	Thackeray, M.M., *STRUCTURAL CONSIDERATIONS OF LAYERED AND SPINEL LITHIATED OXIDES FOR LITHIUM ION BATTERIES.* Journal of the Electrochemical Society, 1995. **142**(8): p. 2558-2563.

62. Murphy, D.W., et al., *TERNARY LIXTIO2 PHASES FROM INSERTION REACTIONS.* Solid State Ionics, 1983. **9-10**(DEC): p. 413-417.

63. West, K., et al., *VANADIUM-OXIDE XEROGELS AS ELECTRODES FOR LITHIUM BATTERIES.* Electrochimica Acta, 1993. **38**(9): p. 1215-1220.

64. Nordlinder, S., K. Edstrom, and T. Gustafsson, *The performance of vanadium oxide nanorolls as cathode material in a rechargeable lithium battery.* Electrochemical and Solid State Letters, 2001. **4**(8): p. A129-A131.

65. Kanno, R., et al., *Synthesis, structure, and electrochemical properties of a new lithium iron oxide, LiFeO2, with a corrugated layer structure.* Journal of the Electrochemical Society, 1996. **143**(8): p. 2435-2442.

66. Delmas, C. and I. Saadoune, *ELECTROCHEMICAL AND PHYSICAL-PROPERTIES OF THE LIXNI1-YCOYO2 PHASES.* Solid State Ionics, 1992. **53**: p. 370-375.

67. Zhecheva, E. and R. Stoyanova, *STABILIZATION OF THE LAYERED CRYSTAL-STRUCTURE OF LINIO2 BY CO-SUBSTITUTION.* Solid State Ionics, 1993. **66**(1-2): p. 143-149.

68. Ohzuku, T. and Y. Makimura, *Layered lithium insertion material of LiNi1/2Mn1/2O2: A possible alternative to LiCoO2 for advanced lithium-ion batteries.* Chemistry Letters, 2001(8): p. 744-745.

69. Morgan, D., A. Van der Ven, and G. Ceder, *Li conductivity in LixMPO4 (M = Mn, Fe, Co, Ni) olivine materials.* Electrochemical and Solid State Letters, 2004. **7**(2): p. A30-A32.

70. Van der Ven, A., et al., *First-principles theory of ionic diffusion with nondilute carriers.* Physical Review B, 2001. **64**(18).

71. Ceder, G., *A derivation of the Ising model for the computation of phase diagrams.* Computational Materials Science, 1993. **1**(2): p. 144-150.

72. Ziman, J.M., *Electrons and phonons; the theory of transport phenomena in solids.* International series of monographs on physics. 1960, Oxford: Clarendon Press. 554 p.

73. Slater, J.C., *Quantum theory of matter.* International series in pure and applied physics. 1968, New York: McGraw-Hill. 763 p.

74. Park, D.A., *Introduction to the quantum theory.* 1964, New York: McGraw-Hill. xv, 547 p.

75. Ziock, K., *Basic quantum mechanics.* 1969, New York: Wiley. xiii, 271 p.

76. Madelung, O., *Introduction to solid-state theory.* Springer series in solid-state sciences. 1978, Berlin: Springer-Verlag. xi, 486 p.

77. Hohenberg, P. and W. Kohn, *INHOMOGENEOUS ELECTRON GAS.* Physical Review B, 1964. **136**(3B): p. B864-&.

78. Kohn, W. and L.J. Sham, *SELF-CONSISTENT EQUATIONS INCLUDING EXCHANGE AND CORRELATION EFFECTS.* Physical Review, 1965. **140**(4A): p. 1133-&.

79. Ceperley, D.M. and B.J. Alder, *GROUND-STATE OF THE ELECTRON-GAS BY A STOCHASTIC METHOD.* Physical Review Letters, 1980. **45**(7): p. 566-569.

80. Perdew, J.P., *DENSITY-FUNCTIONAL APPROXIMATION FOR THE CORRELATION-ENERGY OF THE INHOMOGENEOUS ELECTRON-GAS.* Physical Review B, 1986. **33**(12): p. 8822-8824.

81. Perdew, J.P. and W. Yue, *ACCURATE AND SIMPLE DENSITY FUNCTIONAL FOR THE ELECTRONIC EXCHANGE ENERGY - GENERALIZED GRADIENT APPROXIMATION.* Physical Review B, 1986. **33**(12): p. 8800-8802.

82. Perdew, J.P., K. Burke, and M. Ernzerhof, *Generalized gradient approximation made simple.* Physical Review Letters, 1996. **77**(18): p. 3865-3868.

83. Phillips, J.C. and L. Kleinman, *NEW METHOD FOR CALCULATING WAVE FUNCTIONS IN CRYSTALS AND MOLECULES.* Physical Review, 1959. **116**(2): p. 287-294.

84. Payne, M.C., et al., *ITERATIVE MINIMIZATION TECHNIQUES FOR ABINITIO TOTAL-ENERGY CALCULATIONS - MOLECULAR-DYNAMICS AND CONJUGATE GRADIENTS.* Reviews of Modern Physics, 1992. **64**(4): p. 1045-1097.

85. Blochl, P.E., *PROJECTOR AUGMENTED-WAVE METHOD.* Physical Review B, 1994. **50**(24): p. 17953-17979.

86. Kresse, G. and J. Furthmuller, *Efficient iterative schemes for ab initio total-energy calculations using a plane-wave basis set.* Physical Review B, 1996. **54**(16): p. 11169-11186.

87. Kresse, G. and J. Furthmuller, *Efficiency of ab-initio total energy calculations for metals and semiconductors using a plane-wave basis set.* Computational Materials Science, 1996. **6**(1): p. 15-50.

88. Kresse, G. and D. Joubert, *From ultrasoft pseudopotentials to the projector augmented-wave method.* Physical Review B, 1999. **59**(3): p. 1758-1775.

89. Sanchez, J.M., F. Ducastelle, and D. Gratias, *GENERALIZED CLUSTER DESCRIPTION OF MULTICOMPONENT SYSTEMS.* Physica A, 1984. **128**(1-2): p. 334-350.

90. deFontaine, D., *Cluster approach to order-disorder transformations in alloys*, in *Solid State Physics - Advances in Research and Applications, Vol 47*. 1994, Academic Press Inc: San Diego. p. 33-176.

91. van de Walle, A. and G. Ceder, *Automating first-principles phase diagram calculations.* Journal of Phase Equilibria, 2002. **23**(4): p. 348-359.

92. Hart, G.L.W., et al., *Evolutionary approach for determining first-principles hamiltonians.* Nature Materials, 2005. **4**(5): p. 391-394.

93. Fishman, G.S., *Monte Carlo: concepts, algorithms, and applications*. Springer series in operations research. 1996, New York: Springer-Verlag. xxv, 698 p.

94. SobolÊ¹, I.M., *The Monte Carlo method*. Metod Monte-Karlo. 1975, Moscow: Mir Publishers. 71 p.

95. Madras, N.N. and M. Workshop on Monte Carlo, *Monte Carlo methods*. Fields Institute communications. 2000, Providence, R.I.: American Mathematical Society. viii, 228 p.

96. Robert, C.P. and G. Casella, *Monte Carlo statistical methods*. Springer texts in statistics. 1999, New York: Springer. xxi, 507 p.

97. Metropolis, N., et al., *EQUATION OF STATE CALCULATIONS BY FAST COMPUTING MACHINES.* Journal of Chemical Physics, 1953. **21**(6): p. 1087-1092.

98. Bulnes, F.M., V.D. Pereyra, and J.L. Riccardo, *Collective surface diffusion: n-fold way kinetic Monte Carlo simulation.* Physical Review E, 1998. **58**(1): p. 86-92.

99. Gomer, R., *DIFFUSION OF ADSORBATES ON METAL-SURFACES.* Reports on Progress in Physics, 1990. **53**(7): p. 917-1002.

100. Richards, P.M., *THEORY OF ONE-DIMENSIONAL HOPPING CONDUCTIVITY AND DIFFUSION.* Physical Review B, 1977. **16**(4): p. 1393-1409.

101. Bortz, A.B., M.H. Kalos, and J.L. Lebowitz, *NEW ALGORITHM FOR MONTE-CARLO SIMULATION OF ISING SPIN SYSTEMS.* Journal of Computational Physics, 1975. **17**(1): p. 10-18.

102. Vineyard, G.H., *FREQUENCY FACTORS AND ISOTOPE EFFECTS IN SOLID STATE RATE PROCESSES.* Journal of Physics and Chemistry of Solids, 1957. **3**(1-2): p. 121-127.

103. van de Walle, A. and G. Ceder, *The effect of lattice vibrations on substitutional alloy thermodynamics.* Reviews of Modern Physics, 2002. **74**(1): p. 11-45.

104. Zhong, W., D. Vanderbilt, and K.M. Rabe, *FIRST-PRINCIPLES THEORY OF FERROELECTRIC PHASE-TRANSITIONS FOR PEROVSKITES - THE CASE OF BATIO3*. Physical Review B, 1995. **52**(9): p. 6301-6312.

105. Zhong, W., D. Vanderbilt, and K.M. Rabe, *PHASE-TRANSITIONS IN BATIO3 FROM FIRST PRINCIPLES*. Physical Review Letters, 1994. **73**(13): p. 1861-1864.

106. Waghmare, U.V. and K.M. Rabe, *Ab initio statistical mechanics of the ferroelectric phase transition in PbTiO3*. Physical Review B, 1997. **55**(10): p. 6161-6173.

107. Jomard, G., et al., *First-principles calculations to describe zirconia pseudopolymorphs*. Physical Review B, 1999. **59**(6): p. 4044-4052.

108. Sliwko, V.L., et al., *The fcc-bcc structural transition .1. A band theoretical study for Li, K, Rb, Ca, Sr, and the transition metals Ti and V*. Journal of Physics-Condensed Matter, 1996. **8**(7): p. 799-815.

109. Wang, L.G., M. Sob, and Z.Y. Zhang, *Instability of higher-energy phases in simple and transition metals*. Journal of Physics and Chemistry of Solids, 2003. **64**(5): p. 863-872.

110. Wang, Y., et al., *Ab initio lattice stability in comparison with CALPHAD lattice stability*. Calphad-Computer Coupling of Phase Diagrams and Thermochemistry, 2004. **28**(1): p. 79-90.

111. Yakel, H.L., *THERMOCRYSTALLOGRAPHY OF HIGHER HYDRIDES OF TITANIUM AND ZIRCONIUM*. Acta Crystallographica, 1958. **11**(1): p. 46-51.

112. Gupta, M., *ELECTRONICALLY DRIVEN TETRAGONAL DISTORTION IN TIH2*. Solid State Communications, 1979. **29**(1): p. 47-51.

113. Xu, Q. and A. Van der Ven, *First-principles investigation of metal-hydride phase stability: The Ti-H system*. Physical Review B, 2007. **76**.

114. Barsch, G.R. and J.A. Krumhansl, *TWIN BOUNDARIES IN FERROELASTIC MEDIA WITHOUT INTERFACE DISLOCATIONS*. Physical Review Letters, 1984. **53**(11): p. 1069-1072.

115. Finnis, M.W. and V. Heine, *SIMPLE THEORY OF SOME PHASE-TRANSITIONS*. Journal of Physics F-Metal Physics, 1974. **4**(7): p. 960-968.

116. Rabe, K.M. and U.V. Waghmare, *LOCALIZED BASIS FOR EFFECTIVE LATTICE HAMILTONIANS - LATTICE WANNIER FUNCTIONS*. Physical Review B, 1995. **52**(18): p. 13236-13246.

117. Delmas, C., C. Fouassier, and P. Hagenmuller, *STRUCTURAL CLASSIFICATION AND PROPERTIES OF THE LAYERED OXIDES*. Physica B & C, 1980. **99**(1-4): p. 81-85.

118. Van der Ven, A. and G. Ceder, *Lithium diffusion mechanisms in layered intercalation compounds*. Journal of Power Sources, 2001. **97-8**: p. 529-531.

119. Chen, G.Y., X.Y. Song, and T.J. Richardson, *Electron microscopy study of the LiFePO4 to FePO4 phase transition*. Electrochemical and Solid State Letters, 2006. **9**(6): p. A295-A298.

120. Delmas, C., et al., *Lithium deintercalation in LiFePO4 nanoparticles via a domino-cascade model*. Nature Materials, 2008. **7**(8): p. 665-671.

121. Meethong, N., et al., *Strain accommodation during phase transformations in olivine-based cathodes as a materials selection criterion for high-power rechargeable batteries*. Advanced Functional Materials, 2007. **17**(7): p. 1115-1123.

122. Van der Ven, A., et al., *The Role of Coherency Strains on Phase Stability in LixFePO4: Needle Crystallites Minimize Coherency Strain and Overpotential*. Journal of the Electrochemical Society, 2009. **156**(11): p. A949-A957.

123. Thackeray, M.M., et al., *LITHIUM INSERTION INTO MANGANESE SPINELS*. Materials Research Bulletin, 1983. **18**(4): p. 461-472.

124. Bonino, F., et al., *ANATASE AS A CATHODE MATERIAL IN LITHIUM-ORGANIC ELECTROLYTE RECHARGEABLE BATTERIES.* Journal of Power Sources, 1981. **6**(3): p. 261-270.

125. Ohzuku, T., T. Kodama, and T. Hirai, *ELECTROCHEMISTRY OF ANATASE TITANIUM-DIOXIDE IN LITHIUM NONAQUEOUS CELLS.* Journal of Power Sources, 1985. **14**(1-3): p. 153-166.

126. Cava, R.J., et al., *THE CRYSTAL-STRUCTURES OF THE LITHIUM-INSERTED METAL-OXIDES LI0.5TIO2 ANATASE, LITI2O4 SPINEL, AND LI2TI2O4.* Journal of Solid State Chemistry, 1984. **53**(1): p. 64-75.

127. Colbow, K.M., J.R. Dahn, and R.R. Haering, *STRUCTURE AND ELECTROCHEMISTRY OF THE SPINEL OXIDES LITI2O4 AND LI4/3TI5/3O4.* Journal of Power Sources, 1989. **26**(3-4): p. 397-402.

128. Tarascon, J.M., et al., *THE SPINEL PHASE OF LIMN2O4 AS A CATHODE IN SECONDARY LITHIUM CELLS.* Journal of the Electrochemical Society, 1991. **138**(10): p. 2859-2864.

129. Rodriguez-Carvajal, J., et al., *Electronic crystallization in a lithium battery material: Columnar ordering of electrons and holes in the spinel LiMn2O4.* Physical Review Letters, 1998. **81**(21): p. 4660-4663.

130. Yamada, A. and M. Tanaka, *JAHN-TELLER STRUCTURAL PHASE-TRANSITION AROUND 280K IN LIMN2O4.* Materials Research Bulletin, 1995. **30**(6): p. 715-721.

131. Greedan, J.E., et al., *Structure and magnetism in lambda-MnO2. Geometric frustration in a defect spinel.* Chemistry of Materials, 1998. **10**(10): p. 3058-3067.

132. Greedan, J.E., et al., *Neutron-scattering studies of the geometrically frustrated spinel LiMn2O4.* Physical Review B, 2002. **65**(18).

133. Jang, Y.I., et al., *Magnetic characterization of lambda-MnO2 and Li2Mn2O4 prepared by electrochemical cycling of LiMn2O4.* Journal of Applied Physics, 2000. **87**(10): p. 7382-7388.

134. Wagemaker, M., et al., *Thermodynamics of spinel LixTiO2 from first principles.* Chemical Physics, 2005. **317**(2-3): p. 130-136.

135. Ferg, E., et al., *SPINEL ANODES FOR LITHIUM-ION BATTERIES.* Journal of the Electrochemical Society, 1994. **141**(11): p. L147-L150.

136. Ohzuku, T., A. Ueda, and N. Yamamoto, *ZERO-STRAIN INSERTION MATERIAL OF LI[LI1/3TI5/3]O-4 FOR RECHARGEABLE LITHIUM CELLS.* Journal of the Electrochemical Society, 1995. **142**(5): p. 1431-1435.

137. Zaghib, K., et al., *Electrochemical study of Li4Ti5O12 as negative electrode for Li-ion polymer rechargeable batteries.* Journal of Power Sources, 1999. **81**: p. 300-305.

138. Scharner, S., W. Weppner, and P. Schmid-Beurmann, *Evidence of two-phase formation upon lithium insertion into the Li1.33Ti1.67O4 spinel.* Journal of the Electrochemical Society, 1999. **146**(3): p. 857-861.

139. Arora, P., R.E. White, and M. Doyle, *Capacity fade mechanisms and side reactions in lithium-ion batteries.* Journal of the Electrochemical Society, 1998. **145**(10): p. 3647-3667.

140. Zhang, S.S., et al., *Understanding solid electrolyte interface film formation on graphite electrodes.* Electrochemical and Solid State Letters, 2001. **4**(12): p. A206-A208.

141. Moshopoulou, E., et al., *EVOLUTION OF STRUCTURE AND SUPERCONDUCTIVITY WITH LITHIUM CONTENT IN LI-1-XTI2O4.* Journal of Alloys and Compounds, 1993. **195**(1-2): p. 81-84.

142. Ceder, G., G.D. Garbulsky, and P.D. Tepesch, *CONVERGENT REAL-SPACE CLUSTER-EXPANSION FOR CONFIGURATIONAL DISORDER IN IONIC SYSTEMS.* Physical Review B, 1995. **51**(17): p. 11257-11261.

143.   Zhou, F., et al., *The Li intercalation potential of LiMPO4 and LiMSiO4 olivines with M = Fe, Mn, Co, Ni.* Electrochemistry Communications, 2004. **6**(11): p. 1144-1148.

144.   van de Walle, A. and M. Asta, *Self-driven lattice-model Monte Carlo simulations of alloy thermodynamic properties and phase diagrams.* Modelling and Simulation in Materials Science and Engineering, 2002. **10**(5): p. 521-538.

145.   Kohan, A.F., et al., *Computation of alloy phase diagrams at low temperatures.* Computational Materials Science, 1998. **9**(3-4): p. 389-396.

146.   Wagemaker, M., et al., *Li-Ion Diffusion in the Equilibrium Nanomorphology of Spinel Li4+xTi5O12.* Journal of Physical Chemistry B, 2009. **113**(1): p. 224-230.

147.   Lesar, R., R. Najafabadi, and D.J. Srolovitz, *FINITE-TEMPERATURE DEFECT PROPERTIES FROM FREE-ENERGY MINIMIZATION.* Physical Review Letters, 1989. **63**(6): p. 624-627.

148.   Compaan, K. and Y. Haven, *CORRELATION FACTORS FOR DIFFUSION IN SOLIDS.* Transactions of the Faraday Society, 1956. **52**(6): p. 786-801.

149.   Ouyang, C.Y., et al., *Ab initio molecular-dynamics studies on LixMn2O4 as cathode material for lithium secondary batteries.* Europhysics Letters, 2004. **67**(1): p. 28-34.

150.   Crusius, S., et al., *ON THE NUMERICAL TREATMENT OF MOVING BOUNDARY-PROBLEMS.* Zeitschrift Fur Metallkunde, 1992. **83**(9): p. 673-678.

151.   Hillert, M., *Solute drag, solute trapping and diffusional dissipation of Gibbs energy.* Acta Materialia, 1999. **47**(18): p. 4481-4505.

152.   Tepesch, P.D., G.D. Garbulsky, and G. Ceder, *MODEL FOR CONFIGURATIONAL THERMODYNAMICS IN IONIC SYSTEMS.* Physical Review Letters, 1995. **74**(12): p. 2272-2275.

153.   Thomas, J.C., et al., *Surface atomic order of compound III-V semiconductor alloys at finite temperature.* Physical Review B, 2009. **80**(12).

154.   Noel, M. and R. Santhanam, *Electrochemistry of graphite intercalation compounds.* Journal of Power Sources, 1998. **72**(1): p. 53-65.

155.   Wu, Y.P., E. Rahm, and R. Holze, *Carbon anode materials for lithium ion batteries.* Journal of Power Sources, 2003. **114**(2): p. 228-236.

156.   Ammundsen, B. and J. Paulsen, *Novel lithium-ion cathode materials based on layered manganese oxides.* Advanced Materials, 2001. **13**(12-13): p. 943-+.

157.   Lu, Z.H., D.D. MacNeil, and J.R. Dahn, *Layered cathode materials Li NixLi(1/3-2x/3)Mn(2/3-x/3) O-2 for lithium-ion batteries.* Electrochemical and Solid State Letters, 2001. **4**(11): p. A191-A194.

158.   Murphy, D.W., et al., *VANADIUM-OXIDE CATHODE MATERIALS FOR SECONDARY LITHIUM CELLS.* Journal of the Electrochemical Society, 1979. **126**(3): p. 497-499.

159.   Yamada, A. and S.C. Chung, *Crystal chemistry of the olivine-type Li(MnyFe1-y)PO4 and (MnyFe1-y)PO4 as possible 4 V cathode materials for lithium batteries.* Journal of the Electrochemical Society, 2001. **148**(8): p. A960-A967.

160.   Whittingham, M.S., et al., *Some transition metal (oxy)phosphates and vanadium oxides for lithium batteries.* Journal of Materials Chemistry, 2005. **15**(33): p. 3362-3379.

161.   Van der Ven, A. and G. Ceder, *Lithium diffusion in layered LixCoO2.* Electrochemical and Solid State Letters, 2000. **3**(7): p. 301-304.

162.   Xia, Y.Y. and M. Yoshio, *An investigation of lithium ion insertion into spinel structure Li-Mn-O compounds.* Journal of the Electrochemical Society, 1996. **143**(3): p. 825-833.

163.   Van der Ven, A., et al., *First-principles investigation of phase stability in LixCoO2.* Physical Review B, 1998. **58**(6): p. 2975-2987.

164.   Chung, G.C., et al., *Origin of graphite exfoliation - An investigation of the important role of solvent cointercalation.* Journal of the Electrochemical Society, 2000. **147**(12): p. 4391-4398.

165.   Shewmon, P.G., *Diffusion in solids*. 1983, Jenks, OK (P.O. Box 783, Jenks, OK. 74037): J. Williams Book. 203 p.

166.   Bodenez, V., et al., *Copper extrusion/reinjection in Cu-based thiospinels by electrochemical and chemical routes.* Chemistry of Materials, 2006. **18**(18): p. 4278-4287.